AN INVESTIGATION OF CAVITATION COOLING EFFECT IN CONVERGING-DIVERGING NOZZLES

by

ABDULMALIK ALKOTAMI

B.S., Kansas State University, 2012

A THESIS

submitted in partial fulfillment of the requirements for the degree

MASTER OF SCIENCE

Department of Mechanical and Nuclear Engineering
College of Engineering

KANSAS STATE UNIVERSITY
Manhattan, Kansas

2014

Approved by:

Major Professor
Dr. Mohammad Hosni

Abstract

A traditional cooling/refrigeration cycle has four main system components which are an evaporator, a compressor, a condenser, and an expansion valve. This type of cycle requires use of refrigerants which have been found to be harmful to the environment, including causing damage to the atmospheric ozone layer. The main objective of the project was to investigate a water-based non-vapor compression cooling system. Water as a working fluid has the advantages of being inexpensive and environmentally safe for use, as compared to commercially available chemical refrigerants. The water-based cooling system investigated employed cavitation phenomena in converging-diverging glass nozzles. Cavitation is an important phenomenon in fluids, and is common occurring in many devices such as pumps, refrigeration expansion valves, and capillary tubes. It occurs when the static pressure of the fluid falls below the vapor pressure, into a metastable liquid state. Cavitation can be in the form of traveling bubble cavitation, vortex cavitation, cloud cavitation, or attached wall cavitation.

In this thesis, the focus was first on visualizing cavitation for water flowing through converging- diverging glass nozzles. These nozzles had throat diameters between 2 mm and 4 mm. Two systems were used: (1) a continuous flow system, where water was driven by a centrifugal pump, and (2) a transient blow down system, where water flow was initiated using a suction pump. A high-speed camera was used to record videos and images of the associated cavitation phenomena. A thermal infrared camera was used in an attempt to measure temperature drop in the nozzle while the system was running

The second part of this thesis focused on the understanding of the fundamental thermodynamics phenomena and on the development of practical knowledge relevant to the cavitation process. Two equations of state were used in the analysis, the van der walls equation of state, and the Peng Robinson equation of state. Equations of state were used to predict the transition from vapor to liquid. At a given temperature, the equations were solved for a pressure value corresponding to saturated liquid and saturated vapor specific volume values. Then, the equations were used to determine the spinodal liquid and vapor lines, which represent the metastabillity limits for the liquid and vapor. The characteristic equations of state, combined with implementation of the Law of Corresponding States and thermodynamic theory, were used to estimate the temperature reduction available for refrigeration.

Table of Contents

List of Figures

List of Tables

Acknowledgements

I would like to thank my family for helping me and staying patient with me being busy and away from them most of my time. Special thanks to my parents for motivating and encouraging me to purse higher educations. I would like to express my appreciation to my committee members. Thanks to Dr. Hosni for being patient and understandable with me when I had my worst moments in developing the research, thanks for always encouraging and advising me to do the right thing. Thanks to Dr. Beck for guiding me in the technical problems in the laboratory and research. Thanks to Dr. Sorensen for teaching me a new way of thinking and developing theories in my research. Thanks to Dr. Eckels for guiding me to work the right area of research for me as well as helping me with the research analysis. Thanks to co-worker Jeff Wilms who helped me in the first year in the experiments and using the tools in the laboratory. Thank you all for making my dream come true and for making it possible.

Chapter 1 - Introduction

The knowledge of the way a simple refrigeration cycle works is helpful in the development of a non-vapor compression cooling system. From the second law of thermodynamics, heat always flows from an object at higher temperature to a lower temperature. Heat transfer occurs when there is a temperature difference across a media or between two objects. A simple refrigeration cycle has four main components which include an evaporator, a compressor, a condenser, and an expansion valve. The compressor circulates working the fluid throughout the system; it compresses the cold low pressure vapor into hot high pressure vapor. The hot vapor passes through the condenser to reject heat and sends the liquid to the expansion valve, and subsequently to the evaporator as it completes a cycle. The expansion valve controls the flow of the working fluid to the evaporator; it also lowers the pressure and therefore lowers the temperature. Warm air passes through the evaporator that contains the cold fluid, the fluid absorbs the heat from air, and the cold air is delivered to the controlled indoor environment. Figure 1.1 shows components of a simple refrigeration/ air conditioning system.

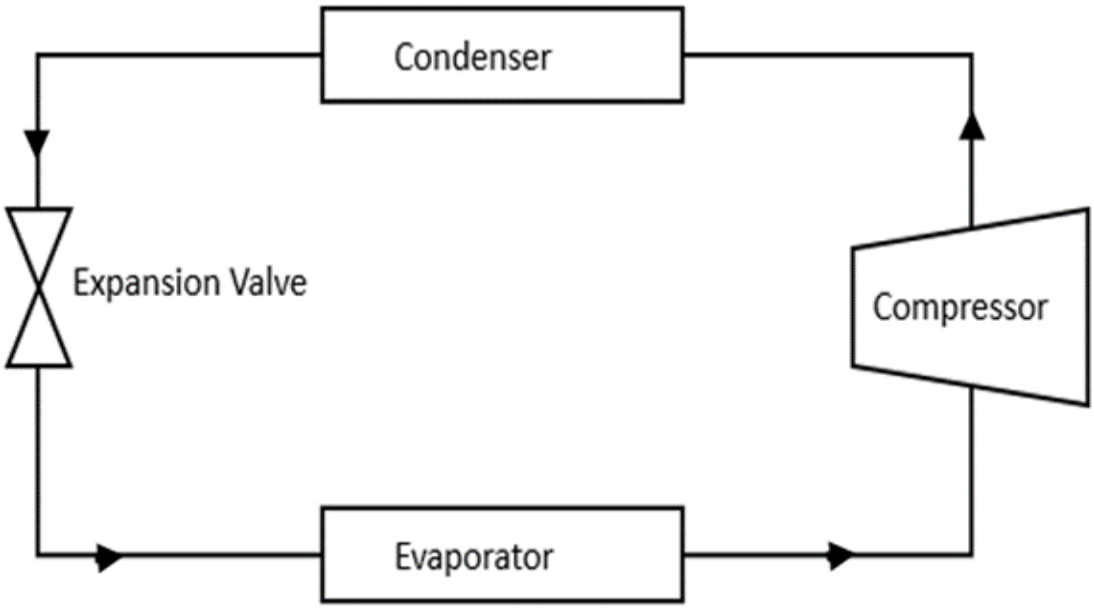

Figure 1.1 Components of a simple refrigeration/ air conditioning system

The research reported in this thesis investigates the possibility of developing a water based cooling and refrigeration system. Using water instead of a refrigerant as a working fluid in a system has many advantages. Water as a refrigerant is cheap compared to other working fluids. It's also environmentally neutral and safe to be used at any location. The main objective of the project is to visualize cavitation in a converging-diverging nozzle while fluid is going through it.

Cavitation could be a common problem in many devices such as pumps, control valves, and heat exchangers. It can cause serious tear and damages as well as reducing the device life time. Cavitation occurs when the static pressure of the fluid drops below the vapor pressure, while keeping the temperature constant. On the other hand, cavitation can be helpful for researchers which provides opportunities for important engineering applications as cooling in converging-diverging nozzles. The current project studies the cavitation occurring in a converging-diverging nozzle. A two phase flow moves at low velocities then accelerates downstream the throat of the nozzle. The pressure drop that occurs in the system causes cavitation, which causes a temperature drop in the fluid. The temperature drop is used to absorb heat from the surroundings. The thesis will discuss the cavitation visualization in various types of converging-diverging nozzle. Figure 1.2 shows a refrigeration cycle using a converging-diverging nozzle that was used in the patent [1].

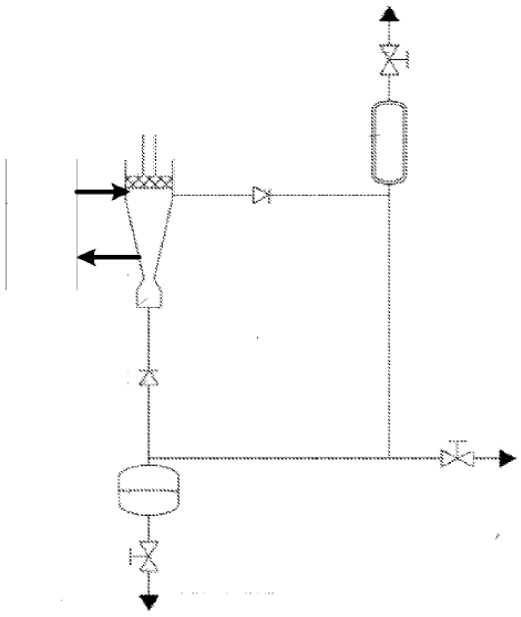

Figure 1.2 Refrigeration cycle using a converging diverging nozzle [1]

1.1 Literature Review

Brennen published a book titled “Cavitation and Bubble Dynamics” from Oxford University [2]. The book is a reference book for researchers that work in cavitation and bubble dynamics areas. The book discusses the two-phase mixtures of vapor and the formation of the vapor bubble in the liquid. It focuses on the formation of bubbles in the flow, bubbles collapse, the different types of cavitation, and the physics of nucleation which could be either cavitation or boiling. The understanding of the phase change from vapor to liquid is a great start to understanding the formation of cavitation.

Figure 1.3 shows the typical P-T and P-V phase diagram which consists of a coexistence curve, temperature isotherms, and spinodal lines. The triple point is described as the point where liquid, vapor, and solid states coexist. The critical point in the phase diagram occurs when the liquid and vapor phases have the same density. The spinodal line consists of a liquid and a vapor lines; the liquid line crosses the minimum point of temperature isotherm and the vapor line crosses the maximum point of the temperature [2].

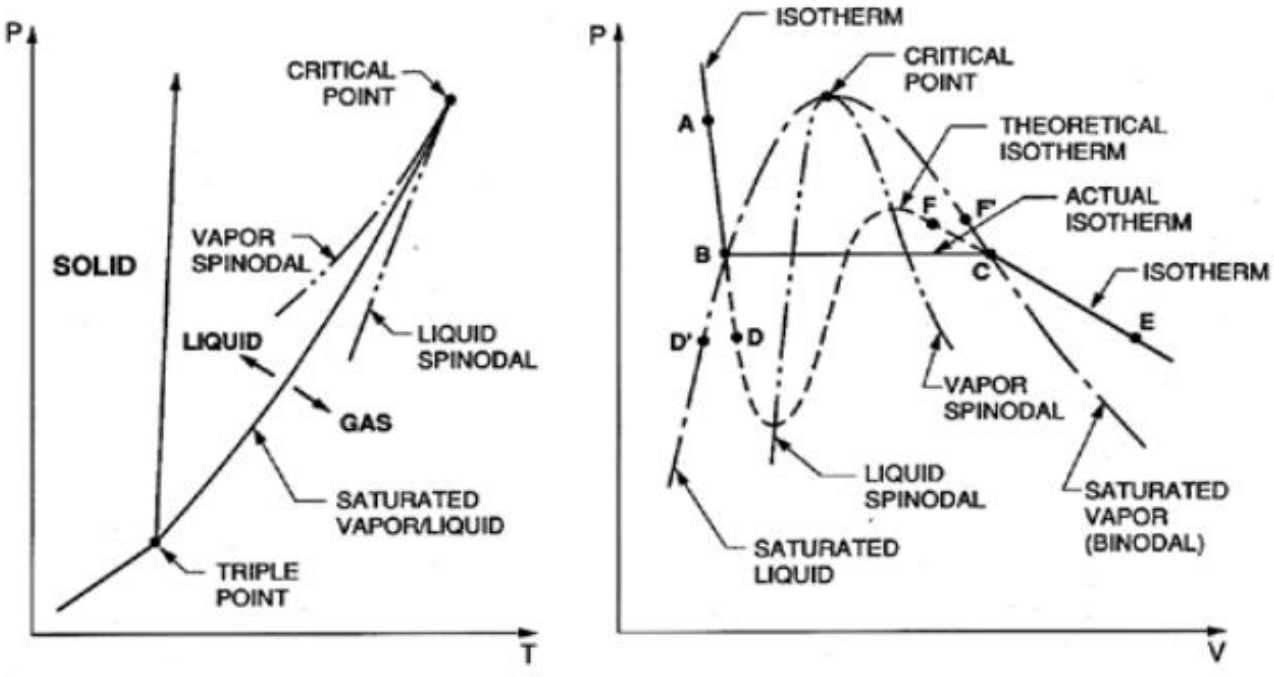

Figure 1.3 Typical P-T and P-V phase diagram [2]

Cavitation can be described as the process of changing from liquid to gas at a constant temperature; the change is due to a pressure drop which falls below saturated vapor pressure. Studies have focused in what happens in a given flow if the pressure decreases or the velocity increases so the pressure in the flow equals the vapor pressure, and defined a relationship called cavitation number [2].

$$\sigma = \frac{p_\infty - p_v(T_\infty)}{\frac{1}{2}\rho_L U_\infty^2} \qquad (1.1)$$

The value U_∞ and p_∞ are the velocity and the pressure of the upstream flow, p_v is the vapor pressure and ρ is the density. Every flow has a value of cavitation number even if the flow does not cavitate. If the value of the cavitation number is large, single phase liquid flow is developed. If the value decreases, cavitation and nucleation start to form at a value called incipient cavitation. When the cavitation number is higher than the incipient cavitation, cavitation will vanish. Cavitation will have the same behavior as long as they have the same cavitation number value.

Brennen described four different types of cavitation, as shown in Figure 1.4: the traveling bubble cavitation, vortex cavitation, cloud cavitation, and attached or sheet cavitation [2]. A detailed model was attempted for the growth of traveling cavitation bubbles. It was assumed that bubbles initially are micron nuclei before moving with the liquid velocity on the streamline, and cavitation was formed when bubbles reached a size of 1 mm. Another model that was attempted on the traveling bubble cavitation was the Rayleigh-Plesset Model, which explored the influence of the size and location of the nucleus. It was shown that nuclei could have a large pressure gradient as they get closer to the stagnation point due to the streamline unexpectedly faced with a pressure drop region. Vortex Cavitation is a term used for the cavitation inception that forms in the vortices of propellers, pump impellers, or in a swirling flow. It develops when having a vorticity region where the pressure in the vortex core is smaller than any point in the flow. The vortex will be filled slowly with vapor when the cavitation number starts to decrease. A stable flow structure can be created when having continuous vortex cavitation on the blades of a propeller. The presence of the streamwise vortices could be an important reason for developing the cavitation inception. Cloud cavitation is the formation and collapse of cavitation bubbles, it

could develop from the shedding of cavitating vortices or a response to the disturbance forced on the flow. Cloud cavitation can be caused by the interference of a rotor and stator blades in a pump or turbine, and the contact between a propeller and a wake which created by the hull. A combined study on the complicated flow pattern involving cloud cavitation on an oscillating hydrofoil has shown the formation, separation, and collapse of the cavitation. The studies have shown the development of a bang due to the collapsing of the cloud cavitation in the pitch. The last type of cavitation is the attached sheet cavitation which develops a region of separated flow filled with vapor. Sheet cavitation usually occurs on a hydrofoil or propeller blade at an angle of attack greater than 10^{o} [2].

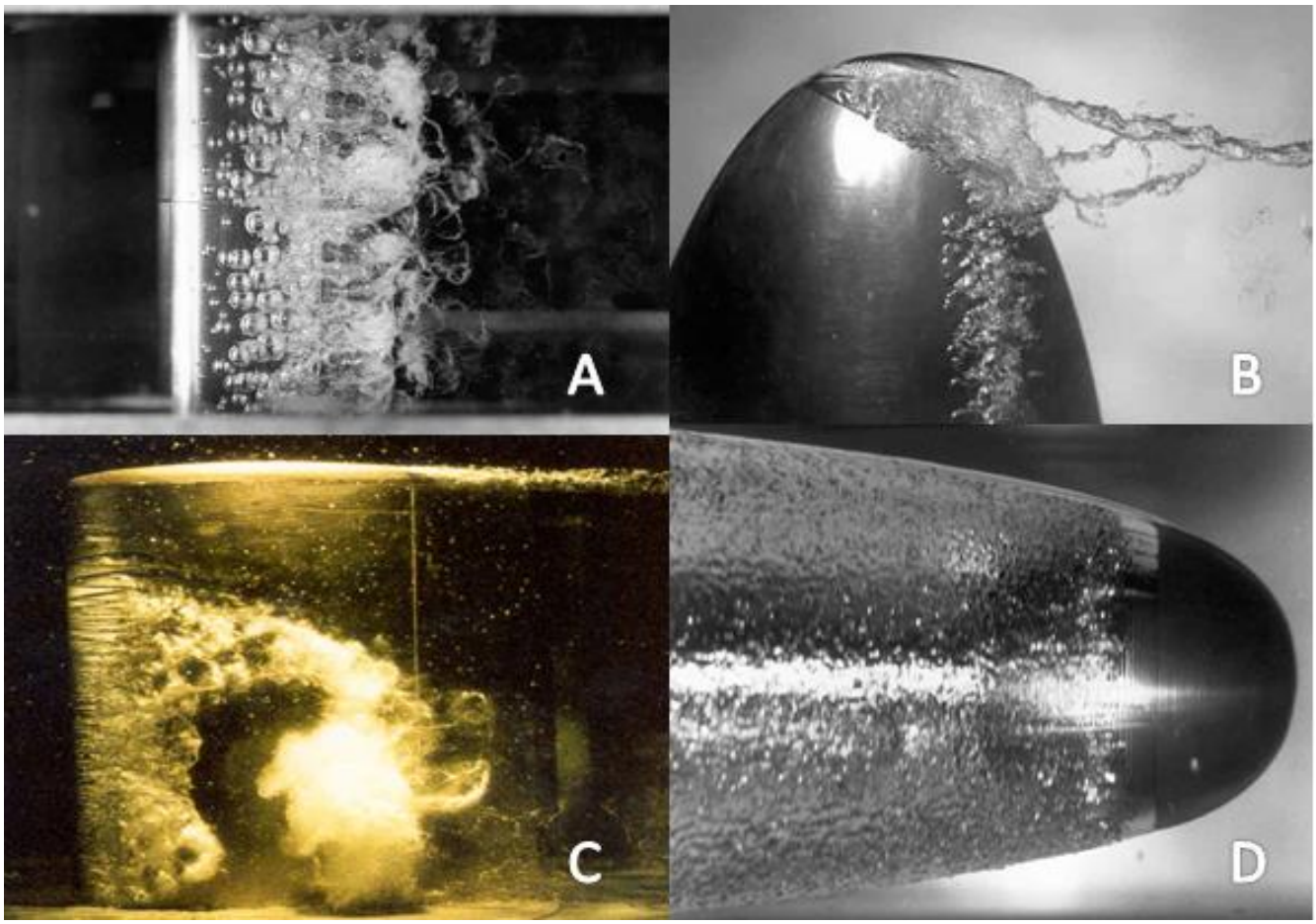

Figure 1.4 Types of cavitation; A. Traveling bubble cavitation, B. Vortex cavitation, C. Cloud cavitation, D. Attached or sheet cavitation [2]

Davis [3] developed a dissertation cavitation of aviation fuel and water in a converging-diverging nozzle. The research focused on the fully development cavitation. As shown in Figure 1.5 the nozzle geometry and test section, a venturi nozzle used in a blow-down system facility. The system includes two tanks used as liquid reservoir; the fluid is pumped down to the needed pressure by using a vacuum pump. The nozzle was designed using a fifth order polynomial; inlet and exit diameters were 19 mm, and a throat diameter of 1.58 mm. High-speed camera used to acquire the flow visualization [3]. Figure 1.6 shows the flow going from left to right of the water test with a pressure downstream of 20 kPa. Void fractions were measured as well, the figure shows from x/L = 0.2 to x/L = 0.8, bubbles start to develop at x/L ≈ 0.25, and there is an abrupt change at x/L ≈ 0.6. Figure 1.7 shows the void fraction measurement with the pressure, which shows as the pressure decreases, the bubble start to form.

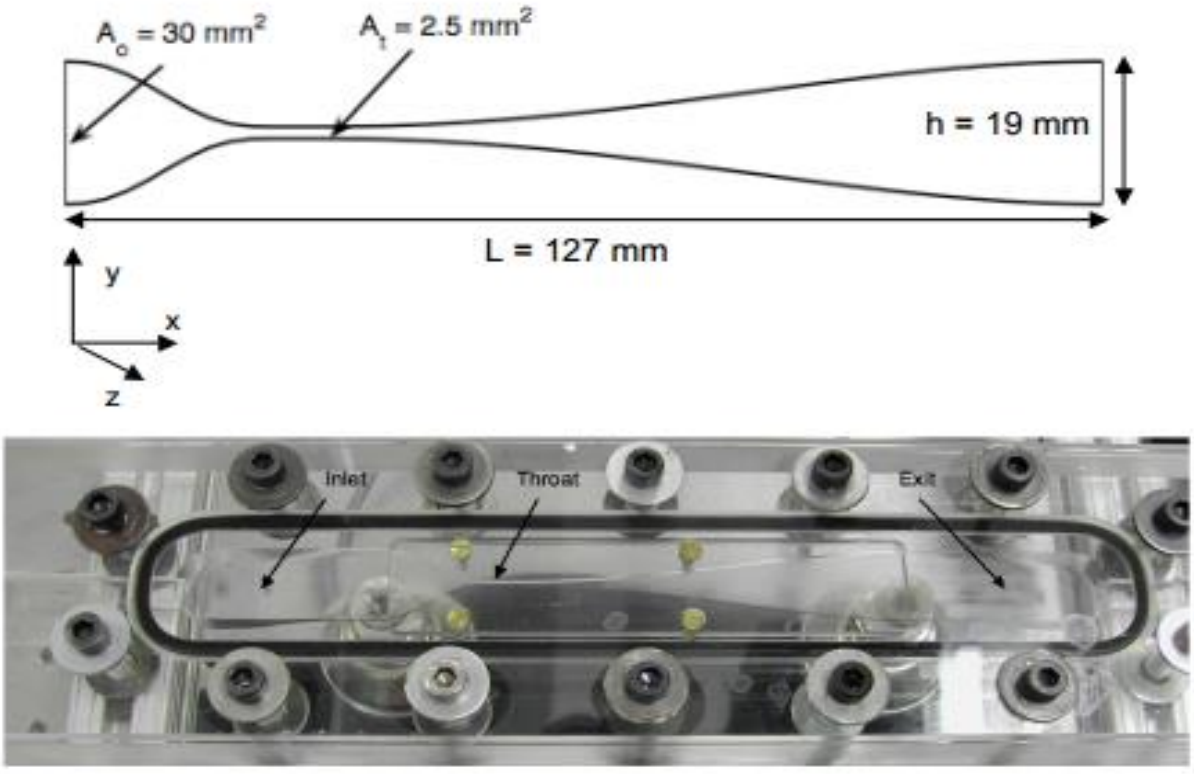

Figure 1.5 Nozzle and test section geometry [3]

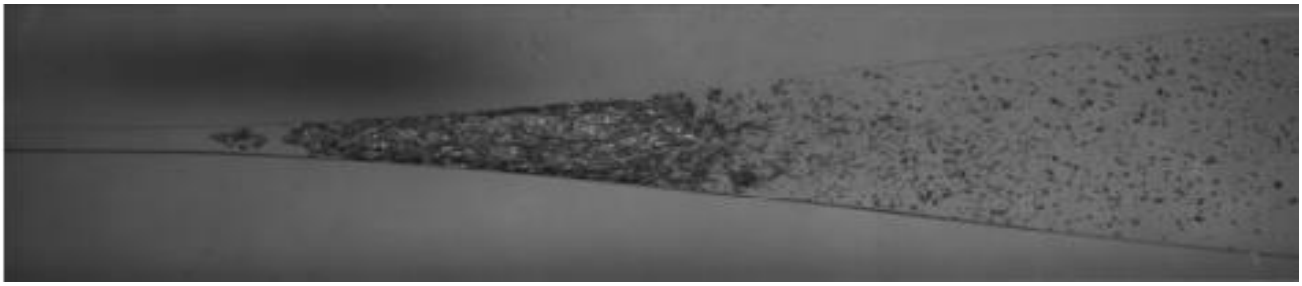

Figure 1.6 Capture of water cavitation mixture [3]

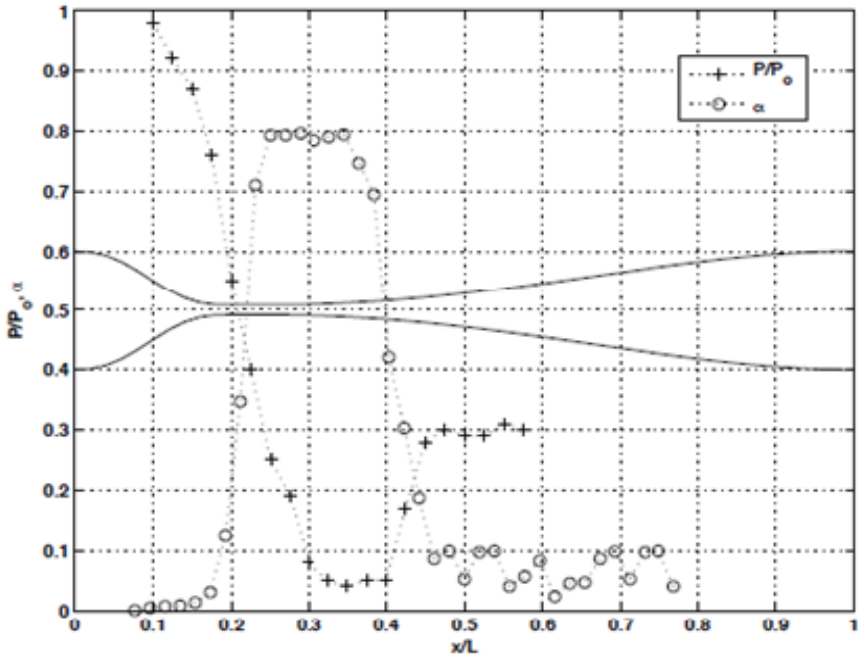

Figure 1.7 Void fraction measurements with the pressure [3]

In a study by Nakagawa, et. al [4], CO2 have used as an alternative refrigerant in a converging-diverging nozzle to measure the shock waves. A modified simple vapor compression cycle was used as the refrigeration cycle, and a compressor output of 1.3 kW. A rectangular converging-diverging nozzle was used; the length of the diverging section was 8.38 mm. A shorter lengths nozzle, gives higher outlet pressure value; a longer lengths nozzle, gives lower outlet pressure value [4]. Figure 1.8 shows results for short nozzles, the biggest back pressure range was 3.6-5.9 MPa. Two types of shock waves were discovered while testing the short nozzles. First type was the pseudo shock wave with a slow increase in pressure, can be seen in the first plot of each section in Figure 1.8. Second type is dispersed shock wave with gradual increase in pressure, can be seen in the last two plots of each section in Figure 1.7 [4].

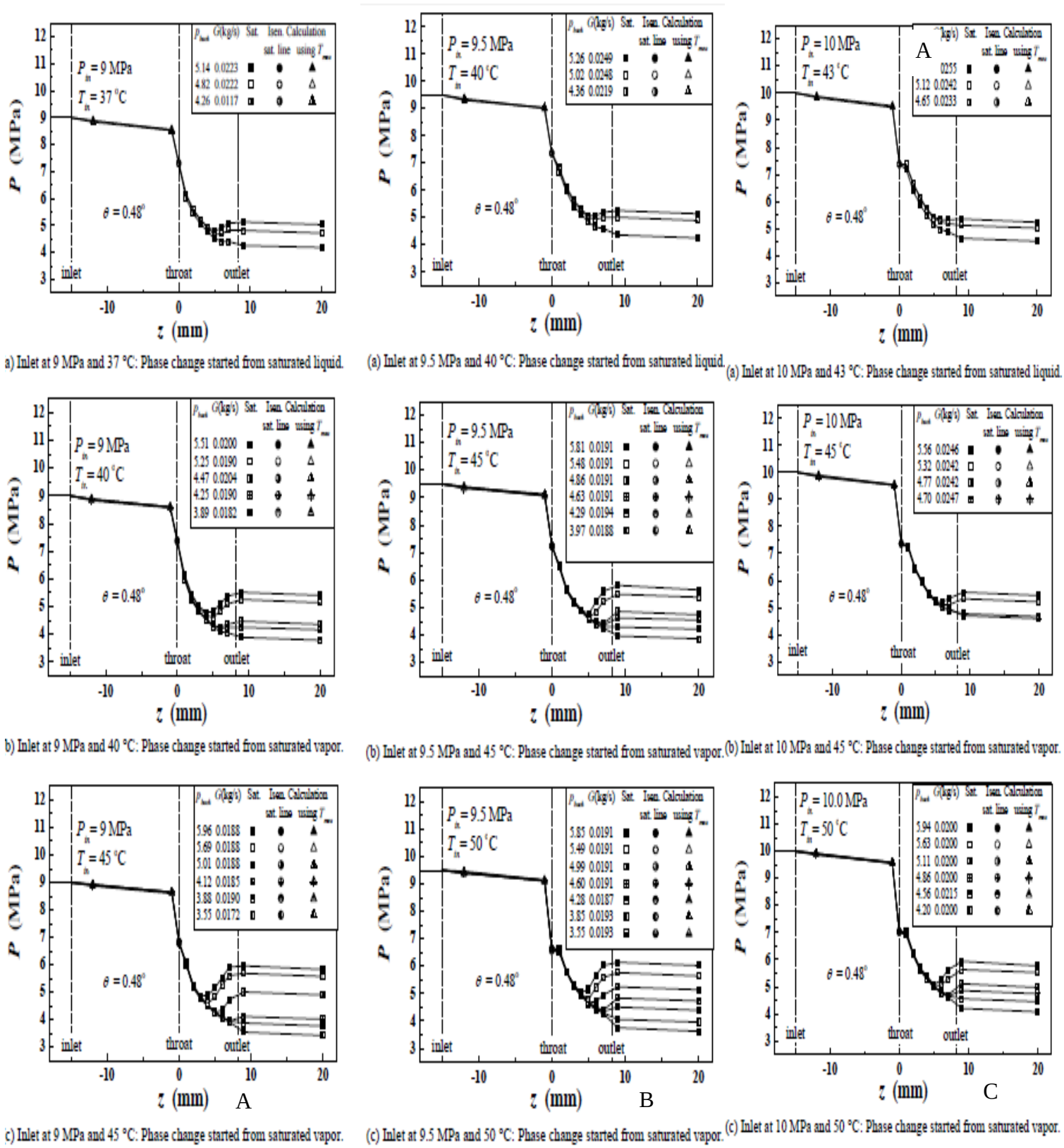

a) Inlet at 9 MPa and 37 °C: Phase change started from saturated liquid.

(a) Inlet at 9.5 MPa and 40 °C: Phase change started from saturated liquid.

(a) Inlet at 10 MPa and 43 °C: Phase change started from saturated liquid.

b) Inlet at 9 MPa and 40 °C: Phase change started from saturated vapor.

(b) Inlet at 9.5 MPa and 45 °C: Phase change started from saturated vapor.

(b) Inlet at 10 MPa and 45 °C: Phase change started from saturated vapor.

c) Inlet at 9 MPa and 45 °C: Phase change started from saturated vapor.

(c) Inlet at 9.5 MPa and 50 °C: Phase change started from saturated vapor.

(c) Inlet at 10 MPa and 50 °C: Phase change started from saturated vapor.

Figure 1.8 Shock wave at chosen pressure and various temperatures; A. 9 MPa, B. 9.5 MPa, C. 10 MPa [4]

An investigation on cavitation enhanced heat transfer in micro-channels studied by Schneider, Kosar, Kuo, Mishra, Cole, Scaringe, and Peles. The study discovered a unique two-phase flow pattern that enhances heat transfer [5]. Figure 1.9 shows a CAD model of the device they used. The device consists of five parallel micro-channels spaced 200 μm. A flow distributive pillar used to develop a homogenous flow, pillars diameters are 100 μm. Five orifices were placed at the entrance of each micro-channel, orifices are 20 μm wide and 200 μm long. Orifices are used to develop cavitation existence [5]. They used water as the fluid flows through the channels, and visualized the cavitation using a high speed camera. They discovered while using the same mass velocity in a supercavitating and noncavitating flow conditions, there was an increase of almost 67% heat transfer enhancement in the supercavitating flow [5].

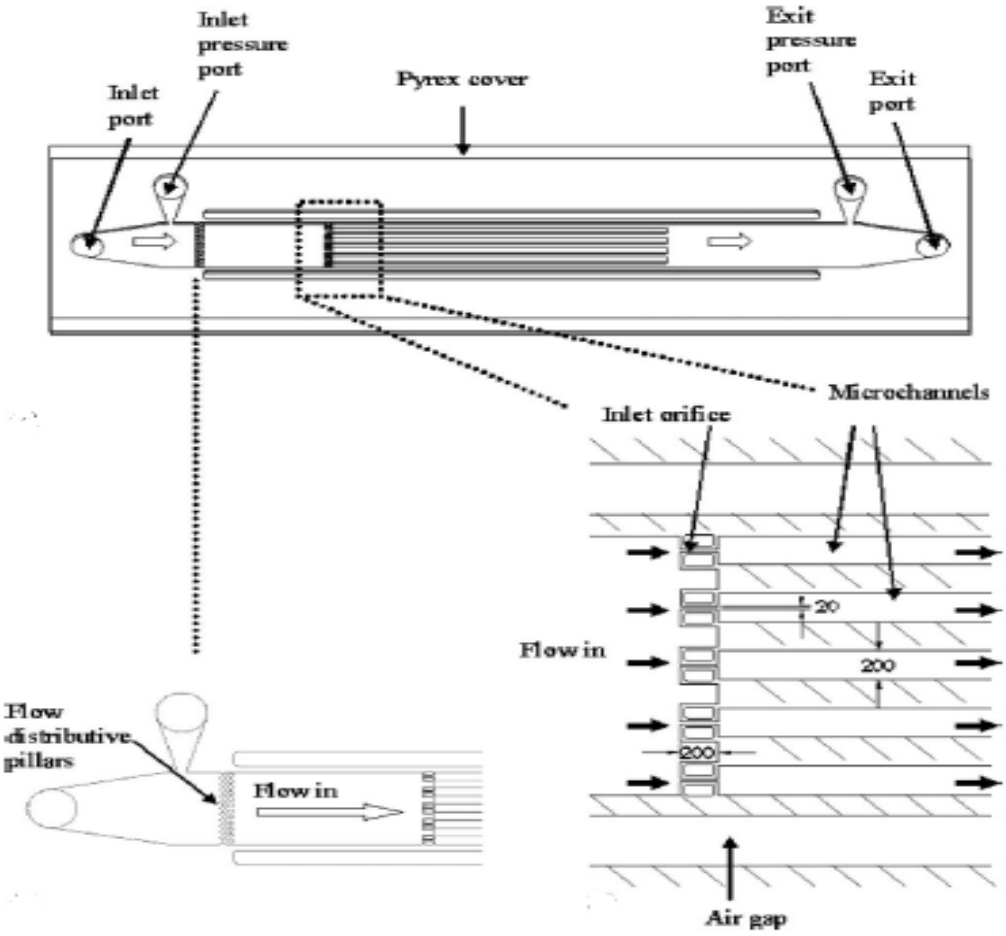

Figure 1.9 A. Micro-channel device, B. Pillars, C. Inlet region geometry [5]

In a research by Wang and Brennen, a one dimensional cavitating flow through a converging-diverging nozzle was studied [6]. They used the Rayleigh-Plesset equation to model the dynamics of the cavitating bubbles. They set the cavitation number to 0.8 so it would develop the cavitation; the nozzle's non-dimensional length is 500 [6]. Figure 1.10 shows the non-dimensional fluid velocity as a function of normalized position for different void fractions. The flow is incompressible pure liquid when the upstream void fraction is at 0. They discovered that the wavelength of the variation in the plot increase with an increase in the void fraction. Different types of flows was found; a quasi-steady flow which shown in the figure, and a quasi-unsteady which is equivalent to flashing flow [6]. According to the conservation of mass and momentum, the velocity increases due to developed bubbles in the flow which then decreases the fluid pressure due to Bernoulli's effect. The pressure decrease causes the bubbles to grow using the Rayleigh-Plesset equation. The process of increasing velocity and void fraction, and decreasing fluid pressure causes the flow to flash back to vapor [6].

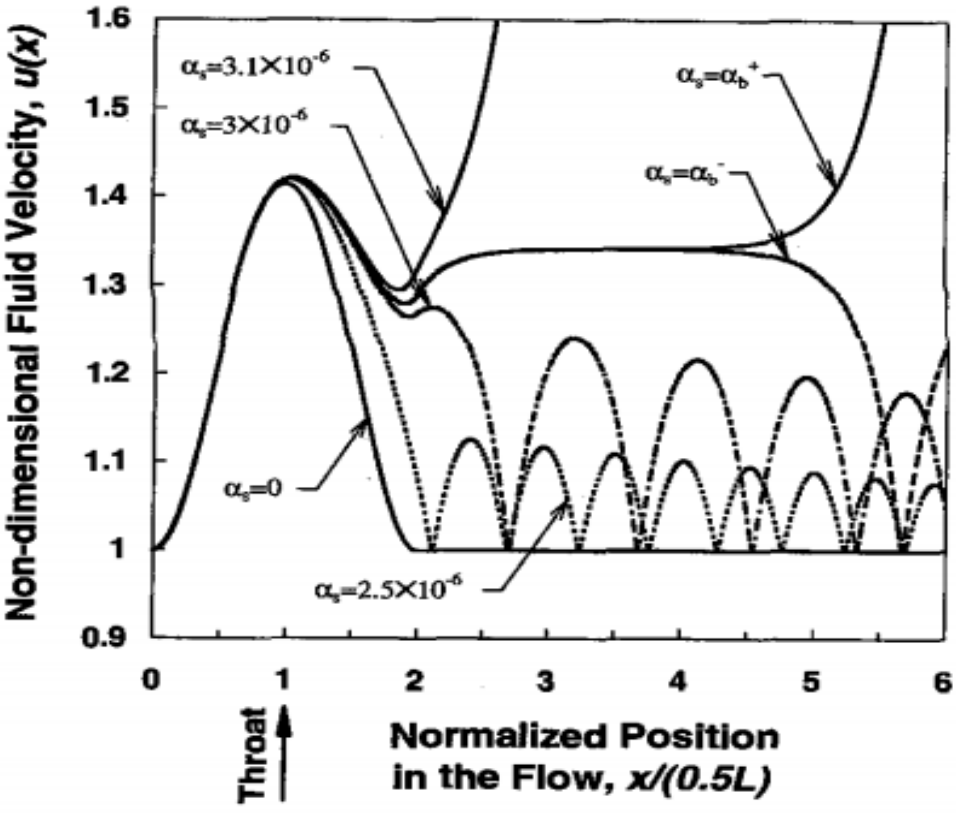

Figure 1.10 Fluid velocity as function of normalized position for various void fractions [6]

1.2 Objectives

The project emphasis is developing a water based cooling and refrigeration system. A water flowing system through converging-diverging glass nozzles was built. Visualizing cavitation is one of the main objectives in the project. Because the phenomena and testing takes place in a fast and short time scale, a high-speed camera with proper lighting source were used to contest the type of speed and get the perfect images needed. Another objective in the research is to understand the fundamental knowledge of phase diagram of water, and the effect it has on developing cavitation in the flow. Also, equation of the state was studied to help us understand the basic knowledge of the project. Two items are introduced for the project objectives below which are the cavitation visualization and quantitative results.

1.2.1 Cavitation Visualization

Cavitation is an outstanding phenomenon that occurs in many flow devices such as pumps, control valves, and heat exchangers. As we discussed earlier in the literature review, it has different kinds which include the traveling bubble cavitation, vortex cavitation, cloud cavitation, and attached or sheet cavitation. Nozzle geometry can be a huge factor on the velocity and void fraction which affects the cavitation development.

1.2.2 Quantitative Results

The research emphasis was on fundamental knowledge of the two-phase flow in converging-diverging nozzle as well as experimental work through glass nozzles. Fundamental knowledge of the equation of state and conservation equations were studied. Experimental work included the measurements of void fraction, velocity, flow quality, and temperature drop in the converging-diverging glass nozzles.

Chapter 2 - Experimental Test Facility and System Set Up

This chapter will show the system setups for testing water flowing through nozzles to develop water based cooling system. Glass nozzles that have been used in the system will be described. Also, four systems will be identified, Continuous Flow system, transient blow down system, piezoelectric system, and visualization system.

2.1 Glass Nozzles

As the project started, plastic nozzles used for testing. Then, glass nozzles were built, by a glassblower at Kansas State University, for use instead of plastic nozzles. Glass nozzles have an advantage of having less time to be machined, and costs less than plastic nozzles. It's also easy to visualize the flow through glass nozzles. Nozzles were made by hand, which did not have the exact dimensions specified by the team. Three types of nozzles have been used in the experiments, 2 mm throat diameter nozzle, a 2.5 mm throat diameter and 4 mm throat diameter nozzle. Details of the nozzles are provided below.

2.1.1 Nozzles Details

Figure 2.1 shows the designs for the glass nozzles. First, Figure 2.1A shows two 50 mm straight nozzles one has 2 mm throat diameter nozzle, converging section for 2 mm nozzle is a bell shaped and it increases with an expansion angle in the diverging side. Then, Figure 2.1B shows 2.5 mm throat diameter nozzle that has an 8.76 mm bell shaped; there is a rapid increase in the throat diameter by 0.5 mm. Figure 2.1C shows the last nozzle which is a 4 mm throat diameter nozzle with a bell shaped expansion diverging side and straight converging side.

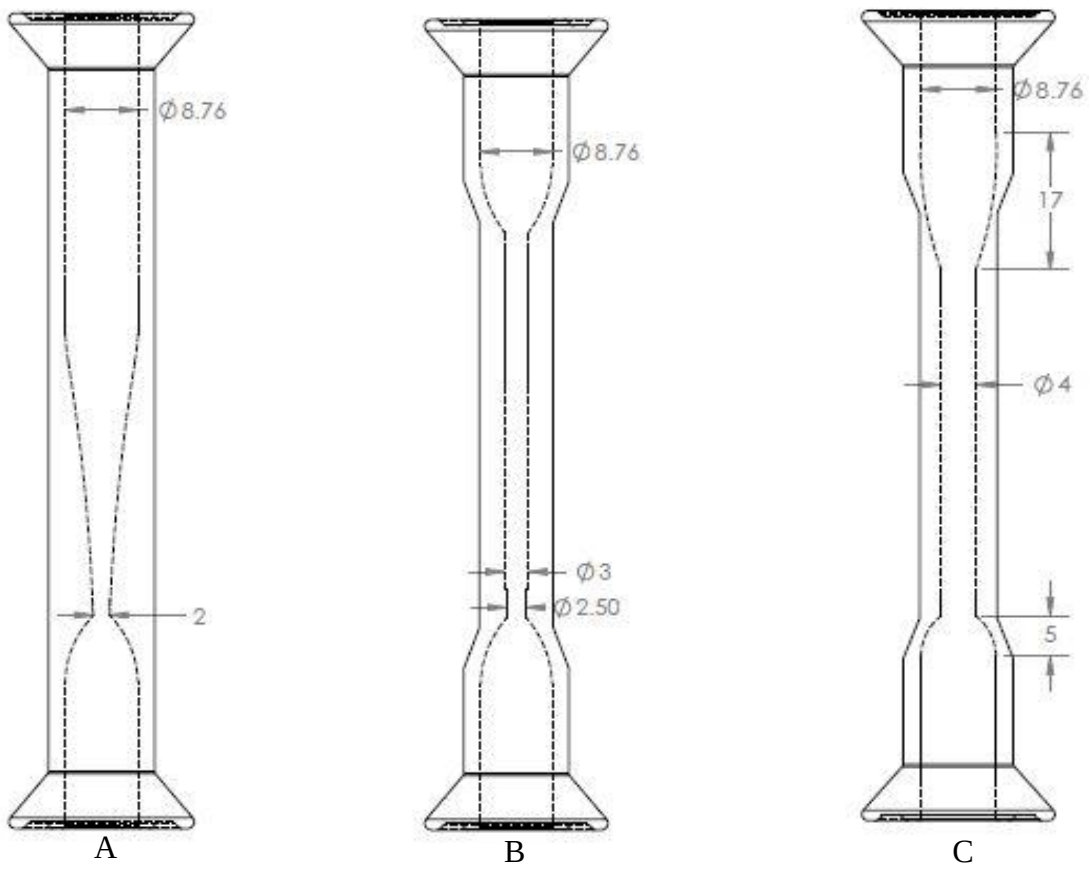

Figure 2.1 A. 2 mm throat diameter nozzle, B. 2.5 mm throat diameter nozzle, C. 4 mm throat diameter

2.2 Continuous Flow System

The continuous flow system flow diagram is shown in Figure 2.2, it consists of two main loops, primary loop and secondary loop. The primary loop consists of a feeding pump that drives the flow vertically from the main water tank to the nozzle which handles the flow with very low suction head; the flow travels through an electric heater which converts the electrical energy into heat, a micro guardian filter is been used to filter the flow. Then, the flow goes into a reversed osmosis device that removes types of molecules and ions from the fluid which makes the fluid pure. Pressure and temperature probes were installed before the flow enters the nozzle to record the inlet measurements for the flow. The flow then travels through the glass

converging-diverging nozzle which then goes to the reservoir to be back in the main water tank. The secondary loop was used to control the temperature of the flow; it is also called the cooling loop because it removes energy from the water after it has flown in the primary loop. A centrifugal pump is used to drive the flow from the main tank to a heat exchanger which cools the fluid using tap water. The flow travels through an electric heater and travels back to the main water tank. The system images and setup are shown in Figure 2.3 below.

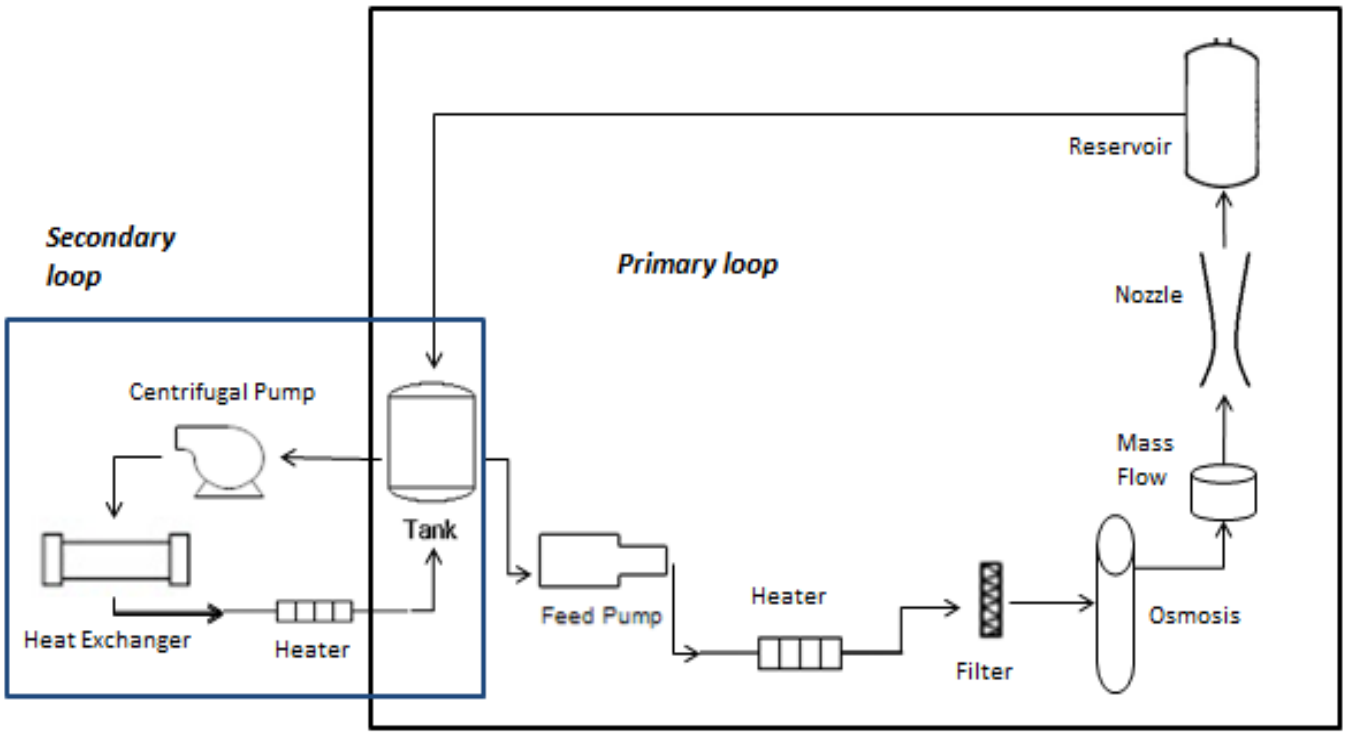

Figure 2.2 Flow diagram consists of a primary loop and a secondary loop

Figure 2.3 Shows A. Test rig, B. Water reservoir, C. Nozzle setup

2.3 Transient Blow Down System

A transient blow down system was explored by Jeff Wilms [1]. The main purpose of the transient blow down system was to change how the fluid was driven through the nozzle. In the previous system, the water was driven by a centrifugal pump. The transient blow down system consists of two water tanks, valve, and the nozzle. As shown in Figure 2.4, the reservoir water tank is being depressurized using a suction pump. Once the desired pressure has been met, valve is opened and the water in the outlet tank, which is at atmospheric pressure, is driven through the nozzle to the reservoir. The system images and setup are shown in Figure 2.5 below.

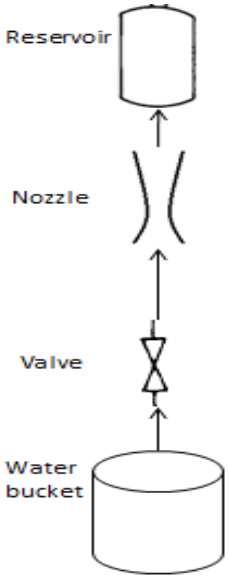

Figure 2.5 Transient blow down flow diagram

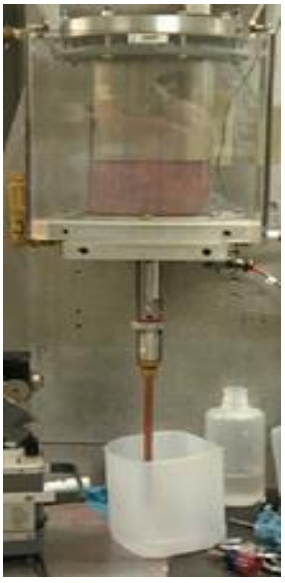

Figure 2.4 Transient blow down system setup

2.4 Piezoelectric System

A Piezoelectric system consists of a piezo disk which gives sound vibrations that would generate voltages and ultrasonic waves to create oscillation. The system set up is shown below in Figure 2.6, the piezo disk is tested on beakers, nozzles, tubes; results are shown in the next chapter.

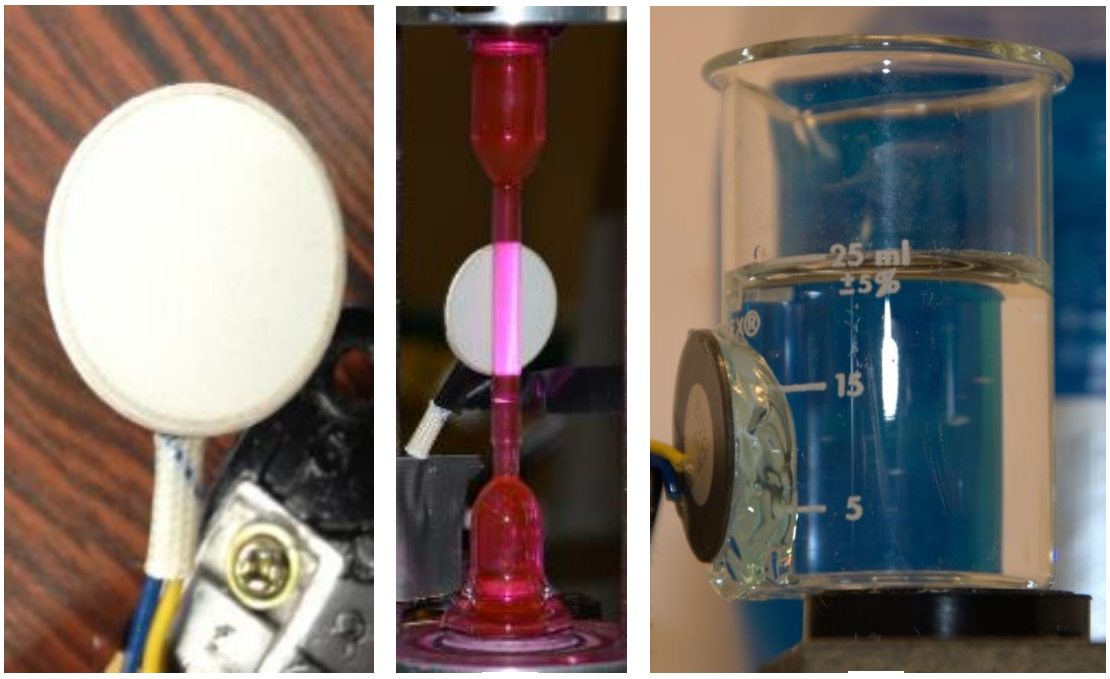

A B C

Figure 2.6 A. Piezo Disk, B. Disk on the nozzle, C. Nozzle on the beaker

2.5 Visualization System

Fluid flow and motion were studied closely using several techniques. Flow visualization gives researchers a quick and clear qualitative assessment of the flow. One of the main advantages is giving detailed information for the entire flow along the entire nozzle. One of the techniques employed was the tracer or dye particles which give clear view of the flow. Cameras were used for flow visualization as well. This section introduces a high speed camera and thermal infrared camera.

2.5.1 High Speed Camera

Having a high speed camera was necessary for flow visualization. A SA5 High Speed Camera was acquired for the project. The camera provides 7,500 frames per second (fps) at a resolution of 1,024 by 1,000 pixels. The camera is capable of providing a maximum of 775,000 fps but it reduces the resolution to 128 by 24 pixels. It has 20μm pixels that ensure light sensitivity for high speed or low light applications.

The high speed camera set up to be used for experiment is shown in Figure 2.7. It's being controlled by the Photron Fastcam Viewer (PFV) software; and camera is connected to the computer using a cable. A microscope was used to provide a close up images of the cavitation in the nozzle. Also, a 60 mm and 25 mm Nikon AF-S lenses were used to provide a good angle of the entire nozzle.

High speed cameras require much more light than any normal photography. Using the perfect amount of lights, help on recording the best results from the High speed camera. An increase in the camera speeds requires more intense amount of lights. A halogen light source from Thor Labs was used in the system as shown in Figure 2.8; a fiber optic cable was used to deliver the light to the nozzle. A clear glass diffusion filter was used between the light source and the nozzle in the system.

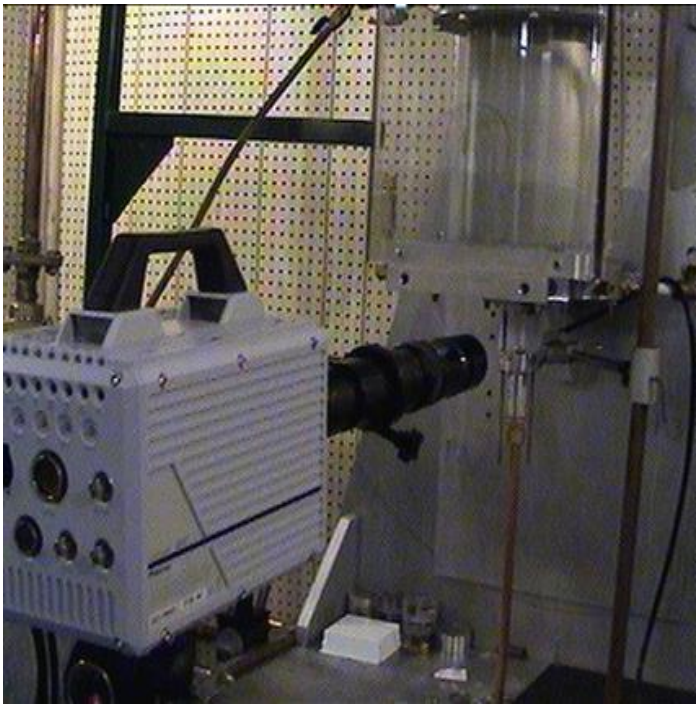

Figure 2.8 System setup with high speed camera

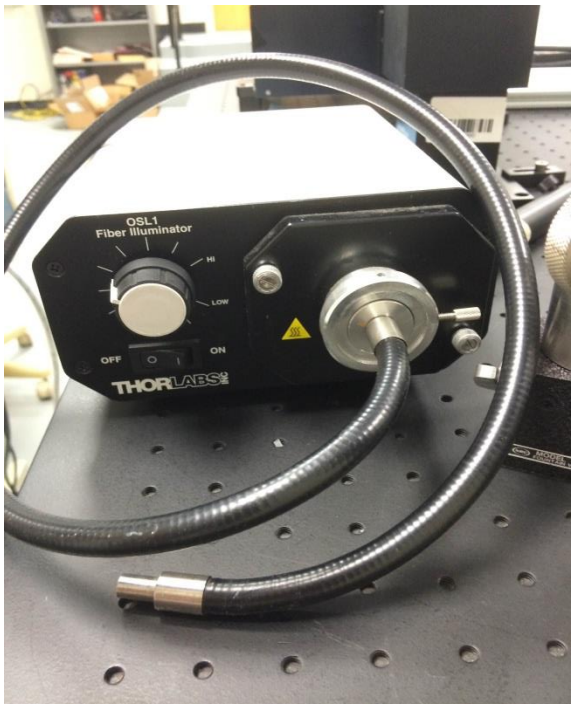

Figure 2.7 Light source with fiber optic

2.5.2 Thermal Infrared Camera

Another type of cameras, FLIR S65 Thermal Infrared Camera, was used for thermal flow visualization. The IR camera has a high temperature filter up to 1500 ºC. Camera is held in front of the nozzle setup on a tripod, operated locally or by a remote control. The camera takes high definition thermal images as well as recording visual images using the built-in digital camera. An advantage of the camera was its light weight. At, 4.4 lb., it was the lightest weight thermal infrared camera available in the market. It's used to measure the temperature drop on the entire nozzle while the fluid is flowing through the nozzle. Figure 2.9 shows the IR camera. Figure 2.10 shows a thermal image of the nozzle captured using the IR camera.

Figure 2.9 Thermal Infrared Camera

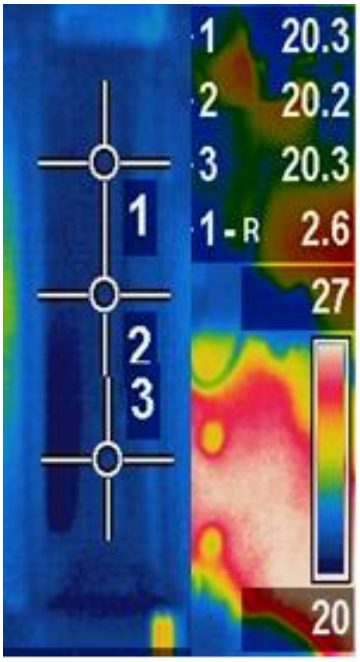

Figure 2.10 Nozzle thermal image

Chapter 3 - Experiment Results

This chapter describes the results of experiments. It focuses on the fluid motion and visualization in the converging-diverging nozzle in a continuous flow system and a transient blow down system. Flow visualization provides a quick qualitative assessment of the entire flow. A high speed camera was used in a continuous flow system tests to get the tiny details of cavitation occurring in the entire nozzle; and, in particular at the throat. Different types of nozzles geometries and throat diameter were used in the experiments. Subsequently, different kind of nozzles testing called a transient blow-down system was explored in which, the system uses a different driving method of water flowing through the nozzle. A high speed camera; as well as, an infrared thermal camera were used to record the cavitation development and the temperature drop, respectively, in the blow down system. Furthermore, a new way of developing nucleation in the converging-diverging nozzle using a piezoelectric system was evaluated. Piezoelectric disk showed some positive results on developing nucleation in water but it was difficult to implement it in the experimental test facility systems.

3.1 Continuous Flow System

A continuous flow system is a pull up system where a pump drives water vertically through a converging-diverging nozzle. Different types of nozzles were tested. Wilms [7] tested different nozzles geometries using the same system. Table 1, reproduced from Wilms thesis [7], shows the designs of all the glass nozzles used [7]. The research work reported herein is a continuation of Wilms project. Nozzles 8 and 9, which are highlighted in the table, were used in the new testing, reported in this thesis.

Nozzle 8, which is called the expansion nozzle, was designed with a large expansion angle and the converging section extended for about 50 mm until the diverging section of the nozzle with a throat diameter of 2 mm. The converging side starts with a bell shape. Figure 3.1 shows the results of testing the expansion nozzle in the system. A 60 mm lens in the high speed camera with a 20,000 frame per second rate was used. The inlet temperature, pressure, and flow rate in the system were 30 C°, 43 psia, and 41 g/s, respectively.

	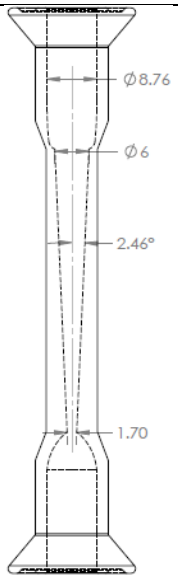	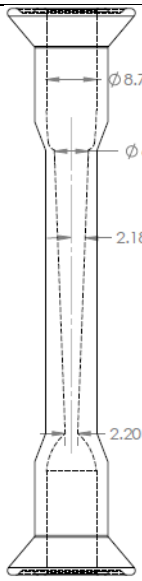	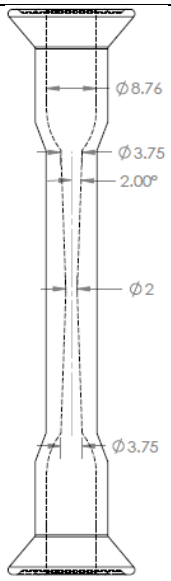	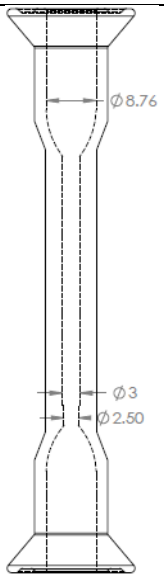	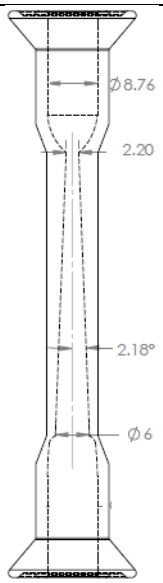
Nozzle Name	Nozzle 1	Nozzle 2	Nozzle 3	Nozzle 4	Inverse Nozzle 2
Throat Diameter (mm)	1.7	2.2	2	2.5	2.2
Converging	Bell	Bell	2° Angle	Bell	2.18°
Diverging	2.46°	2.18°	2° Angle	Bell	Bell
Section	3.1.3, 4	3.1.3,3.5, 4	3.1.4	3.1.5	3.2.1
	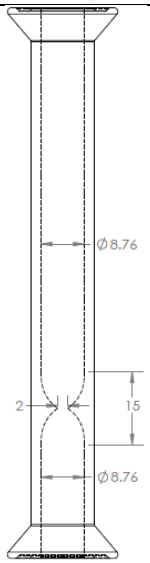	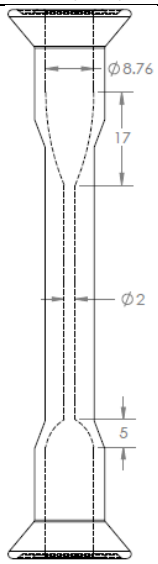	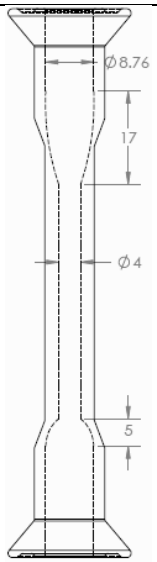	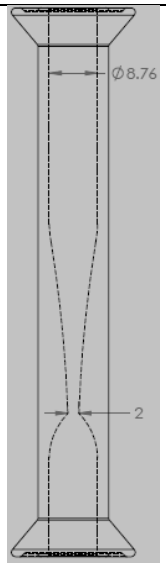	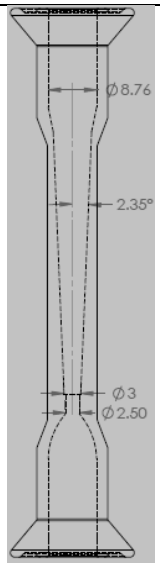
Nozzle Name	Nozzle 5	Nozzle 6	***Nozzle 7***	***Nozzle 8***	***Nozzle 9***
Throat Diameter (mm)	2	2	***4***	***2***	***2.5***
Converging	Bell	Straight	***Straight***	***Bell***	***Bell***
Diverging	Bell	Bell- 17 or 5 mm	***Bell- 17 or 5 mm***	***Increasing Expansion Angle***	***Ogive to 2.35°***
Section	3.2.2, 3.4	3.2.3	***3.2.3***	***3.3.1***	***3.3.2***

Table 1 Glass Nozzle Designs [7]

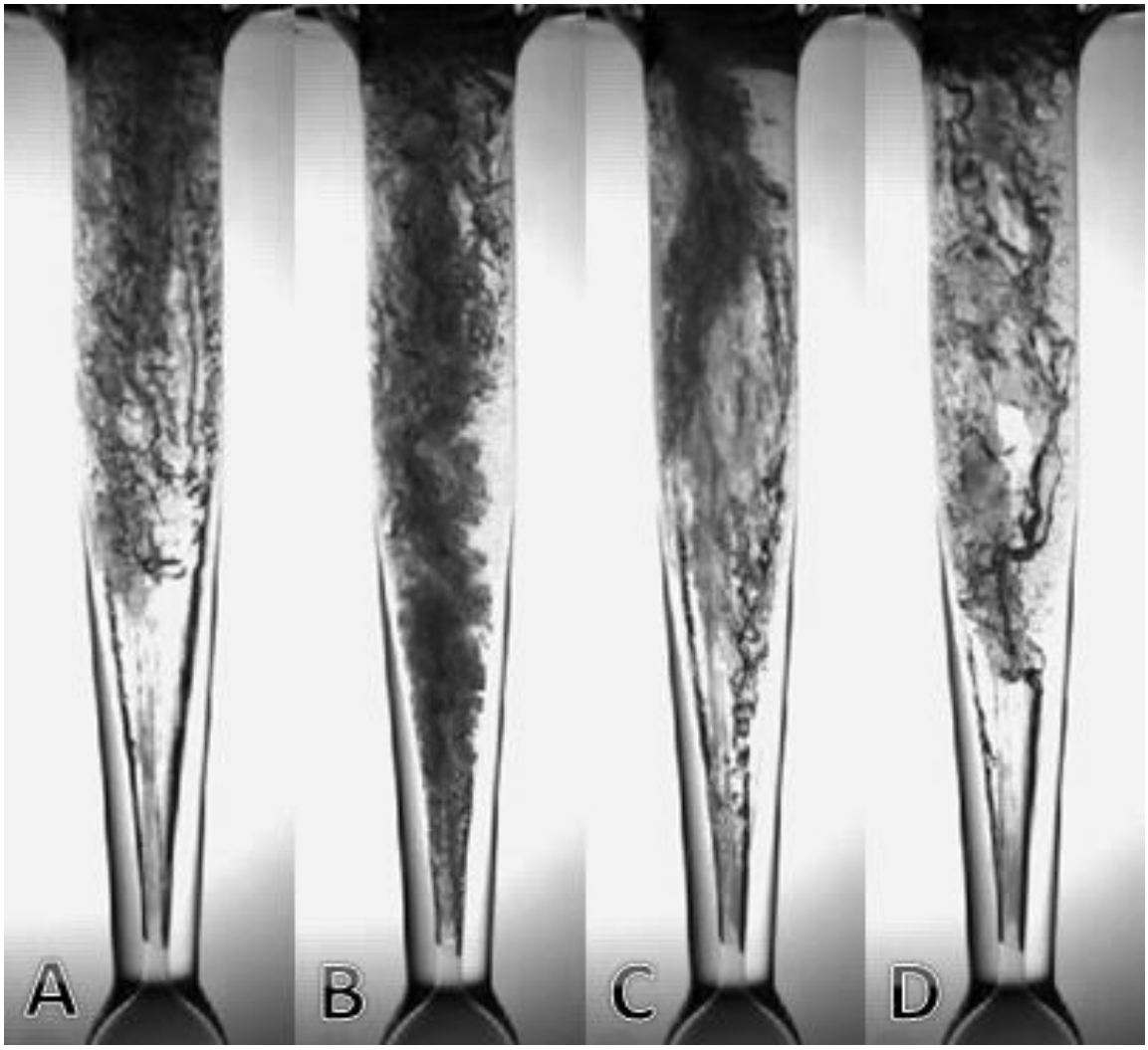

Figure 3.1 Expansion nozzle flow visualization

The first image in Figure 3.1 shows that the attached wall cavitation occurred at the beginning of the flow downstream of the throat. It also shows a region of separated flow, filled with vapor, and reveals variations in the flow pattern as well as fluctuations at the end of the cavitation. The next image shows that the cavitation changed from being attached to the wall to a cloud cavitation. It shows cloud of vapors in the middle surrounded by water on the walls. It occurs when there is an increase in the expansion angle, and then the vapor cloud takes over the entire nozzle for about a 100 frames. In the next image, it is observed that the cloud cavitation collapses downward and fills up the region, which had the cloud cavitation, with a mixture of liquid and vapor.

The second nozzle used in the experiments was nozzle 9 in Table 1, which is called the ogive nozzle. It was designed to have an ogive expansion with a very sudden expansion at the throat. Throat diameter is 2.5 mm and then suddenly expands to 3 mm; converging side geometry is bell shape, which is similar to the expansion nozzle. The same lens and frame rate, which was used for the expansion nozzle, was used in the ogive nozzle. The inlet temperature, pressure, and flow rate in the system were 30 C°, 44 psia, and 38 g/s, respectively.

Figure 3.2 shows that the ogive nozzle having almost the same flow characteristics of the expansion nozzle. The first picture in the figure shows that the attached wall cavitation started at throat and kept ascending to create vapor clouds. Image C shows that the cloud cavitation occurring in the entire nozzle with a small layer of water surrounding it. Then, the cloud cavitation starts to collapse in the nozzle creating a mixture of liquid and vapor around the nozzle.

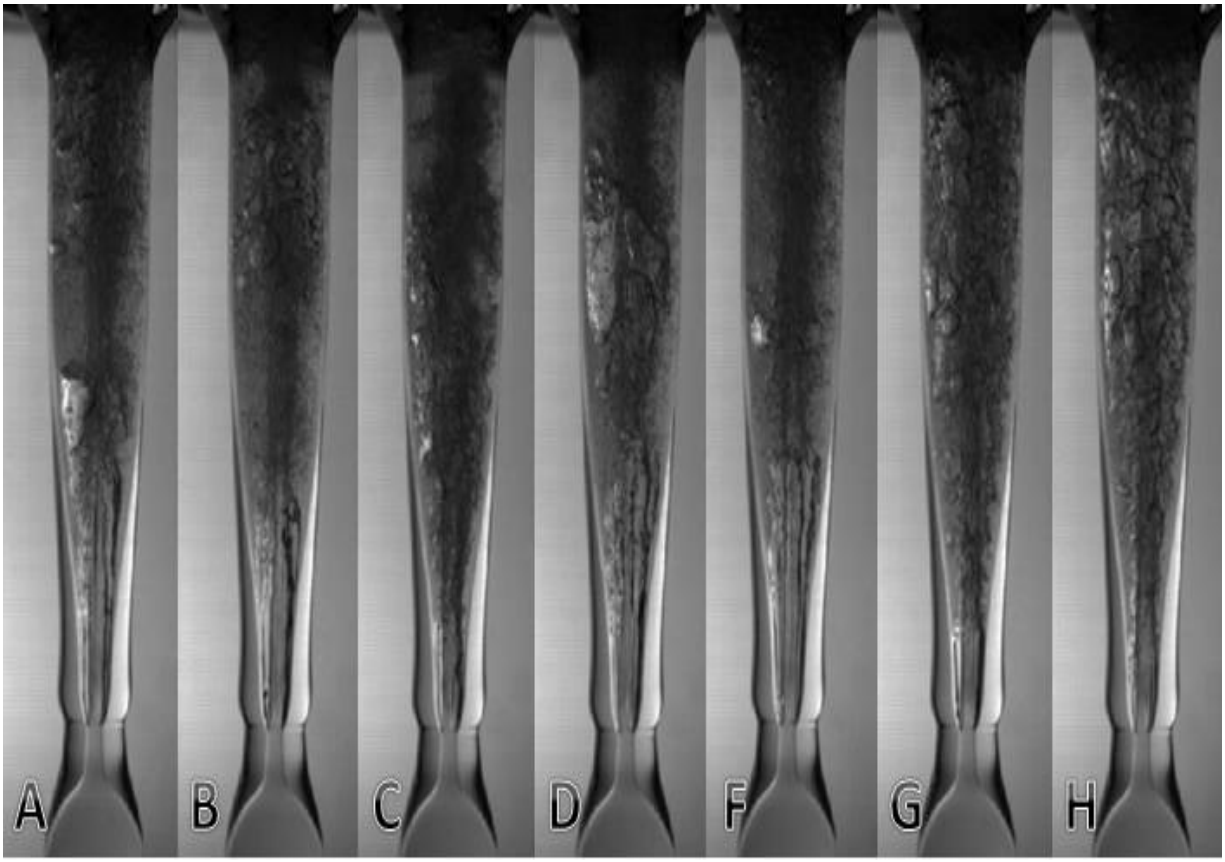

Figure 3.2 Expansion nozzle flow visualization

3.2 Transient Blow Down System

Another type of testing using converging-diverging nozzles was explored, which is called a transient blow down system. The main purpose of the new system was to develop more homogenous flow. Water is driven differently from the continuous flow system. It allows cavitation to be evaluated at outlet conditions that are closer to the vaporization pressure of the water. Different nozzles were tested in the blow-down system; nozzles variations included a 2 mm and a 4 mm throat diameter. Figure 3.3 shows the water in the reservoir while being pumped from the water tank through the nozzle in a free jet and a no jet condition. This section discusses cavitation visualization and measurements of flow temperature using two types of cameras. A high speed camera was used to record the cavitation in different nozzle variations while the water is flown in a free jet and a no jet condition in the reservoir. Another type of cameras used to measure the fluid temperature in the entire nozzle is an Infrared thermal camera.

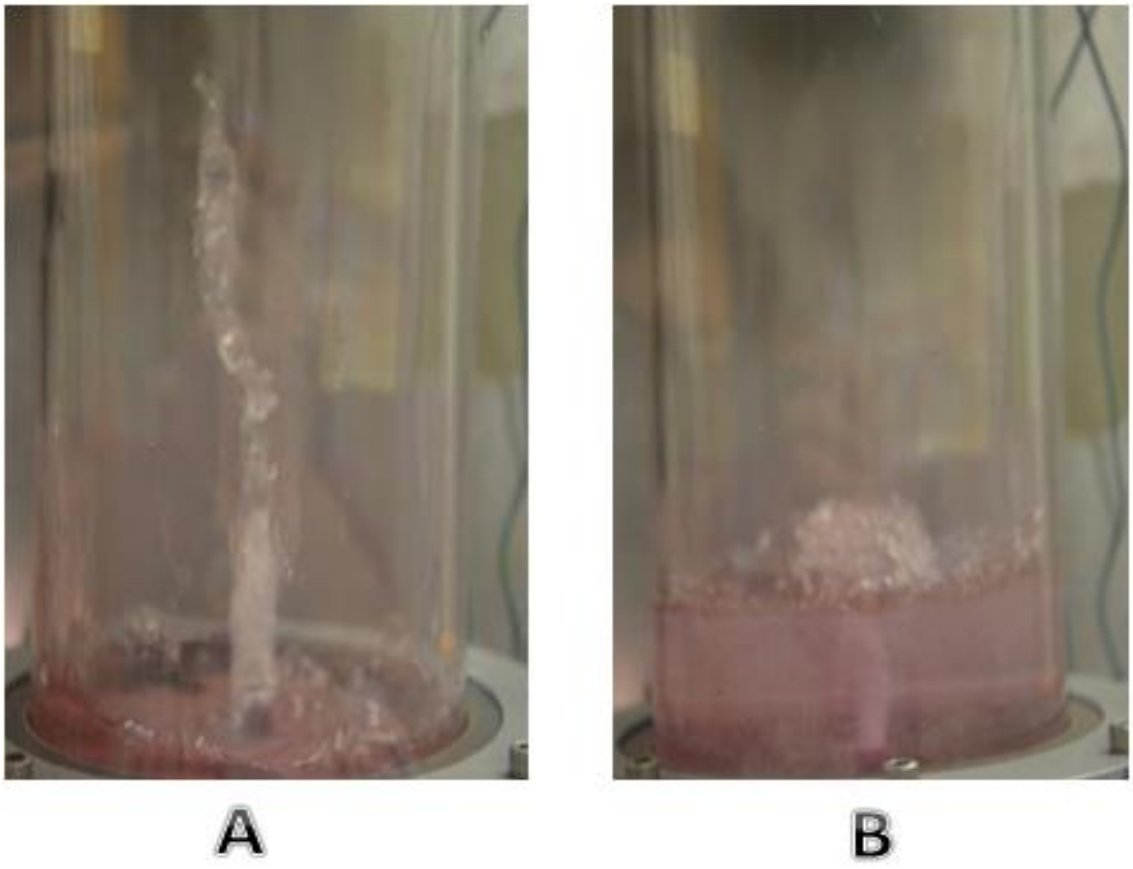

Figure 3.3 Water in the reservoir A. Free jet, B. No jet

3.2.1 High Speed Camera Results

Three different nozzles were tested in the transient blow-down system and were recorded using the high speed camera. Four 2 mm and a one 4 mm throat diameter nozzles were tested. The main focus in this section was on the expansion nozzle, ogive nozzle, and the 4 mm throat diameter nozzle. Nozzles were tested using tap water as the fluid flowing through the system, and then it was decided to degas the water to record different results of cavitation on the nozzles. Results are shown and discussed below.

Figure 3.4 shows the results of the first nozzle that was tested, which is nozzle 2 in Table 1. Figure 3.4 A, shows the images for the free jet testing. It is observed that the traveling bubble cavitation is occurring as long as the flow is in a free jet condition. The traveling bubble cavitation caused by the presence of vapor and gas bubbles in the liquid. On the other hand, Figure 3.4 B, shows cavitation results in a no jet flow condition. It is observed in the first image that the attached wall cavitation is starting to develop at the throat. As the flow continues, the attached wall cavitation starts to collapse which is caused by the traveling bubble cavitation that appears at the same time. In the last image, the attached wall cavitation develops again and remains presented in the entire flow testing.

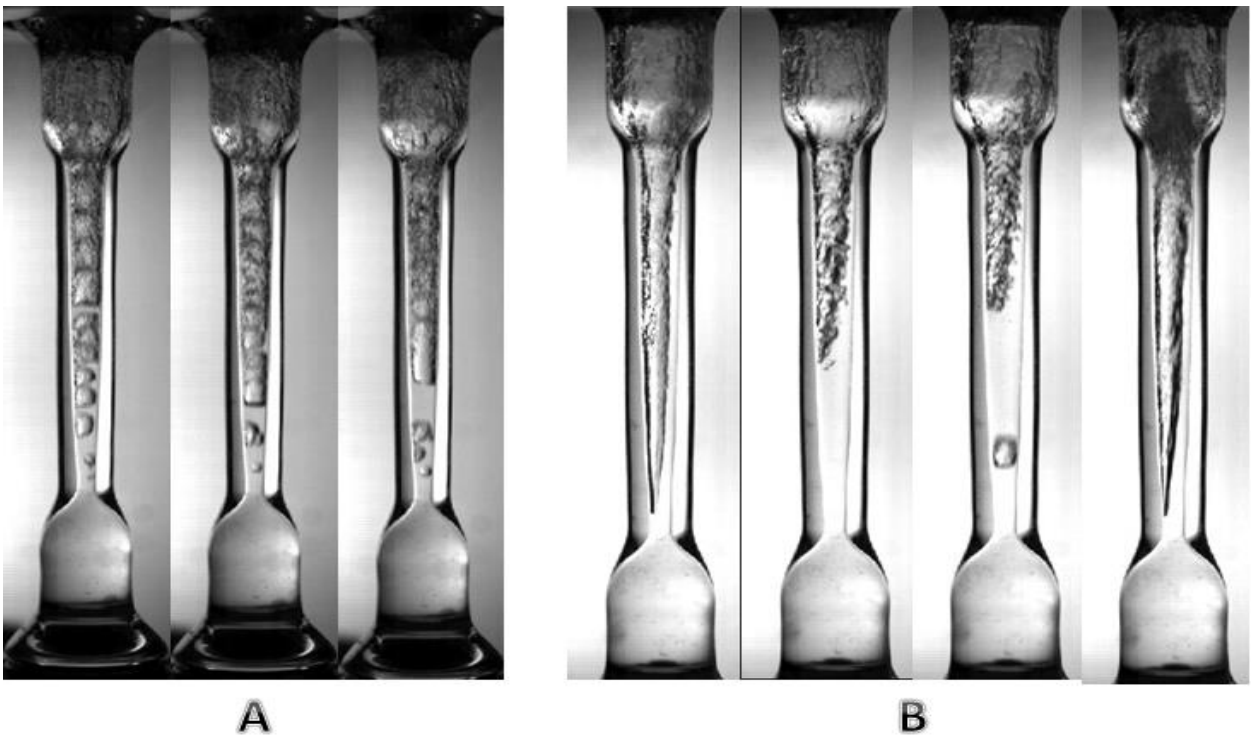

Figure 3.4 Nozzle 2 results A. Free jet, B. No jet

The second nozzle tested was nozzle 5 in Table 1. Figure 3.5 A, shows the results for nozzle 5 in a free jet condition and B shows the results in a no jet condition. The first two images show the vortex cavitation developing an orifice jet, where the pressure in the vortex core is smaller than any point in the flow. In the no jet condition, the first image shows the vortex cavitation in orifice jet surrounded by vapor clouds. The next frame shows a single vapor cloud surrounds the orifice jet, which starts developing around the throat. Small traveling bubble cavitation in the vapor cloud was observed in the next frame. The vapor cloud then started to collapse causing the liquid to develop in the flow.

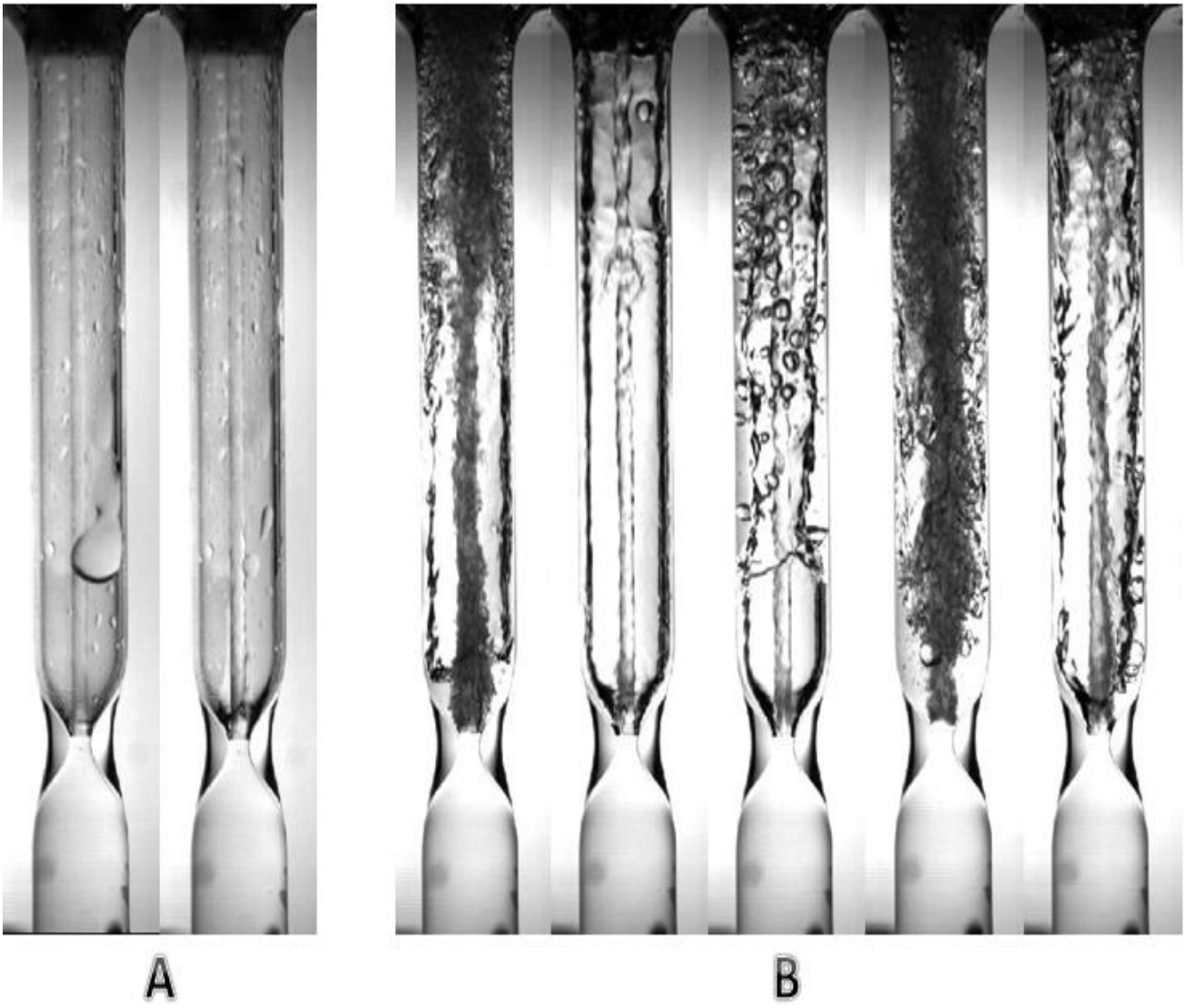

Figure 3.5 Nozzle 5 results A. Free jet, B. No jet

The third nozzle tested was the expansion nozzle, which has been already tested in the continuous flow system. The flow took 20 seconds to use a volume of 600 ml of tap or degassed water, which gives a mass flow rate of 0.03 kg/s. The velocity of the throat in the flow was measured to be 11.8 m/s. Figure 3.6 shows the results of the expansion nozzle in a free jet, a no jet, and a degassed water no jet conditions. The free jet and no jet conditions developed similar cavitation; it is observed that the cavitation was attached in one side of the nozzle, which could be due to the lack of equality when the nozzle was made. Cavitation visualization from the blow-down system test shows similarities with the testing in the continuous flow system. Attached wall cavitation develops, as well as, vapor clouds, and bubbles surrounding the liquid. Then, the water was degassed using a boiling method. When the degassed water temperature equals room temperature, it is used for testing. The results for degassed water testing are shown in Figure 3.4 C. It is observed that the attached wall cavitation developed at the throat, and then a mixture of liquid and vapor was seen on the walls of the nozzle. Vapor clouds and bubbles developed at the end of the expansion section of the nozzle.

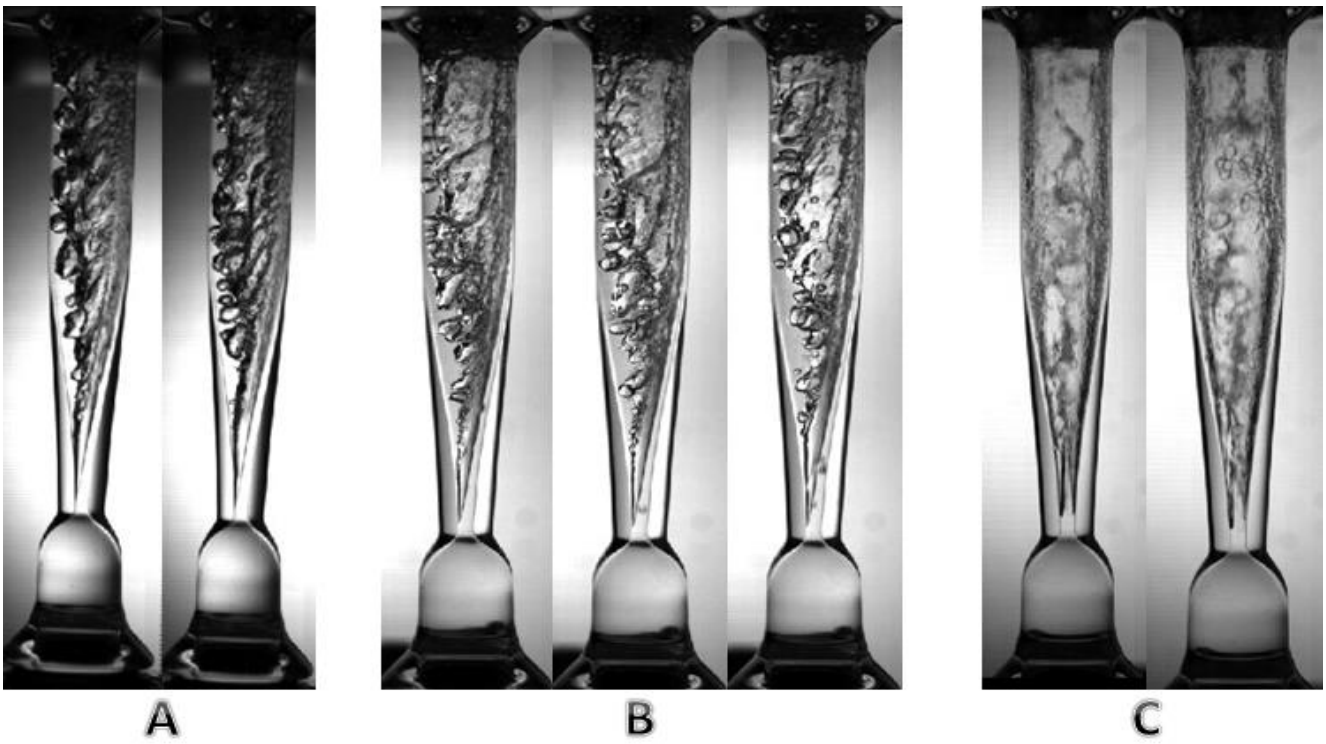

Figure 3.6 Expansion nozzle results A. Free jet, B. No jet, C. Degassed water no jet

Then, a 4 mm throat diameter nozzle was suggested to be used in the testing to improve the homogenous cavitation development. In this nozzle, the flow took a factor of 5 less time than the 2 mm nozzles to flow. The flow took 4 seconds to use a volume of 600 ml of tap or degassed water, which gives a mass flow rate of 0.15 kg/s. The velocity of the throat in the flow was measured to be 9.38 m/s. Figure 3.7 shows the results of the 4 mm throat diameter nozzle in a free jet, a no jet, and a degassed water no jet conditions. It also shows that the cavitation development is identical in all conditions. Attached wall cavitation is seen with a turbulent mix of vapor and gas in the liquid flown on the walls.

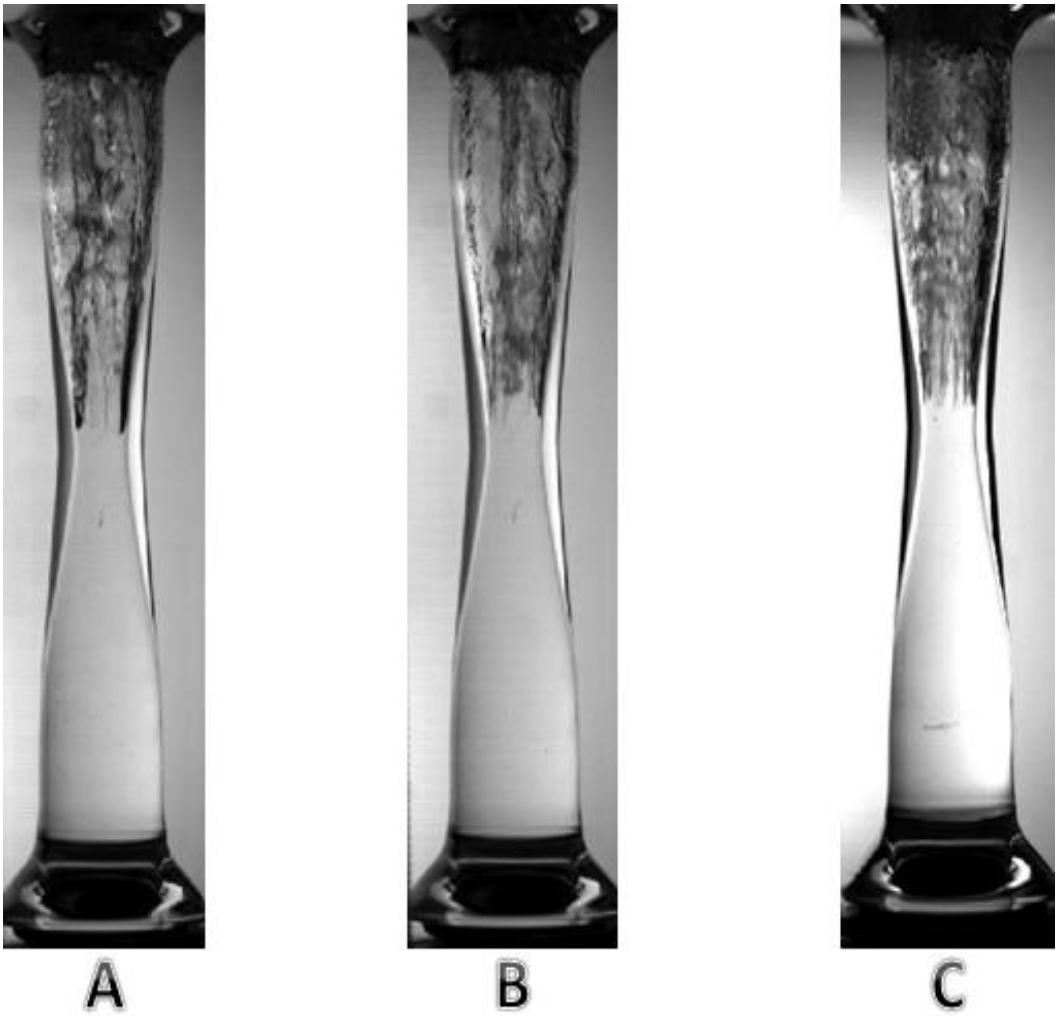

Figure 3.7 4 mm nozzle results A. Free jet, B. No jet, C. Degassed water no jet

The expansion nozzle broke, therefore further tests stopped on the nozzle. The expansion nozzle was replaced by the ogive nozzle. The ogive nozzle geometry was discussed previously in the continuous system flow. The flow took 30.8 seconds to use a volume of 600 ml of tap or degassed water, which gives a mass flow rate of 0.02 kg/s. The velocity of the throat in the flow was measured to be 3.97 m/s. Figure 3.8 show the results of the ogive nozzle in a no jet and degassed water no jet conditions. The first images show that the cavitation has the same characteristics of the testing in the continuous flow system. Attached wall cavitation is seen at the throat and vapor cloud at the expansion location. It was observed that the vapor cloud collapse and an orifice jet developed with attached wall cavitation on the expansion region. After degassing the water, cavitation in the system is just an orifice jet with vapor bubbles surrounding it. At some point in the flow, a mixture of liquid and vapor develops then collapse to create attached wall cavitation.

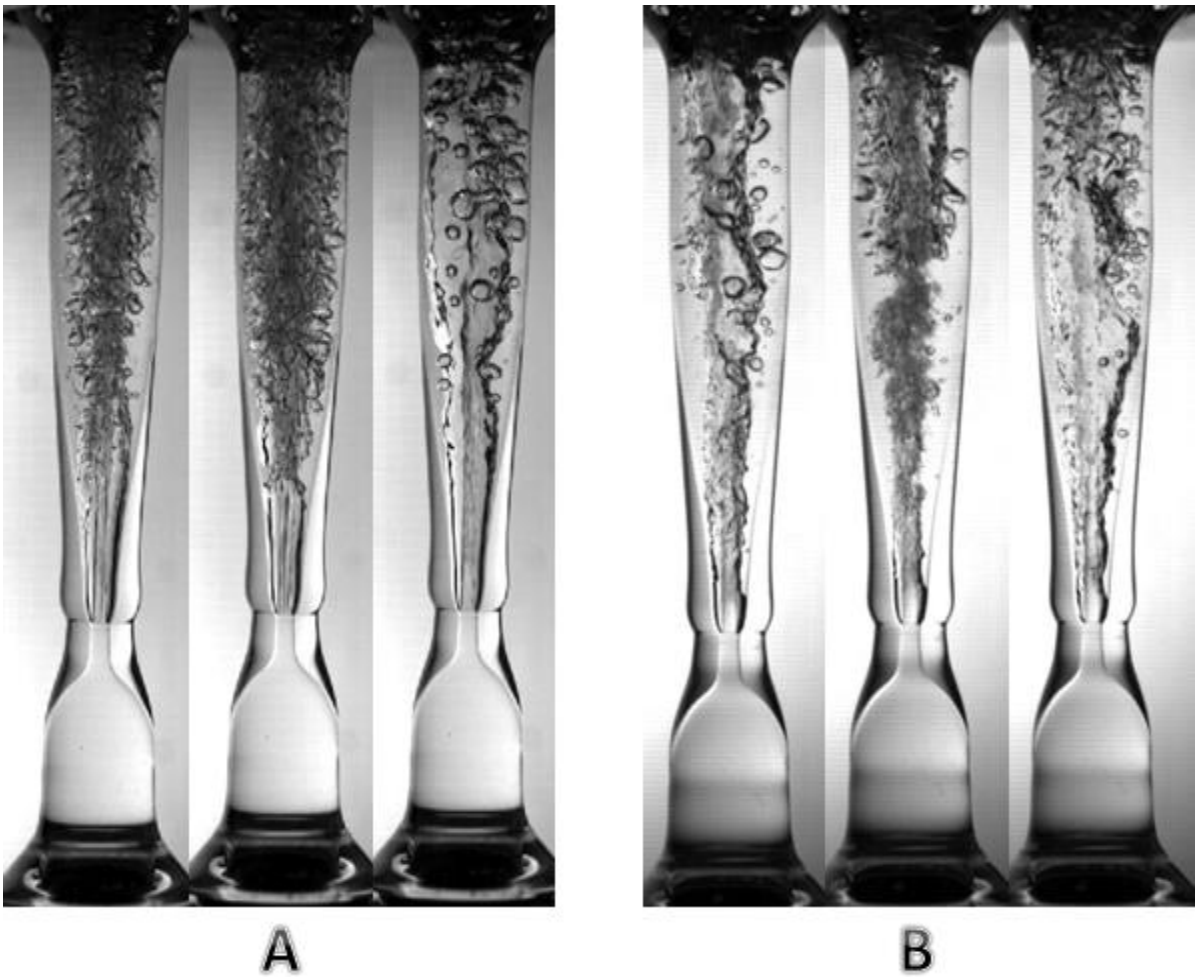

Figure 3.8 Ogive nozzle results A. No jet, B. Degassed water no jet

3.2.1 Thermal Infrared Camera Results

After testing all the nozzles in the transient blow-down system using the high speed camera, the next step followed was the use of a thermal infrared camera to investigate the temperature measurements of the water flowing in the system. Two different nozzles were tested using the thermal camera, the ogive nozzle and the 4 mm nozzle. Calibration of the thermal camera on a beaker, that has tap water, was recommended for having ideal results. Table 2 shows the results for the calibration of the thermal camera on the beaker. Figure 3.9 shows the calibration test using the thermal camera and beaker. In the first and second test, the thermal camera was directed to the beaker surface without filters, temperature values did not match. A tape was used on the beaker surface and then once again the camera was recalibrated, values matched.

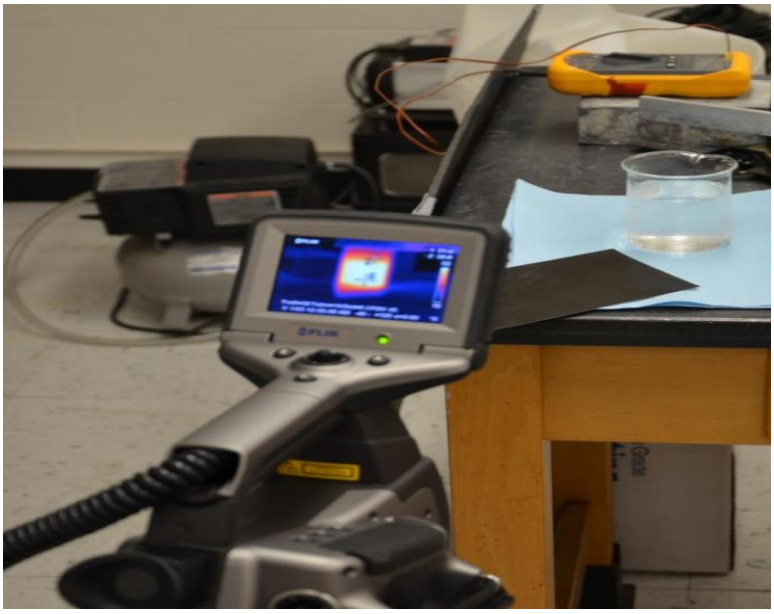

Figure 3.9 Calibration test of the thermal camera

	Test 1	Test 2	Test 3
Beaker temperature	22.8 C^o	16 C^o	16 C^o
Camera Result	15 C^o	7 C^o	15.8 C^o

Table 2 Calibration results

The first nozzle tested was the ogive nozzle. Three tests were done on the ogive nozzle, temperature variations data was recorded during the operation. Table 3 shows the results of the three tests. In the first and second test, water temperature was measured using a thermocouple while the water was in the reservoir before flowing through the nozzle. The first test results were taken 20 seconds after the start of the flow going through the nozzle, second test was taken 75 seconds after. In the third test, water was pumped in the system until the nozzle was filled with water and then the flow stopped, where water temperature was measured. The test was taken 40 seconds after the start of the flow. Figure 3.10 shows the thermal images and final temperature of the fluid for the ogive nozzle while the water was flowing in the blow-down system.

Ogive nozzle	Room Temperature	Water Temperature	Mass Flow Rate	Test Duration
First Test	20 C^o	19.5 C^o	19.5 g/s	20 seconds
Second Test	19 C^o	20.5 C^o	19.5 g/s	75 seconds
Third Test	20 C^o	19.5 C^o	19.5 g/s	40 seconds

Table 3 Test results for ogive nozzle

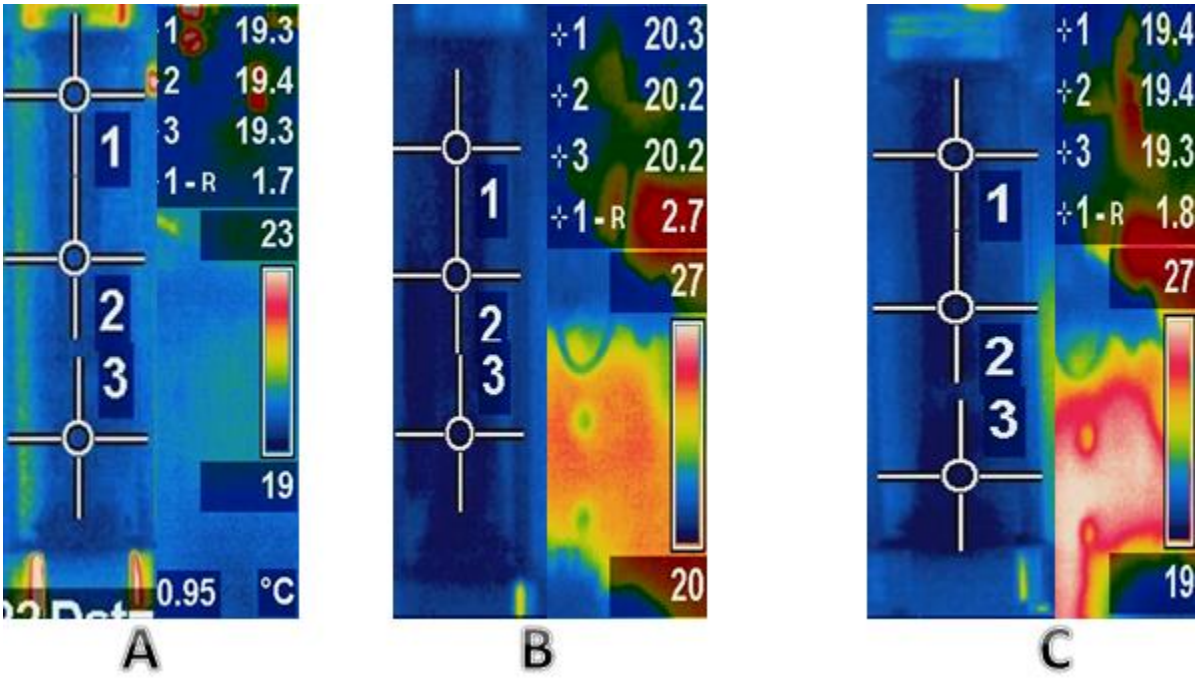

Figure 3.10 Thermal images results A. First test, B. Second test, C. Third test

Then, the 4 mm nozzle was tested; results and data variations were measured using the same procedure as the ogive nozzle, three tests were done as well. Table 4 shows the test results for the 4 mm nozzle. Figure 3.11 shows the thermal images and the fluid final temperature for the 4 mm nozzle while the water was flowing in the blow-down system.

4 mm nozzle	Room Temperature	Water Temperature	Mass Flow Rate	Test Duration
First Test	19.5 C°	19 C°	150 g/s	10-15 seconds
Second Test	19 C°	20.5 C°	150 g/s	25-30 seconds
Third Test	19.5 C°	19 C°	150 g/s	20 seconds

Table 4 Test results for 4 mm nozzle

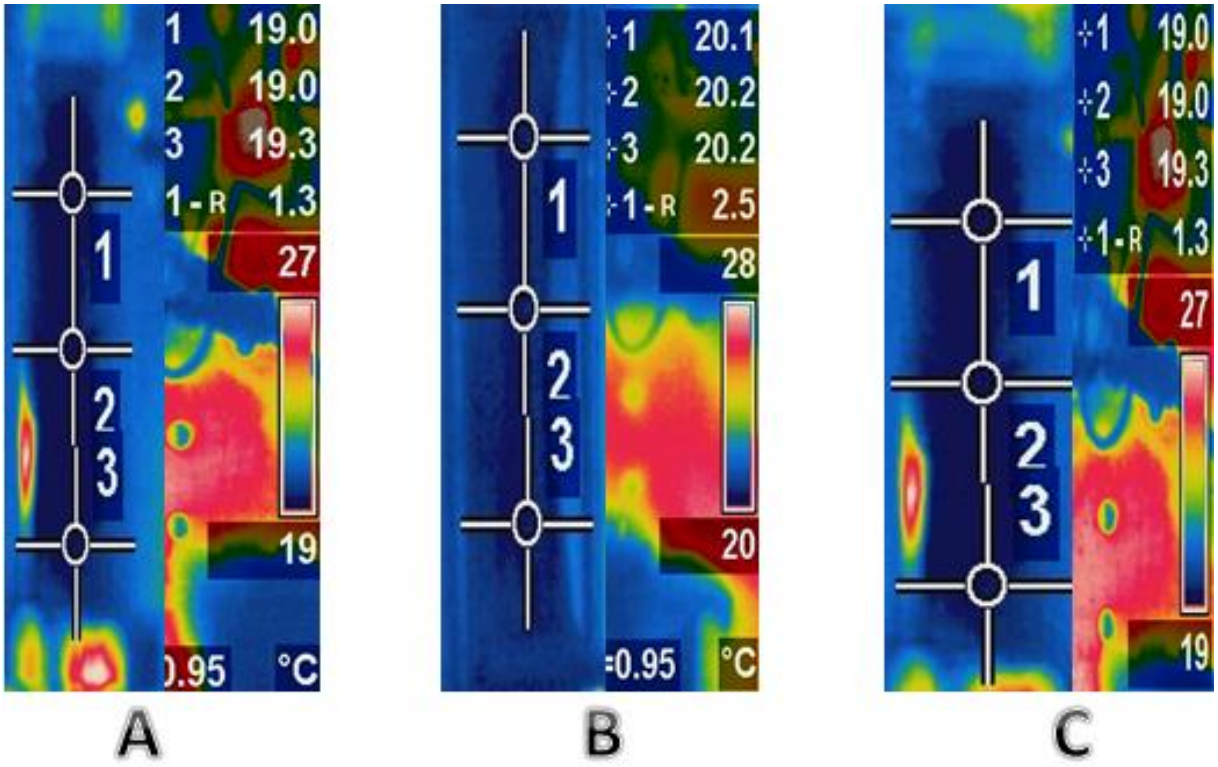

Figure 3.11 Thermal images results A. First test, B. Second test, C. Third test

3.3 Piezoelectric System

Alternative types of nucleation that supplemented this research were investigated. Acoustic cavitation is a possible way of inducing nucleation and create homogenous flow away from the walls. A piezoelectric disk was used to generate an ultrasonic sound wave. The piezoelectric disk was acquired from an ultrasonic humidifier device. The piezoelectric disk was tested on a beaker of water, a test tube inside a container, and a glass nozzle while running the continuous flow system.

While testing the piezoelectric disk, it was observed that the disk was heating up quickly. Table 5 shows the initial temperature, final temperatures, and duration time values of the power resistance and piezo disk on water, contact gel, and air. Figure 3.12 shows the piezo disk and power resistance.

	Power resistance			Piezo disk		
	Water	Contact gel	Air	Water	Contact gel	Air
Initial Temperature	23 C^o	25 C^o	24 C^o	25 C^o	22 C^o	24 C^o
Time	30 s	15 s	10 s	30 s	15 s	10 s
Final Temperature	25 C^o	26 C^o	24.8 C^o	30 C^o	29 C^o	40 C^o

Table 5 The piezoelectric disk and power resistance temperature values

Figure 3.12 Power resistance and piezoelectric disk

The piezoelectric disk was first tested on a beaker of water; ultrasonic contact gel was used to create vapor bubbles through glass. Figure 3.13 shows the piezoelectric disk on the beaker before and after the disk was turned on. It is observed from the figure that the piezoelectric disk was successful in showing volumetric nucleation within the beaker. Vapor bubbles are shown after the disk was turned on.

Figure 3.13 Beaker test before and after the piezoelectric disk was turned on

Another approach of inducing nucleation using the piezoelectric disk was to use a test tube inside a container. The piezoelectric disk was mounted on the side of the plastic square container. The container was filled with water and a test tube was immersed inside the container. Figure 3.14 shows the test tube inside the container before and after the disk was turned on. It is observed that volumetric nucleation occurred within the container with the test tube inside. Figure 3.15 shows the sequences of testing the tube inside the container for 4 minutes. It is observed that bubbles stick to the walls of the container and tube. However, the plastic container started to melt on the opposite side of the piezoelectric device during the operation. Figure 3.16 shows the container melted from the piezoelectric device.

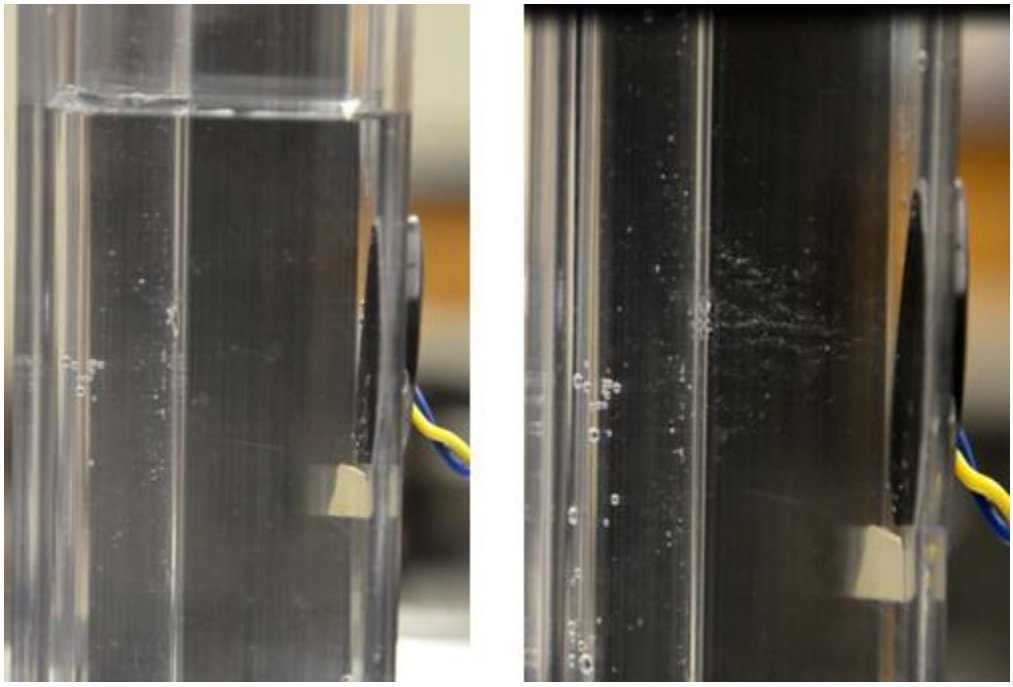

Figure 3.14 Tube test before and after the piezoelectric disk was turned on

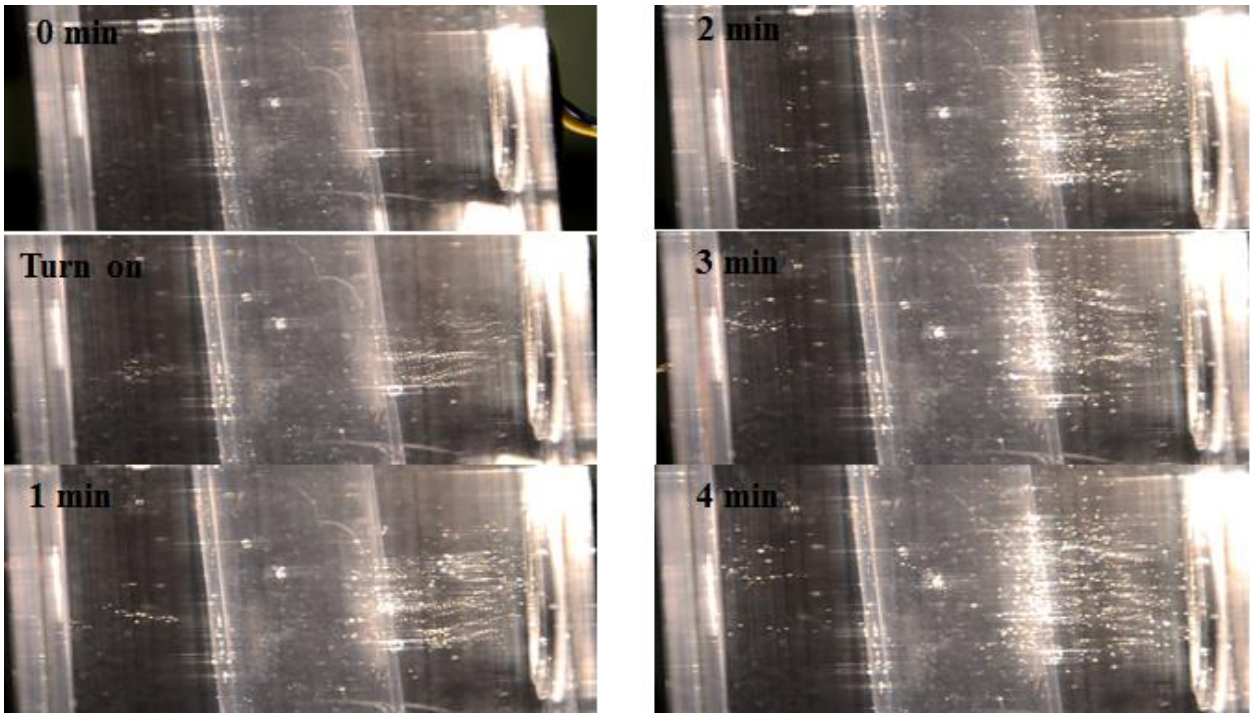

Figure 3.15 The sequences of testing the tube inside the container for 4 minutes

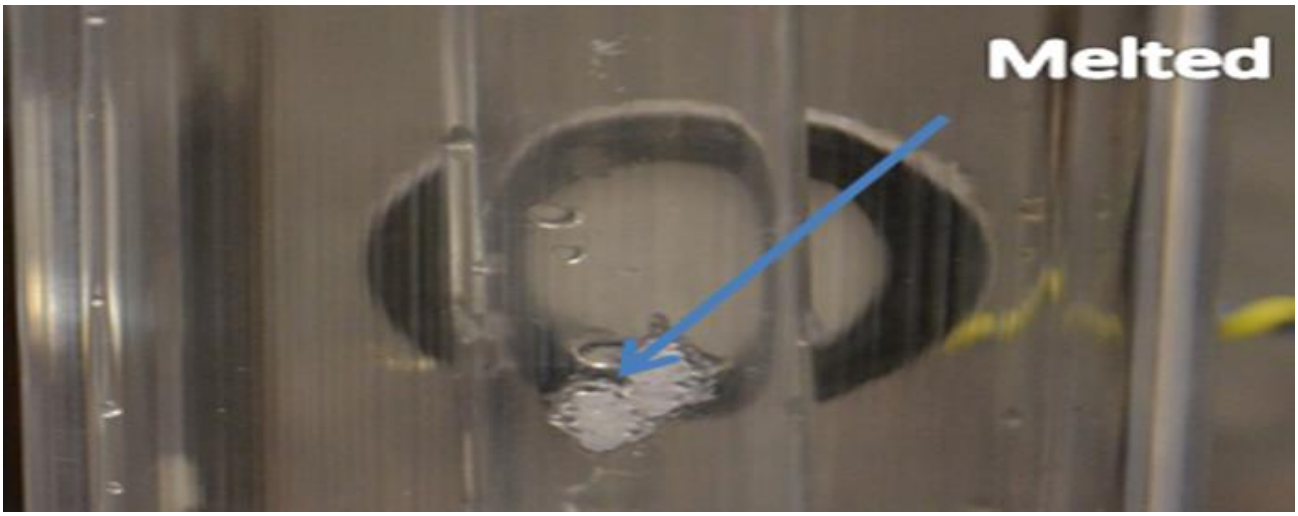

Figure 3.16 The container melted from the piezoelectric device

Finally, the piezoelectric disk was mounted on the side of the glass nozzle while the continuous flow system was running. Figure 3.17 show the disk mounted on the nozzle. The piezoelectric disk heated up quickly and a burning smell was perceived. The piezoelectric device tests were discontinued because of the difficulty of implementing the device on the continuous flow system.

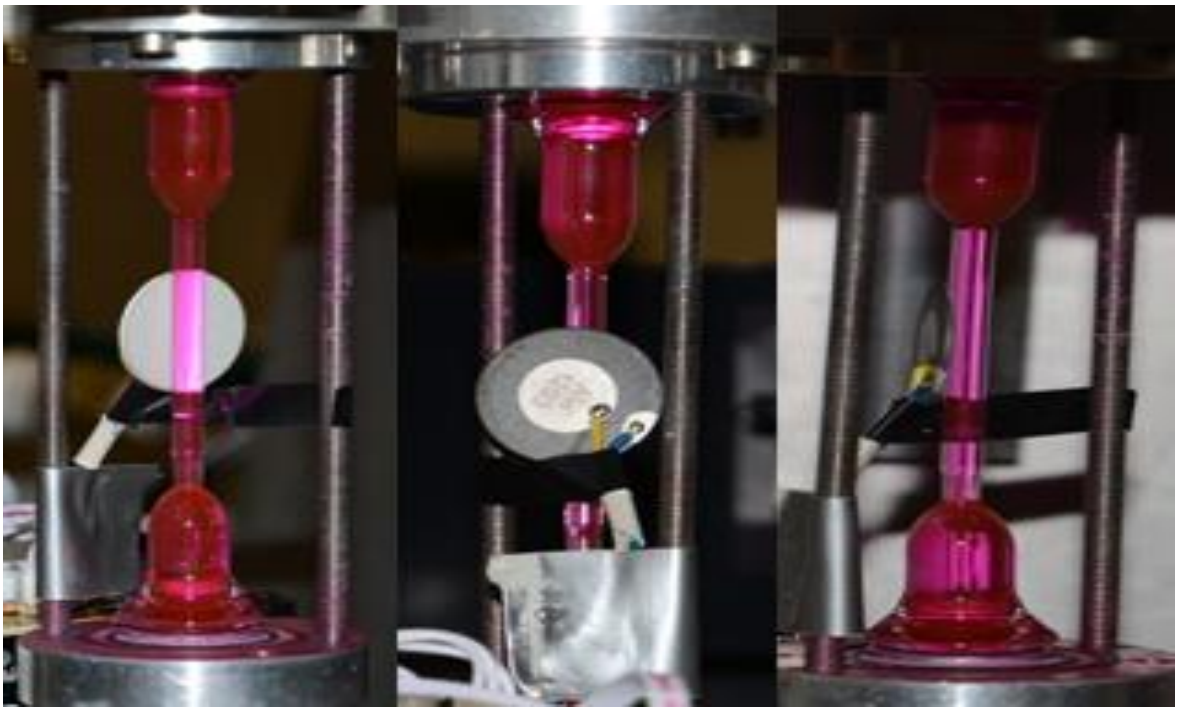

Figure 3.17 The piezoelectric disk mounted on the nozzle

Chapter 4 - Fundamental Knowledge

After testing and visualizing water cavitation in multiple converging-diverging nozzles using different methods of testing, it was decided to take a step back and learn more about some of the basic fundamental knowledge associated with the thermodynamics within the nozzle. Some fluids like R134a have been tested before and results were successful in showing temperature drop in the converging-diverging nozzles. By removing thermal energy from a flowing liquid, cooling (i.e., refrigeration effect) had been observed. The focus of the fundamental knowledge effort was to better understand the reasons behind water experiments not being successful in developing significant cooling results. This chapter will introduce the basic conservation equations, equation of states, and temperature reduction predictions. The chapter will discuss the reason behind water not being a good working fluid, and also address what characteristics are desired in general for a viable coolant.

4.1 Conservation Equations

Conservation equations, known as the governing equations, include three different conservation laws of physics and will be discussed in this section. Figure 4.1 shows the variable cross sectional area of the converging-diverging nozzle, with a stationary control volume shown after the throat, that control volume can be also evaluated at the inlet of the nozzle. Flow in the converging-diverging nozzle is assumed to be incompressible, up to the initiation of cavitation. Fluid is flowing from the left to the right. The throat is designated with subscript t. The equations of conservation of mass, of momentum, and of energy are shown below.

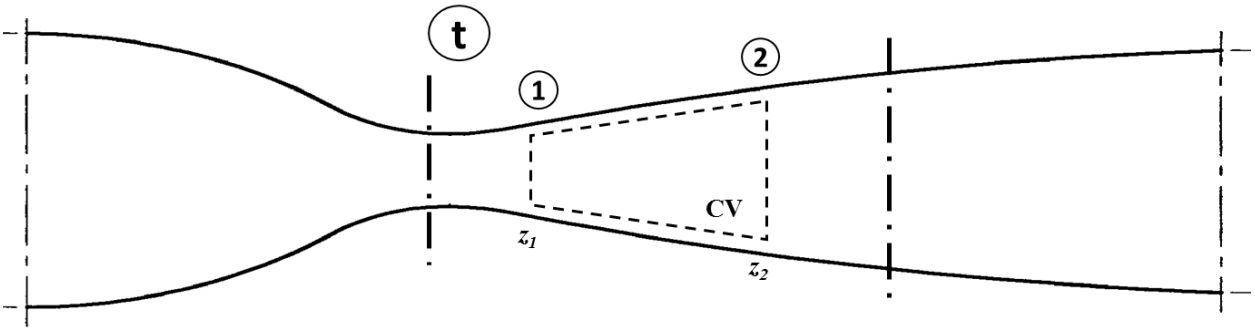

Figure 4.1 Converging-diverging nozzle

4.1.1 Conservation of Mass

The principle of conservation of mass states that any mixture that flows in a nozzle can be developed but the amount of mass entering the nozzle equals the same amount leaving the nozzle over a period of time. In other words, time rate of change of mass inside a control volume (i.e., rate of mass storage) plus the net mass flow through leaving the control surface equals zero. We start with a basic equation for the conservation of mass.

$$\frac{dM}{dt}_{system} = \mathbf{0} \tag{4.1}$$

where M is the mass flow rate and t is the time. Using this relation, the conservation of mass for a fixed control volume and control surface is given in general by

$$\frac{d}{dt}(\iiint \boldsymbol{\rho dv})_{cv} + (\iint \boldsymbol{\rho V.n.dS})_{cs} = \mathbf{0} \tag{4.2}$$

where

$$\boldsymbol{n.dS} = \boldsymbol{dA} \tag{4.3}$$

where ρ is density, *v* is volume, n is an outward unit normal vector, and **V** is velocity vector on the control surface, CS. For steady flows, the mass in the control volume will not change; therefore

$$(\iint \boldsymbol{\rho V.dA})_{cs} = \mathbf{0} \tag{4.4}$$

Assuming one dimensional flow, with uniform velocities across the cross-section, Eqn (4.4) becomes

$$(\iint \boldsymbol{\rho V.dA})_{cs} = \sum \dot{\boldsymbol{m}}_{out} - \sum \dot{\boldsymbol{m}}_{in} = \mathbf{0} \tag{4.5}$$

where

$$\sum \dot{\boldsymbol{m}}_{out} - \sum \dot{\boldsymbol{m}}_{in} = \sum(\boldsymbol{\rho AV})_{out} - \sum(\boldsymbol{\rho AV})_{in} \tag{4.6}$$

for the cross section and control surface in the nozzle we have

$$\dot{m}_2 - \dot{m}_1 = (\rho AV)_2 - (\rho AV)_1 = 0 \quad \textbf{(4.7)}$$

if density is constant we have

$$(AV)_2 - (AV)_1 = 0 \quad \textbf{(4.8)}$$

finally we get a simple relationship for the conservation of mass where the inlet mass flow equals the outlet the mass flow rate

$$\dot{m}_2 = \dot{m}_1 = (\rho AV)_2 = (\rho AV)_1 \quad \textbf{(4.9)}$$

4.1.1 Conservation of Momentum

The momentum principle is a representation of Newton's second law, which states that (for a closed system) the sum of all forces equals the rate of time change of the momentum. Forces on the nozzles can be due to surface forces as pressure and viscous forces, or could be due to body forces, (namely, gravitational forces), which acts on the control volume,. The law states that if an object loses momentum, it will be gained by another object which then the total amount will be constant unless friction is involved. We first introduce Newton's second law for a closed system.

$$\sum F = \frac{dP}{dt} = m \frac{dV}{dt} \quad \textbf{(4.10)}$$

where P is the momentum, *m* is the inertial mass, and V is velocity. Equation (4.10) is easy to apply to particles, but for the case of fluid flowing in a nozzle, it requires modification to account for momentum entering and leaving a specified control volume. For a general open system, the momentum principle as applied to a given control volume, can be expressed as follows:

$$\sum F = (\iiint g\rho dv)_{cv} - (\iint PdA)_{cv} + (\iint \tau dA)_{cv} = \frac{d}{dt}(\iiint \rho . V dv)_{cv} + (\iint V\, \rho V . n . dA)_{cs} \quad \textbf{(4.11)}$$

Where the first term on the right-hand side represent the instantaneous rate of momentum storage within the CV, the second term represent the net rate of change of the momentum through the control volume surface.

For one dimensional uniform velocity flow, a homogenous model, steady states conditions, uniform flow, and ignoring gravitational forces and shear forces we get

$$\left(\iint \boldsymbol{V}\,\boldsymbol{\rho V}.\boldsymbol{n}.\boldsymbol{dS}\right)_{\boldsymbol{cs}} = \sum \dot{\boldsymbol{m}}_{\boldsymbol{out}}\boldsymbol{V}_{\boldsymbol{out}} - \sum \dot{\boldsymbol{m}}_{\boldsymbol{in}}\boldsymbol{V}_{\boldsymbol{in}} \tag{4.12}$$

which gives

$$\sum \dot{\boldsymbol{m}}_{\boldsymbol{out}}\boldsymbol{V}_{\boldsymbol{out}} - \sum \dot{\boldsymbol{m}}_{\boldsymbol{in}}\boldsymbol{V}_{\boldsymbol{in}} = \boldsymbol{V_2}(\boldsymbol{\rho AV})_2 - \boldsymbol{V_1}(\boldsymbol{\rho AV})_1 \tag{4.13}$$

and

$$\sum \boldsymbol{F} = (\boldsymbol{p_1A_1} - \boldsymbol{p_2A_2} - \int_{z_1}^{z_2} \boldsymbol{p}\left(\frac{\boldsymbol{dA}}{\boldsymbol{dz}}\right)\boldsymbol{dz}) \tag{4.14}$$

Combining (4.11), (4.12), (4.13), and (4.14) we get

$$\boldsymbol{V_2}(\boldsymbol{\rho AV})_2 - \boldsymbol{V_1}(\boldsymbol{\rho AV})_1 = (\boldsymbol{p_1A_1} - \boldsymbol{p_2A_2} - \int_{z_1}^{z_2} \boldsymbol{p}\left(\frac{\boldsymbol{dA}}{\boldsymbol{dz}}\right)\boldsymbol{dz}) \tag{4.15}$$

4.1.1 Conservation of Energy

The principle of the conservation of energy represents the first law of thermodynamics, which states that (for a closed system) any increase in internal energy equals the heat added to the system minus the work done by the system. For a general open system control volume (and associated control surface) we get

$$\frac{\boldsymbol{d}}{\boldsymbol{dt}}\left(\iiint \boldsymbol{e}\,\boldsymbol{\rho dv}\right)_{\boldsymbol{cv}} + \left(\iint \left(\frac{\boldsymbol{P}}{\boldsymbol{\rho}} + \boldsymbol{e}\right)\boldsymbol{\rho V}.\boldsymbol{n}.\boldsymbol{dA}\right)_{\boldsymbol{cs}} = \dot{\boldsymbol{Q}}_{\boldsymbol{cv}} - \dot{\boldsymbol{W}}_{\boldsymbol{cv}} \tag{4.16}$$

where

$$\boldsymbol{e} = \left(\boldsymbol{h} + \frac{\boldsymbol{1}}{\boldsymbol{2}}\boldsymbol{V^2} + \boldsymbol{gz}\right) \tag{4.17}$$

where e is total energy per unit mass, $\dot{\boldsymbol{Q}}_{\boldsymbol{cv}}$ is the rate of heat added to the system, $\dot{\boldsymbol{W}}_{\boldsymbol{cv}}$ is the rate of work done by the system. Total energy equals the kinetic energy plus the potential energy

plus the internal energy. For steady states conditions, the first term drops out and Eqn (4.16) becomes

$$\left(\iint \left(\frac{P}{\rho} + e\right)\rho \boldsymbol{V}.\boldsymbol{n}.\boldsymbol{dA}\right)_{cs} = \dot{Q}_{cv} - \dot{W}_{cv} \quad \textbf{(4.18)}$$

Assuming that the nozzle has adiabatic walls, and there is no work (by friction), we get

$$\sum\left(\frac{P}{\rho} + e\right)\rho \boldsymbol{V}.\boldsymbol{n}.\boldsymbol{dA} = 0 \quad \textbf{(4.19)}$$

Combining (4.17) and (4.19), for a steady flow we get

$$(\rho AV)_2\left(h_2 + \frac{1}{2}V_2^2 + gz_2\right) - (\rho AV)_1\left(h_1 + \frac{1}{2}V_1^2 + gz_1\right) = 0 \quad \textbf{(4.20)}$$

since mass flow rates are equals it simplifies to:

$$\left(h_2 + \frac{1}{2}V_2^2 + gz_2\right) - \left(h_1 + \frac{1}{2}V_1^2 + gz_1\right) = 0 \quad \textbf{(4.20a)}$$

4.2 Equation of State (EOS)

The Equation of State (EOS) defines the thermodynamic state of a material under given conditions; it describes gasses, fluids, and solids. Multiple equations of state have been studied in this research. The main focus was on the following two equations: van der Waals and Peng Robinson. Reduced pressure and reduced temperature are useful relative thermodynamic properties that were used in the analysis. The van der Walls EOS perfectly obeys the so-called Law of Corresponding States, which indicates that there is a general relationship among thermodynamic properties when expressed in terms of the reduced quantities. Figure 4.2 shows a typical coexistence curve generated from the equation of state isotherms. This EOS has the same general form as the van der Waal or Peng Robinson equation of state, for a constant temperature in a pressure verses specific volume plot. The Critical point and spinodal point is (along with the general liquid spinodal line) are shown as well.

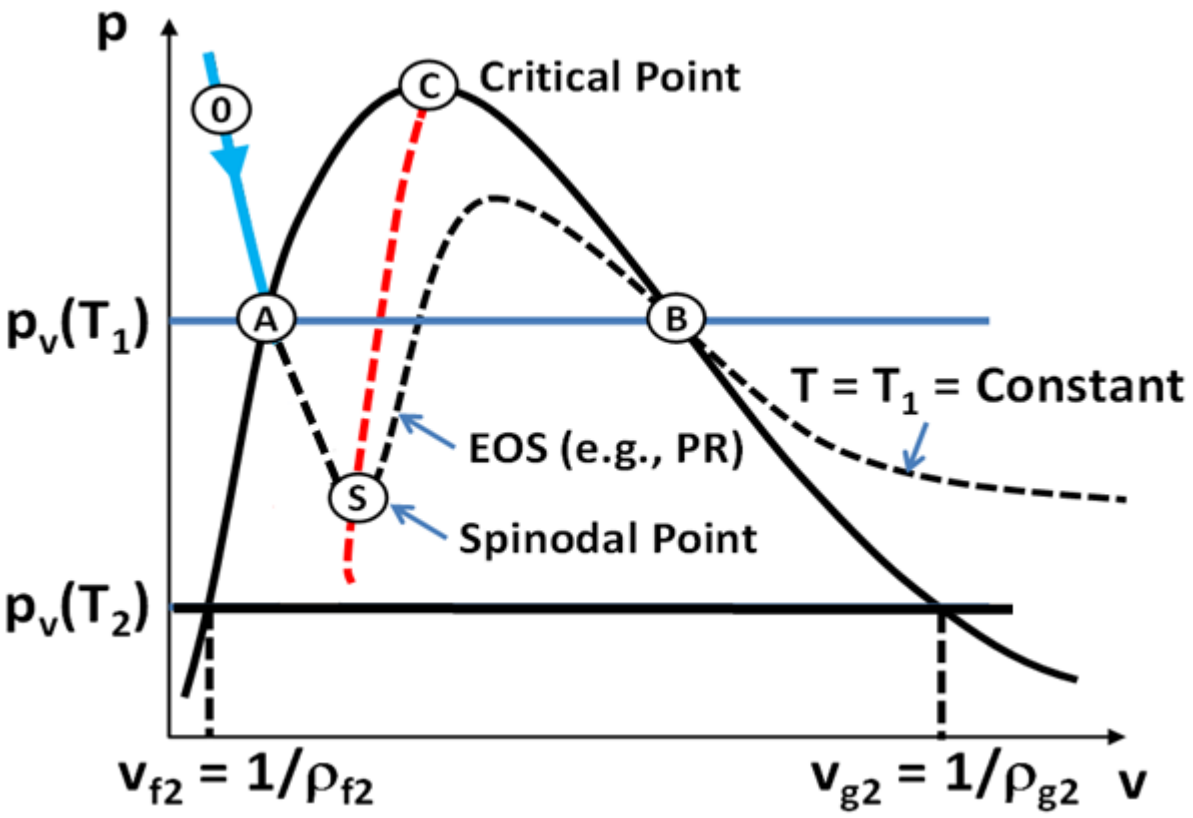

Figure 4.2 Coexistence and spinodal curves with a constant temperature isotherm

4.2.1 Van der Waals Equation of State

Van der Waals equation of state is used to predict the transition from vapor to liquid or liquid to vapor; that is, the mixture region envelope or vapor dome as it is sometimes called. At a given temperature, it yields a relationship between pressure and density (or specific volume). For a given saturation pressure, the corresponding saturated liquid and vapor specific volume values are determined as the points where the VDW EOS crosses the given saturation pressure level, such that the areas above and below this pressure level are equal corresponding points A and B in Figure 4.2. The integral from A to B at a constant temperature equals to zero such that the areas under the curves are equal. The specific volume values get closer and closer when the temperature increases. At high temperatures the equation only gives one real root, which corresponds to the location of the critical point. The van der Waals equation is shown below

$$P = \frac{RT}{v-b} - \frac{a}{v^2} \quad \textbf{(4.21)}$$

where P is the absolute pressure, *v* is the specific volume, R is the ideal gas constant, *a* and *b* are empirical constants, which are different from fluid to fluid and defined as

$$a = 12\,\frac{R^2 {T_c}^2}{64 P_c} \quad , \quad b = \frac{RT_c}{8P_c} \quad \textbf{(4.22)}$$

Van der Waals equation was used to solve for the liquid and vapor specific volumes to get the liquid-gas coexistence curve in a pressure and specific volume plot. Also, the equation was solved for the liquid and vapor spinodal lines. Plots were used to understand the fundamental thermodynamics of the fluids used in existing two phase flow experiments. Using Mathcad software, spinodal lines were found by determining the set of all points in the van der Waals equation; where the slope of the pressure versus volume relation is zero. The derivative of van der- Waals equation is

$$\frac{\partial P}{\partial v} = \frac{-RT}{(v-b)^2} - \frac{2a}{v^3} \quad \textbf{(4.23)}$$

where

$$\frac{\partial P}{\partial v} = 0 \quad \text{At both the liquid and vapor spinodal lines} \quad \textbf{(4.24)}$$

Figure 4.3 show a plot of the van der Waals EOS in terms of pressure versus specific volume plot, for water at a temperature of 600 K. The plot shows a pressure line crossing the liquid-vapor coexistence curve. Specific volumes values are the points where that pressure line crosses the curve such that the areas above and below the enclosed regions are equal.

The work on the van der Waals EOS represents perhaps the simplest EOS for a fluid; however, it has only limited capability when used to represent properties of other fluids of interest such as R134a. Another EOS, known for improved agreement with fluid properties of R134a and other refrigerants, is the Peng Robinson EOS.

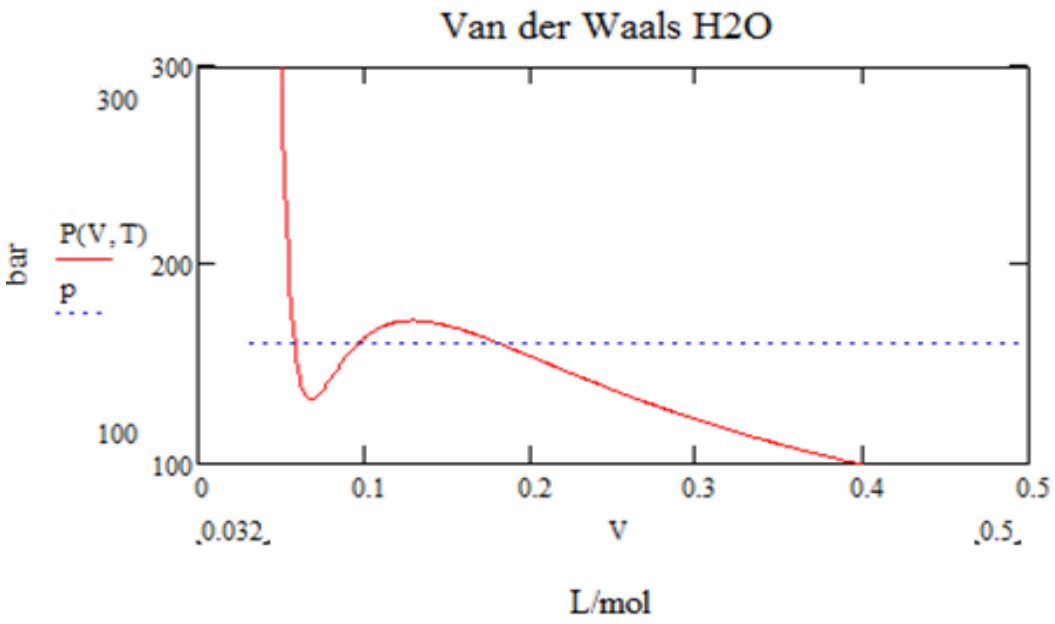

Figure 4.3 Van der Waals equation EOS for water at temperature T = 600 K

4.2.2 Peng Robinson Equation of State

The Peng Robinson (PR) EOS is a general cubic EOS, giving pressure as a function of specific volume for a given temperature similar to the van der Waals relation. The PR EOS can similarly yield both the saturated liquid and saturated vapor lines (i.e., the coexistence liquid-vapor curve) as well as the spinodal lines. Different fluids were investigated using the PR EOS, especially water, R134a, and R123a. However, the main focus was on R134a and water. The principle of corresponding states was introduced, similar to what was done with the van der waals EOS, by expressing the thermodynamic variables in terms of reduced state (or relative) state variables. Reduced pressure, reduced temperature, and reduced volume were used to study the liquid metastability limits for these fluids. The Peng Robinson EOS is given by

$$\boldsymbol{P = \frac{RT}{v-b} - \frac{a\alpha}{v(v+b)+b(v-b)}} \qquad \textbf{(4.25)}$$

where T is the absolute temperature, a and b are

$$\boldsymbol{a = 0.45724\ \frac{R^2 {T_c}^2}{P_c}} \quad , \quad \boldsymbol{b = 0.0778\ \frac{R^2 {T_c}^2}{P_c}} \qquad \textbf{(4.26)}$$

where R is the universal gas constant, P_c is the critical pressure, T_c is the critical temperature**.** The parameter α given by

$$\boldsymbol{\alpha = \left[1 + \kappa \left(1 - \sqrt{\frac{T}{T_c}} \right) \right]^2} \qquad \textbf{(4.27)}$$

where $\boldsymbol{\kappa}$ is a dimensionless parameter defined in terms of ω, which is called the acentric factor and is related to the compressibility of the gas.

$$\kappa = 0.37464 + 1.54226\omega - 0.26992\omega^2 \qquad \text{When } \omega \leq 0.49 \qquad \textbf{(4.28)}$$

$$\kappa = 0.379642 + 1.48503\omega - 0.164423\omega^2 + 0.01666\omega^3 \qquad \text{When } \omega > 0.49 \qquad \textbf{(4.29)}$$

The Peng Robinson equation was used to plot a general coexistence curve, based on the assumption of corresponding states, and to obtain general normalized liquid and vapor spinodal lines. Three fluids were explored using the Peng Robinson equation: R134a, water, and R123. Results showed that the coexistence curves and the corresponding spinodal lines have somewhat different shapes. This stems from the unique values of the acentric factor for each fluid. As a result, the PR EOS can only approximately predict the critical point location. Hence, the coexistence curve and the spinodal lines generally do not match at the critical point location. Figure 4.4 shows plots for all three fluids of coexistence and spinodal curves in reduced state variables. To improve the match at the critical point (and hence better represent the behavior of the PR over a range of conditions, a "shift" of the spinodal curve was applied matched the coexistence curve at the critical point. All the spinodal curves were moved to the left by slightly different factor. The R134a spinodal data was multiplied by a factor of 0.855, the R123 spinodal data was multiplied by a factor of 0.886, and the water spinodal data was multiplied by a factor of 0.759. Figure 4.5 shows shifted plots for all the fluids coexistence and spinodal curves in reduced states variables. All three have different curves shapes when plotted as pressure versus specific volume axes. On the other hand, all fluids have nearly universal shapes when expressed in reduced state variables. This is illustrated in Figure 4.6 (a), which shows the universal coexistence and shifted spinodal curves for all three fluids plotted together using the same

reduced pressure and specific volume variables. Similarly, Figure 4.6 (b) shows nearly universal agreement for the coexistence curves in terms of reduced pressure and temperature variables.

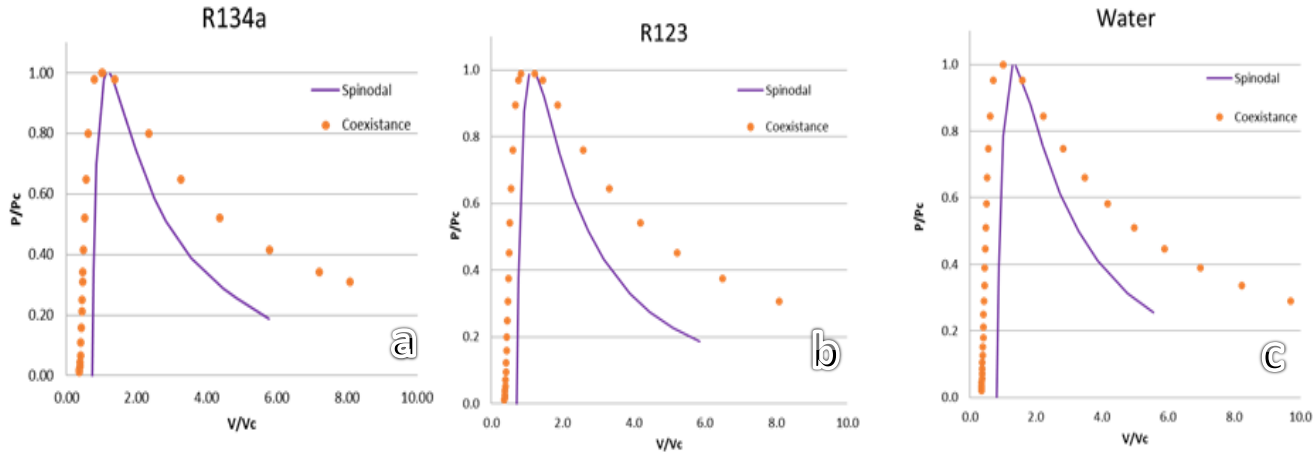

Figure 4.4 Coexistence and spinodal curves for a. R134a, b. R123, c. Water

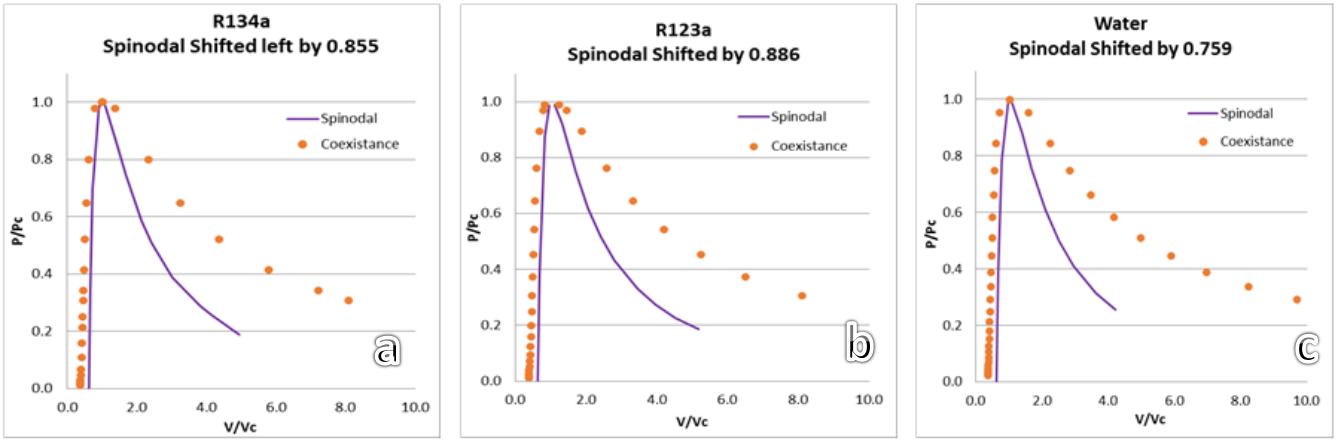

Figure 4.5 Coexistence and shifted spinodal curves for a. R134a, b. R123, c. Water

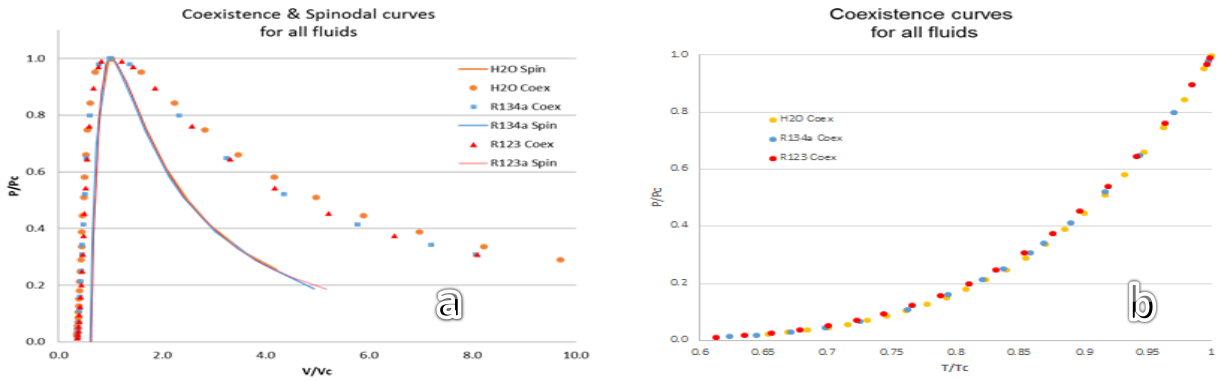

Figure 4.6 a. Coexistence and shifted spinodal curves, b. Coexistence curves

4.3 Temperature Reduction Calculations

In a two phase flow, a temperature drop can occur when the gas phase nucleates, since this process generally requires energy transfer to change the liquid to gas phase. When the environment does not supply any heat, this temperature drop would have a maximum value. Since there was not any measurable temperature drop recorded in the water flow refrigeration experiments, a simple theory was developed in an attempt to understand the thermodynamics behind this lack of temperature drop. Two basic theories were formulated to determine the temperature reduction and will be discussed in this section: (1), a static theory, and (2) a dynamic theory.

4.3.1 Static Calculation

Any incompressible liquid has a lower pressure than the environment pressure due to Bernoulli equation effect. Many variables affect the temperature reduction in flowing fluid. One of the factors is latent heat of vaporization which is required for the liquid to change to gas using heat coming from the fluid. Other factors are the quality and the heat capacity of liquid which relates to gas nucleation and the amount of liquid converted to gas. A thermodynamics theory introduces an equation to calculate the temperature drop that is shown below, details shown in appendix D:

$$\Delta \boldsymbol{T_{max}} = \frac{\boldsymbol{x}\, \boldsymbol{h_{fg}}}{\boldsymbol{C_l}} \tag{4.30}$$

where x is the mass quality, h_{fg} is the liquid- gas latent heat of vaporization, and C_l is the specific heat at a constant pressure.

Mass quality is the mass fraction of gas (vapor), which is the fraction of the total mass that is vapor. The lever rule, which follows from the Conservation of Mass equation, is used to relate the quality to other thermodynamics mixture properties in the phase diagram. Quality equation is introduced in equation (4.31)

$$\boldsymbol{x} = \frac{\boldsymbol{m_g}}{\boldsymbol{m}} \tag{4.31}$$

Where m_g the gas mass and *m* is the total mass of gas and liquid.

As shown previously the different shapes of spinodal that were calculated using the Peng Robinson equation affected the quality on the spinodal. Figure 4.7 shows the quality is increasing as the reduced pressure increasing for R134a. Cavitation is not initiated until we get to the spinodal, and quality is based on a specific pressure on the spinodal point. From Equation (4.30) this would suggest that cavitating fluids near the critical point would develop larger quality, and therefore potentially larger temperature drop. However, since the heat of vaporization also reduces as the critical point is approached, the effect will eventually be reduced close to the critical point. This suggests that there is an "optimum" or maximum condition that would yield the largest possible temperature change. All three fluids showed nearly universal variations of quality versus reduced pressure. Table 6 shows the values of maximum quality at the spinodal and reduced pressure for all three fluids, illustrating that for the quality corresponding to locations along the spinodal line is nearly a universal function of reduced pressure.

Quality	Reduced Pressure		
	Water	R134a	R123a
2.5%	0.28	0.30	0.28
5%	0.551	0.55	0.52
10%	0.80	0.78	0.80
20%	0.92	0.97	0.96

Table 6 Approximately Universal variation of Quality with reduced pressure

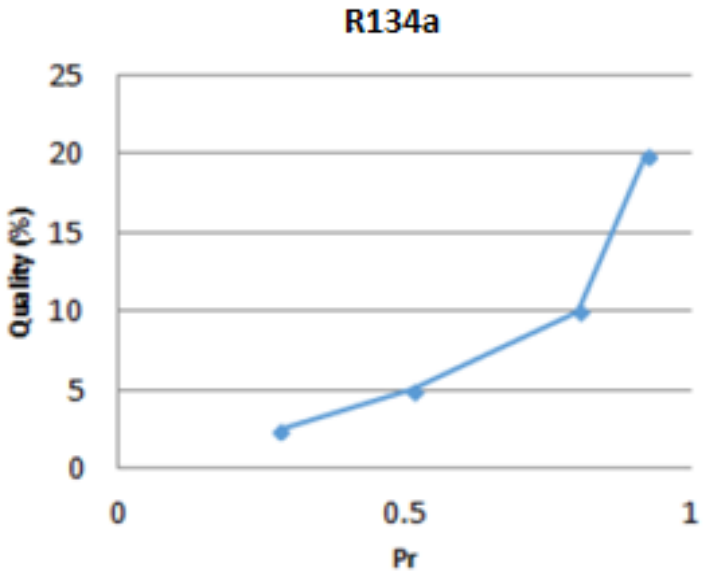

Figure 4.7 R134a results of quality versus reduced pressure

Equation (4.30) of the temperature drop was calculated in terms of reduced pressure. The behavior of the latent heat of vaporization, the heat capacity of liquid, and the quality were also studied as functions of reduced pressure. Quality was solved at the location of the spinodal point, it's an approximation and not in an equilibrium point. Figure 4.8 shows the curve of temperature drop as a function of reduced pressure for R134a, revealing the apparent optimum (or maximum) temperature drop suggested above. As seen in the figure, the maximum possible temperature drop was when the reduced pressure equals approximately 0.5.

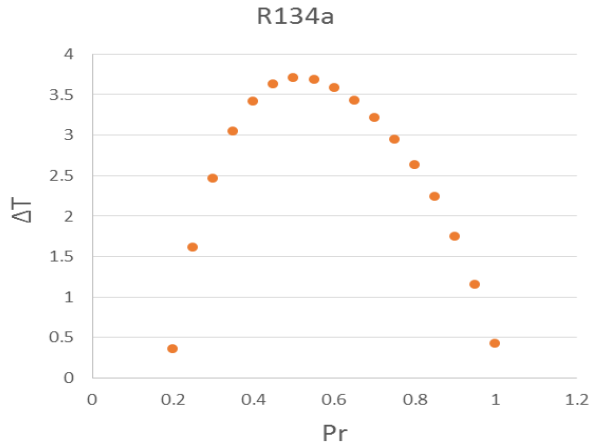

Figure 4.8 R134a temperature drop versus reduced pressure, static evaluations

Heat flow rate is an important application for temperature drop. In Equation (4.30) the assumption was that all heat leaves the flowing fluid, and absorbed heat out of the environment. The total heat flow always equals the sum of the heat flow from the liquid and the heat flow from the environment. An equation of the heat from the environment as a function of temperature drop was developed. Appendix D shows more details of the equation.

$$\dot{q}_{env} = \rho \varphi_v \left[x\, h_{fg} - C_l \Delta T \right] \tag{4.32}$$

where φ_v is the volumetric flow rate of the liquid. Figure 4.9 shows the rate of the heat removal from the environment as function of temperature drop for water with different quality. It's observed that temperature drop increment decreases when there is more heat removed from the environment.

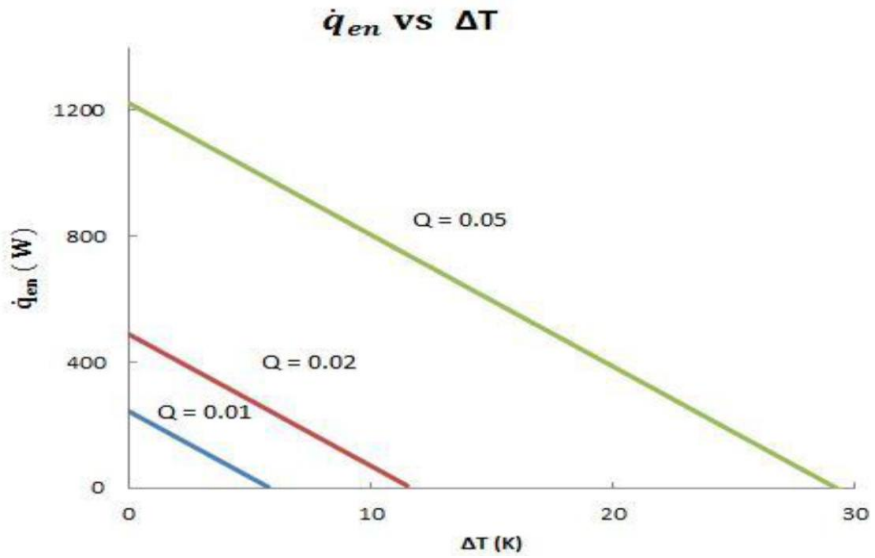

Figure 4.9 Rate of heat from environment versus temperature drop for different qualities

4.3.1 Dynamic Calculation

In the static evaluations, kinetic energy effects were ignored in the temperature drop calculations. It was decided that including kinetic energy effects would be helpful to match the temperature drop values that were measured experimentally. Dynamic evaluation will include calculation of the temperature drop with the fluid flowing with a known velocity, which includes

the kinetic energy entering the nucleation zone. Conservation of mass discusses that gas phase accelerates when it starts nucleating to keep the mass flow rate constant. Using equation (4.7) we get

$$\boldsymbol{V_g = V_l\left(\frac{\rho_l}{\rho_g}\right)} \tag{4.33}$$

where V_g and V_l are gas and liquid velocities. Using the conservation of energy equation, ignoring potential energy and gravitational effect, an equation for the kinetic energy is developed. Equation (4.34) introduces the energy equation for gas phase acceleration. Also, using energy balance and heat transfer equation we get an energy equation in terms of liquid's thermal energy, shown in equation (4.35)

$$\boldsymbol{\Delta E = \frac{1}{2} m_g V_g^2} \tag{4.34}$$

$$\boldsymbol{\Delta E = m_l C_l \Delta T} \tag{4.35}$$

where $\boldsymbol{m_l}$ is the liquid mass flow rate and $\boldsymbol{C_l}$ is the specific heat. Finally, an equation developed for the temperature drop using kinetic energy and under the assumption that all energy coming out of the liquid's thermal energy with no energy removed from the environment. Equation is shown below. Temperature drop is proportional to the quality the same as the static evaluations.

$$\boldsymbol{\Delta T = \frac{x\, V_l^2\left(\frac{\rho_l}{\rho_g}\right)^2}{2C_l}} \tag{4.36}$$

Figure 4.10 shows results for R134a using equation (4.36) in a plot of temperature drop versus reduced pressure. Throat velocity was assumed to be 30 m/s, and quality was calculated using an equation fit in terms of reduced pressure, which was used in the static evaluation. Densities and heat capacity are saturated properties.

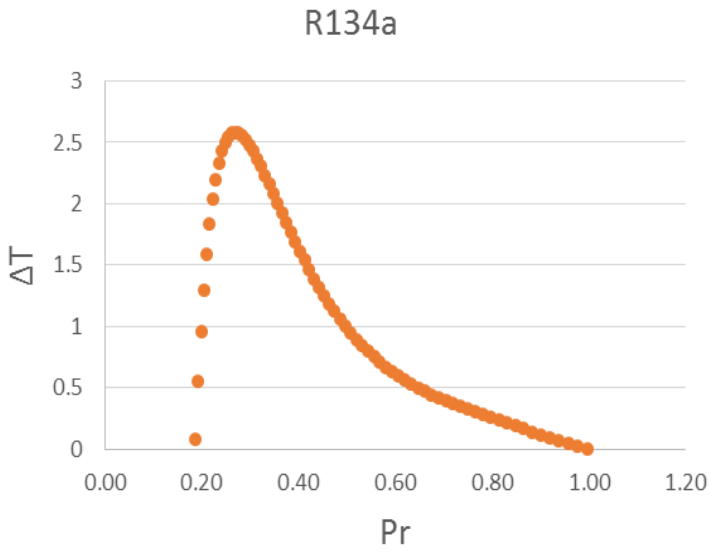

Figure 4.10 R134a temperature drop versus reduced pressure, dynamic evolutions

As seen previously in the static evaluations, the max ΔT value was at a reduced pressure of 0.5. Figure 4.10 shows the max of ΔT occurs at a reduced pressure of 0.3 with kinetic energy effects takes place.

Chapter 5 - Conclusion

The main objective of the project was to investigate a water based non-vapor compression cooling system. In this thesis, the focus was first on visualizing cavitation for water flowing through a converging diverging glass nozzles. These nozzles had throat diameters between 2 mm and 4 mm. Two systems have been used: (1) a continuous flow system, where water was driven by a centrifugal pump, and (2) a transient blow down system, where water flow was initiated using a suction pump. A high-speed camera was used to record videos and images of the associated cavitation phenomena. A thermal infrared camera was used in an attempt to measure temperature drop in the nozzle while the system is running. A piezoelectric disk was used in an attempt to develop more homogenous nucleation in the interior of the converging diverging nozzles, rather than at the inner walls.

Cavitation is an important phenomenon in fluids, and is common occurring in many devices such as pumps, refrigeration expansion valves, and capillary tubes. It occurs when the static pressure of the fluid falls below the vapor pressure, into a metastable liquid state. Cavitation can be in the form of traveling bubble cavitation, vortex cavitation, cloud cavitation, or attached wall cavitation.

At first, two nozzles were tested using the continuous flow system: the expansion nozzle, which has a large expansion angle, and the ogive nozzle, which has an ogive expansion with a very sudden expansion at the throat. Attached wall cavitation occurred with separated flow filled with vapor at the beginning, then it changes to cloud cavitation, appearing as a cloud of vapor, in the middle of the nozzle surrounded by liquid water flowing near the walls. Cavitation was also observed to suddenly collapse. Results were the same for both nozzles.

The transient blow down system was also used to test converging-diverging nozzles. Testing nozzle 2, shown in Table 1, showed the presence of traveling bubble cavitation caused by vapor and gas bubbles in the liquid. Also, attached wall cavitation was observed first near, the throat, then started to collapse, due to the presence of traveling bubble cavitation. Nozzle 5 in Table 1 was tested next. Vortex cavitation developed an orifice jet in the nozzle, where the pressure in the core was smaller than any point in the flow. Vortex cavitation was surrounded by a vapor cloud. The vapor cloud would then begin to collapse, causing the liquid to develop back in the nozzle. The expansion and ogive nozzles were tested as well and showed similar flow

characteristics, except that attached wall cavitation was seen to occur only on one side of the nozzle. The expansion and ogive nozzles were tested at mass flow rates of 0.03 kg/s and 0.02 kg/s respectively. The last nozzle that was tested using the transient blow down system had a 4 mm throat intended to improve the development of homogenous cavitation. The nozzle was tested at a mass flow rate of 0.15 kg/s. Unfortunately, it also showed attached wall cavitation with a turbulent mix of vapor and gas in the liquid flown in the gas.

The thermal infrared camera was also used in the transient blow down system to investigate the possibility of temperature change associated with the water flowing in the system. Two nozzles were used: the ogive nozzle, and the 4 mm nozzle. No significant (measurable) temperature drop was observed while water was flowing in the system.

A piezoelectric disk was used to generate ultrasonic sound waves as an alternative method of creating homogenous nucleation in the interior of nozzle, instead of wall cavitation. The disk was successful in creating nucleation, inside a beaker and inside a test tube. However, it was difficult to implement the disk on the current nozzle flow system, due to the complex curvature of the nozzle geometry, so the work associated with the disk cavitation was discontinued.

A theoretical investigation was undertaken in an attempt to understand the thermodynamics behind the nozzle cavitation phenomena, in an effort to explain the experimental results; specially, why water behaved so poorly. The three conservation equations were developed and discussed during this process. Two equations of state were used in this research, the Peng Robinson equation, and the van der Waals equation. Van der Waals equation was used initially to define saturated liquid and saturated vapor lines, for water, R134a, and R123a. The research later focused on the Peng Robinson equation, which better represent the properties of a wide variety of substances. Coexistence curves and spinodal curves were determined for these equation of state using a Mathcad code. Spinodal curves were shifted to better match the critical point on the coexistence curve. All fluids were observed to have the same basic shapes when expressed in terms of reduced state variables.

Two different types of analysis of temperature drop due to cavitation were developed for comparison with experimental measurements; a static analysis, and a dynamic analysis. In the static analysis, an equation, based on the conservation of mass and energy equations, and ignoring the kinetic energy effects, was developed. The analysis provided a theoretical

prediction for the maximum temperature drop, due to cavitation initiation, as a function of mass quality, liquid-gas latent heat of vaporization, and heat capacity of the liquid. Results shows with an increase in quality, there is an increase in the reduced pressure of the fluid. The maximum possible temperature drop was shown to correspond to an optimum reduced pressure of 0.5, a universal value for all fluids. It was also observed that temperature drop decreases with an increase of the heat removed from the environment. Then, a dynamic analysis was introduced to investigate the possible magnitude of the kinetic energy contribution. The resulting equation for temperature drop due to cavitation was shown to depend on the velocity, latent heat, mass quality, and heat capacity. For an assumed throat velocity of 30 m/s, it was shown that the maximum temperature drop occurs when the reduced pressure equals 0.3, again for a general fluid.

References

[1] Charamko, Serguei, Kristian Debus, and Tom Gielda. "Cooling system utilizing a reciprocating piston." U.S. Patent Application 13/087,062

[2] Brennen, Christopher E. Cavitation and bubble dynamics. Cambridge University Press, 2013.

[3] Davis, Michael P. Experimental investigation of the cavitation of aviation fuel in a converging-diverging nozzle. ProQuest, 2008.

[4] Nakagawa, Masafumi, Menandro Serrano, and Atsushi Harada. "Shock waves in supersonic two-phase flow of CO2 in converging-diverging nozzles." (2008).

[5] Schneider, Brandon, et al. "Cavitation enhanced heat transfer in microchannels." Journal of Heat Transfer 128.12 (2006): 1293-1301

[6] Wang, Yi-Chun, and Christopher E. Brennen. "One-dimensional bubbly cavitating flows through a converging-diverging nozzle." Journal of fluids engineering 120.1 (1998): 166-170.

[7] Wilms, Jeffrey. Flow Visualization of Cavitation. MS Thesis. Kansas State University, Manhattan, 2013.

[8] Lemmon, E.W., Huber, M.L., McLinden, M.O. NIST Standard Reference Database 23: Reference Fluid Thermodynamic and Transport Properties-REFPROP, Version 9.1, National Institute of Standards and Technology, Standard Reference Data Program, Gaithersburg, 2013

Appendix A - Camera Specifications

High Speed Camera Specifications

The Photron FASTCAM SA-5 provides 7,500 frames per second (fps) at a resolution of 1,024 by 1,000 pixels. It could have a maximum of 775,000 fps but it reduces the resolution to 128 by 24 pixels. It has an equivalent light sensitivity 10,000 (monochrome) and 4,000 (color). The camera could have an 8GB, 16GB, 32GB or 64GB memory options. It is provided with a remote control keypad.

Specifications: Partial Frame Rate / Recording Duration Table

FRAME RATE (fps)	MAXIMUM RESOLUTION		MAXIMUM SHUTTER SPEED	RECORD DURATION (12-BIT)							
				TIME (Sec.)				FRAMES			
	Horizontal	Vertical		8GB	16GB	32GB	64GB	8GB	16GB	32GB	64GB
1,000	1,024	1,024	1 µs 1/1,000,000 sec	5.46	10.92	21.84	43.68	5,457	10,918	21,841	43,686
2,000	1,024	1,024		2.73	5.46	10.92	21.84	5,457	10,918	21,841	43,686
4,000	1,024	1,024		1.36	2.73	5.46	10.92	5,457	10,918	21,841	43,686
5,000	1,024	1,024		1.09	2.18	4.37	8.73	5,457	10,918	21,841	43,686
7,000	1,024	1,024		0.78	1.56	3.12	6.24	5,457	10,918	21,841	43,686
7,500	1,024	1,000		0.75	1.49	2.98	5.96	5,588	11,180	22,365	44,735
9,300	1,024	800		0.75	1.50	3.01	6.01	6,985	13,975	27,956	55,918
10,000	1,024	744		0.75	1.50	3.01	6.01	7,511	15,027	30,061	60,127
15,000	960	528		0.75	1.51	3.01	6.02	11,289	22,587	45,182	90,374
20,000	832	448		0.77	1.54	3.07	6.14	15,352	30,716	61,443	122,898
30,000	768	320		0.78	1.55	3.11	6.21	23,284	46,586	93,189	186,396
50,000	512	272		0.82	1.64	3.29	6.57	41,090	82,211	164,452	328,934
75,000	320	264		0.90	1.81	3.61	7.22	67,737	135,523	271,097	542,244
100,000	320	192		0.93	1.86	3.73	7.45	93,138	186,345	372,758	745,585
150,000	256	144		1.03	2.07	4.14	8.28	155,230	310,575	621,264	1,242,642
300,000	256	64		1.16	2.33	4.66	9.31	349,269	698,794	1,397,845	2,795,946
420,000	128	64		1.66	3.33	6.66	13.31	698,538	1,397,589	2,795,690	5,591,893
525,000	128	48		1.77	3.55	7.10	14.20	931,384	1,863,452	3,727,587	7,455,857
775,000	128	24		2.40	4.81	9.62	19.24	1,862,769	3,726,904	7,455,175	14,911,715
930,000	128	16	369 ns 1/2,712,000 sec	3.00	6.01	12.02	24.05	2,794,154	5,590,357	11,182,762	22,367,573
1,000,000	64	16		5.59	11.18	22.37	44.73	5,588,309	11,180,714	22,365,525	44,735,146

OPTION SUBJECT TO EXPORT LICENSE CONTROL RESTRICTIONS WHERE APPLICABLE

Sensor	12-bit ADC (Bayer system color, single sensor) with 20μm pixel
Shutter	Global electronic shutter from 16.7ms to 1μs independent of frame rate
Lens Mount	Interchangeable F-mount and C-mount using supplied adapters
Extended Dynamic Range	Selectable in twenty steps (0 to 95% in 5% increments) to prevent pixel over-exposure
Memory	8GB (standard: 5,457 frames @ maximum resolution) 16GB (option: 10,913 frames @ maximum resolution) 32GB (option: 21,841 frames @ maximum resolution) 64GB (option: 43,686 frames @ maximum resolution)
Video Output 1	NTSC/PAL composite VBS (BNC). Ability to zoom, pan and tilt within image via keypad. Live video during recording
Video Output 2	HD-SDI: HD-SDI 2 channel (BNC) digital output
Camera Control	Through optional keypad with integrated viewfinder and Gigabit Ethernet or RS-422
User Preset Switches	Four user selectable camera function controls mounted on the camera's rear panel
Low Light Mode	Low light mode drops the frame rate and shutter time to their maximum values, while maintaining other set parameters, to enable users to position and focus the camera
Triggering	Selectable positive or negative TTL 5Vp-p or switch closure
Trigger Delay	Programmable delay on selected input and output triggers, 100ns resolution
Timing	Internal clock or external source
Phase Lock	Enables cameras to be synchronized precisely together to a master camera or external source, such as IRIG/GPS time codes
Event Markers	Ten user entered event markers mark specific events within the image sequence in real time. Immediately accessible through software
Dual Speed Recording	Enables the recording speed to be changed up or down by a factor of 2, 4 or 8 during a recording
Trigger Modes	Start, End, Center, Manual, Random, Random Reset, Random Center, Random Manual and Duals Speed Recording
Saved Image Formats	JPEG, AVI, TIFF, BMP, RAW, PNG, MOV and FTIF. Images can be saved with or without image or comment data
Data Display	Frame Rate, Shutter Speed, Trigger Mode, Date or Time, Status (Playback/Record), Real Time, Frame Count and Resolution
Partitioning	Up to 64 memory segments for multiple recording in memory
Data Acquisition	Supports Photron MCDL and DAQ
Cooling	Actively cooled
Operating Temperature	0 - 40 degrees C (32 - 104 degree F)
Mounting	1 x 1/4 - 20 UNC, 1 x 3/8 - 16 UNC, 6 x M6
Dimensions	165mm (6.50")H×153mm (6.02")W×242.5mm (9.55")D *excluding protrusions
Weight	6.2 kg (13.67 lbs)
Power Requirements	100V-240V AC ~ 1.5A, 50-60Hz DC operation 18-36 V DC, 100VA

Thermal Infrared Camera Specifications

The specifications for the FLIR S65 Thermal Infrared Camera are introduced. It has a thermal sensitivity with a 76,000 pixel display which provides high resolution thermal images in real time. It has built-in 4-inch LCD screen that displays the digital images captured by the IR system. It has flexible image storage; images can be stored as JPEG format or in an internal flash RAM. The camera can record up to 30 seconds of voice comment with each image. The camera automatically find the temperature and location of the hot spots in the thermal images, a sound alarm goes off when temperature exceeds the temperature limit set by the user.

Imaging Performance	
Thermal	
Field of view/min focus distance	24° x 18° / 0.3 m
Spatial resolution (IFOV)	1.3 mrad
Electronic zoom function	2, 4, 8, interpolating
Focus	Automatic or manual
Digital image enhancement	Normal and enhanced
Detector type	Focal plane array (FPA) uncooled microbolometer; 320 x 240 pixels
Spectral range	7.5 to 13 µm
Thermal sensitivity @ 50/60Hz	0.08° C at 30° C
Visual	
Built-in digital video	640 x 480 pixels, full color
Image Presentation	
Viewfinder	Built-in high-resolution color LCD (TFT)
Video output	4" LCD with integrated remote control RS 170 EIA/NTSC or CCIR/PAL
External display	Built-in high-resolution color LCD (TFT)
Measurement	
Temperature ranges	-40° C to +120° C (-40° F to +248° F), Range 1 0° C to +500° C (+32° F to +932° F), Range 2 +350° C to +1500° C (+662° F to +2732° F), Range 3 Up to +2000° C (+3632° F), optional
Accuracy (% of reading)	± 2° C or ± 2%
Measurement modes	Up to 10 movable spots. Automatic temperature difference (Δ) and placement and reading of maximum and minimum temperatures. Up to 5 movable circle areas or boxes. Up to 2 isotherms. Line profile.
Emissivity corrections	Variable from 0.1 to 1.0 or select from listings in pre-defined material list
Measurement features	Automatic corrections based on user input for reflected ambient temperature, distance, relative humidity, atmospheric transmission, and external optics
Optics transmission correction	Automatic, based on signals from internal sensors
Image Storage	
Type	Removable CompactFlash (256 MB) memory card; built-in Flash memory (100 images); built-in RAM memory for burst and AVI recording
File format - THERMAL	Standard JPEG; 14 bit thermal measurement data included
File format - VISUAL	Standard JPEG inked with corresponding thermal image
Voice annotation of images	Input via supplied Bluetooth® wireless headset up to 30 seconds of digital voice clip per image stored with image
Text annotation of images	Predefined by user and stored with image
System Status Indicator	
LCD display	Shows status of battery and storage media. Indication of power, communication and storage modes.

Power Source	
Battery type	Li-Ion, rechargeable, field-replaceable
Battery operating time	2 hours continuous operation
Charging system	In camera (AC adapter or 12V from car) or 2 bay intelligent charger
External power operation	AC adapter 110/220 VAC, 50/60Hz or 12V from car (cable with standard plug optional)
Power saving	Automatic shutdown and sleep mode (user-selectable)
Environmental	
Operating temperature range	-15° C to +50° C (5° F to 122° F)
Storage temperature range	-40° C to +70° C (-40° F to 158° F)
Humidity	Operating and storage 10% to 95%, non-condensing
Encapsulation	IP 54 IEC 529
Shock	Operational: 25G, IEC 68-2-29
Vibration	Operational: 2G, IEC 68-2-6
Physical Characteristics	
Weight	2.0 kg (4.4 lbs) w/battery and top handle (includes remote control, LCD, video camera and laser) 1.4 kg (3.1lbs) excluding battery and handle
Size	100mm x 120mm x 220 mm (3.9" x 4.7" x 8.7") camera only
Tripod mounting	1/4" - 20

ThermaCAM S65 System Includes:
IR camera with visual camera, Laser LocatIR, remote with LCD display
High-output multi-LED target light
Bluetooth® wireless headset
Carrying case, lens cap, shoulder strap, hand strap
User manual (multilingual)
Batteries (2)
Power supply
Battery charger
FireWire® (IEEE 1394) cable
Video cable with RCA plug
USB cable
S-video cable
256 MB CompactFlash card
ThermaCAM QuickViewTM software

Lenses (optional)	
Field of view/ minimum focus distance	3X Telescope (7° x 5.3°/4m) 2X Telescope (12° X 9°/1.2m) 0.5X Wide angle (45° x 34°/0.1m) 0.3X Wide angle (80° x 60°/0.1m) 200 µm Close-up (64mm x 48mm/150mm) 100 µm Close-up (34mm x 25mm/80mm) 50 µm Close-up (15mm x 11mm/19mm) Wearable Optics/Heads-up Display
Interfaces	
Firewire output (IEEE 1394)	Real-time digital transfer of radiometric thermal images or digital video (DV) out
USB / RS232	Image (thermal and visual), measurement data, voice and text transfer to PC
IrDA	Two-way data transfer from laptop, PDA
Remote control	Removable handle with redundant controls and LCD

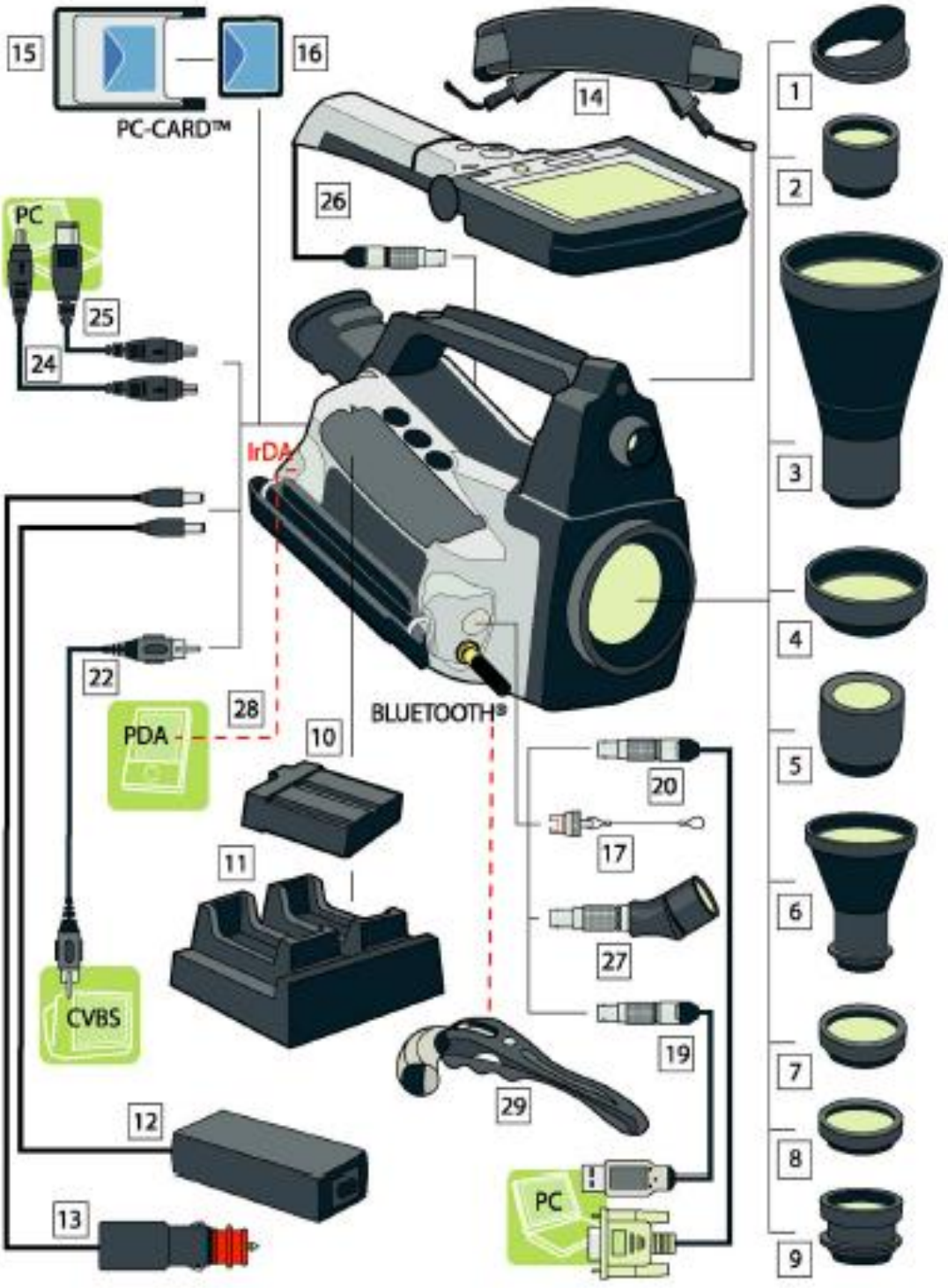
15
16
PC-CARD™
14
1
2
26
PC
25
24
3
IrDA
4
22
28
PDA
10
BLUETOOTH®
20
5
17
11
6
27
CVBS
19
29
7
12
8
PC
13
9

Callout	Part No.	Description of part
1	194 560	Protective plastic window
2	1 194 977	Protective window
3	194 579	124 mm IR lens
4	194 176	72 mm IR lens
5	194 401	18 mm IR lens
6	194 702	9.0 mm IR lens
7	194 533	64/150 close-up IR lens
8	1 194 978	34/80 close-up IR lens
9	1 700 500	50 µm IR lens
10	1 195 268	Battery
11	1 195 267	2-bay battery charger
12	1 909 528	External power supply
13	1 195 143	Automotive (cigarette lighter) 12 VDC adapter
14	117 132	Shoulder strap
15	1 909 820	Adapter for CompactFlash™ card
16	1 909 653	CompactFlash™ card
17	1 910 233	▪ Protective cap for RS-232/USB connector
19	1 195 314	USB cable
20	1 195 313	RS-232 cable
22	1 909 775	CVBS cable (composite video cable)
24	1 909 812	FireWire cable 4/4
25	1 909 813	FireWire cable 4/6
26	1 195 346	Remote control
27	1 195 994	Video lamp
28		IrDA infrared communication link
29	One of the following part numbers: ▪ 1 910 218 ▪ 1 910 219 ▪ 1 910 213	Headset with Bluetooth® wireless technology ➲ Depending on your camera configuration, this feature may be an extra option.

Appendix B - Saturation Tables

Water Saturation Table

Temp	Temp	Pressure	volume (m^3/kg)		volume (m^3/mol)		volume Ratio		density Ratio		Pr	Tr
°C	K	Pa	vf	vg	vf	vg	Vf/Vc	Vg/Vc	ρf/ρc	ρg/ρc	P/Pc	T/Tc
150	423.15	4.76E+05	0.0010905	0.3928	1.97E-05	7.08E-03	0.351	126.397	2.850	0.008	0.02	0.653715
160	433.15	6.18E+05	0.001102	0.3071	1.99E-05	5.53E-03	0.355	98.820	2.820	0.010	0.03	0.669164
170	443.15	7.92E+05	0.0011143	0.2428	2.01E-05	4.38E-03	0.359	78.130	2.789	0.013	0.04	0.684613
180	453.15	1.00E+06	0.0011274	0.1941	2.03E-05	3.50E-03	0.363	62.459	2.756	0.016	0.05	0.700062
190	463.15	1.25E+06	0.0011415	0.1565	2.06E-05	2.82E-03	0.367	50.359	2.722	0.020	0.06	0.715511
200	473.15	1.55E+06	0.0011565	0.1274	2.08E-05	2.30E-03	0.372	40.996	2.687	0.024	0.07	0.730959
210	483.15	1.91E+06	0.0011726	0.1044	2.11E-05	1.88E-03	0.377	33.594	2.650	0.030	0.09	0.746408
220	493.15	2.32E+06	0.00119	0.08619	2.14E-05	1.55E-03	0.383	27.735	2.611	0.036	0.10	0.761857
230	503.15	2.80E+06	0.0012088	0.07158	2.18E-05	1.29E-03	0.389	23.033	2.571	0.043	0.13	0.777306
240	513.15	3.34E+06	0.0012291	0.05976	2.21E-05	1.08E-03	0.396	19.230	2.528	0.052	0.15	0.792755
250	523.15	3.97E+06	0.0012512	0.05013	2.25E-05	9.03E-04	0.403	16.131	2.484	0.062	0.18	0.808203
260	533.15	4.69E+06	0.0012755	0.04221	2.30E-05	7.61E-04	0.410	13.583	2.436	0.074	0.21	0.823652
270	543.15	5.50E+06	0.0013023	0.03564	2.35E-05	6.42E-04	0.419	11.468	2.386	0.087	0.25	0.839101
280	553.15	6.41E+06	0.0013321	0.03017	2.40E-05	5.44E-04	0.429	9.708	2.333	0.103	0.29	0.85455
290	563.15	7.44E+06	0.0013656	0.02557	2.46E-05	4.61E-04	0.439	8.228	2.276	0.122	0.34	0.869998
300	573.15	8.58E+06	0.0014036	0.02167	2.53E-05	3.90E-04	0.452	6.973	2.214	0.143	0.39	0.885447
310	583.15	9.86E+06	0.001448	0.01834	2.61E-05	3.30E-04	0.466	5.900	2.146	0.169	0.45	0.900896
320	593.15	1.13E+07	0.001499	0.01549	2.70E-05	2.79E-04	0.482	4.984	2.073	0.201	0.51	0.916345
330	603.15	1.29E+07	0.001561	0.01298	2.81E-05	2.34E-04	0.502	4.176	1.991	0.239	0.58	0.931794
340	613.15	1.46E+07	0.001638	0.01080	2.95E-05	1.95E-04	0.527	3.475	1.897	0.288	0.66	0.947242
350	623.15	1.65E+07	0.001740	0.008802	3.14E-05	1.59E-04	0.560	2.832	1.786	0.353	0.75	0.962691
360	633.15	1.87E+07	0.001893	0.006945	3.41E-05	1.25E-04	0.609	2.235	1.642	0.447	0.84	0.97814
370	643.15	2.10E+07	0.002215	0.004954	3.99E-05	8.93E-05	0.713	1.594	1.403	0.627	0.95	0.993589
374.14	647.29	2.21E+07	0.003155	0.003155	5.69E-05	5.69E-05	1.015	1.015	0.985	0.985	1.00	0.999985

- Tables imported from Refprop which is published by NIST, the program uses thermodynamics equations to solve for the saturation properties of a fluid. Tables were then modified by adding volume and density ratios. [8]

R134a Saturation Table

Temp	Temp	Pressure	volume (m^3/kg)		volume (m^3/mol)		volume Ratio		density Ratio		Pr	Tr
°C	K	kPa	vf	vg	vf	vg	Vf/Vc	Vg/Vc	ρf/ρc	ρg/ρc	P/Pc	T/Tr
-40	233.15	51.2	0.0007055	0.3569	7.19822E-05	0.036415	0.358395	181.3056	2.79022	0.005516	0.012719	0.623063
-32	241.15	76.7	0.0007172	0.2451	7.31759E-05	0.025008	0.364338	124.511	2.744702	0.008031	0.018975	0.644441
-22	251.15	121.7	0.0007328	0.159	7.47676E-05	0.016223	0.372263	80.77216	2.686272	0.012381	0.03003	0.671165
-12	261.15	185.2	0.0007498	0.1068	7.65021E-05	0.010897	0.380899	54.25451	2.625367	0.018432	0.045665	0.697889
-2	271.15	272.2	0.0007684	0.0744	7.83999E-05	0.007591	0.390348	37.79528	2.561817	0.026458	0.067044	0.724613
12	285.15	443	0.0007971	0.046	8.13281E-05	0.004693	0.404928	23.36805	2.469577	0.042793	0.109099	0.762026
24	297.15	645.8	0.0008257	0.0317	8.42462E-05	0.003234	0.419456	16.10363	2.384038	0.062098	0.15903	0.794094
34	307.15	862.6	0.000853	0.0236	8.70316E-05	0.002408	0.433325	11.98882	2.307737	0.083411	0.212431	0.820818
40	313.15	1016.6	0.0008714	0.0199	8.89089E-05	0.00203	0.442672	10.10922	2.259008	0.09892	0.250345	0.836852
48	321.15	1252.9	0.0008989	0.0159	9.17148E-05	0.001622	0.456642	8.077216	2.189899	0.123805	0.308522	0.858231
52	325.15	1385.4	0.0009142	0.0142	9.32758E-05	0.001449	0.464415	7.213614	2.153249	0.138627	0.341158	0.86892
60	333.15	1681.8	0.0009488	0.0114	9.68061E-05	0.001163	0.481991	5.791212	2.074726	0.172675	0.414113	0.890299
70	343.15	2116.8	0.0010027	0.0086	0.000102305	0.000877	0.509373	4.368809	1.963199	0.228895	0.521232	0.917023
80	353.15	2633.2	0.0010766	0.0064	0.000109845	0.000653	0.546914	3.251207	1.828441	0.307578	0.648374	0.943747
90	363.15	3244.2	0.0011949	0.0046	0.000121916	0.000469	0.60701	2.336805	1.647418	0.427935	0.798892	0.97047
100	373.15	3974.2	0.0015443	0.0027	0.000157565	0.000275	0.784506	1.371603	1.274688	0.729074	0.978867	0.997194
101.06	374.21	4059.1	0.0019535	0.002	0.000199316	0.000204	0.99238	1.016002	1.007679	0.98425	0.999778	1.000027

- Tables imported from Refprop which is published by NIST, the program uses thermodynamics equations to solve for the saturation properties of a fluid. Tables were then modified by adding volume and density ratios. [8]

R123a Saturation Table

Temp	Temp	Pressure	volume (m^3/kg)		volume (m^3/mol)		volume Ratio		density Ratio		Pr	Tr
°C	K	Pa	vf	vg	vf	vg	Vf/Vc	Vg/Vc	ρf/ρc	ρg/ρc	P/Pc	T/Tc
7	280.15	44233	0.000663	0.335864	0.000101318	0.051364	0.3677	186.4032	2.720	0.00536	0.01207	0.612879
17	290.15	66848	0.000674	0.228258	0.000103018	0.034908	0.3739	126.6827	2.675	0.00789	0.01823	0.634768
27	300.15	97798	0.000685	0.159757	0.000104811	0.024432	0.3804	88.6647	2.629	0.01128	0.02668	0.656656
37	310.15	139020	0.000698	0.114718	0.000106713	0.017544	0.3873	63.6683	2.582	0.01571	0.03792	0.678545
47	320.15	192640	0.000711	0.084232	0.000108739	0.012882	0.3946	46.7484	2.534	0.02139	0.05255	0.700433
57	330.15	260950	0.000725	0.063056	0.000110915	0.009643	0.4025	34.9957	2.484	0.02857	0.07118	0.722322
67	340.15	346360	0.000741	0.048001	0.000113248	0.007341	0.4110	26.6403	2.433	0.03754	0.09448	0.74421
77	350.15	451470	0.000757	0.037069	0.000115786	0.005669	0.4202	20.5730	2.380	0.04861	0.12315	0.766099
87	360.15	578980	0.000775	0.028977	0.00011856	0.004431	0.4303	16.0822	2.324	0.06218	0.15793	0.787988
97	370.15	731720	0.000795	0.022881	0.000121614	0.003499	0.4413	12.6990	2.266	0.07875	0.19960	0.809876
107	380.15	912680	0.000818	0.018214	0.000125025	0.002786	0.4537	10.1089	2.204	0.09892	0.24896	0.831765
117	390.15	1125000	0.000843	0.014585	0.000128892	0.002231	0.4678	8.0947	2.138	0.12354	0.30687	0.853653
127	400.15	1372200	0.000872	0.01172	0.000133354	0.001792	0.4840	6.5048	2.066	0.15373	0.37430	0.875542
137	410.15	1657700	0.000907	0.009424	0.000138637	0.001441	0.5031	5.2304	1.988	0.19119	0.45218	0.89743
147	420.15	1985800	0.000949	0.007551	0.000145109	0.001155	0.5266	4.1909	1.899	0.23861	0.54168	0.919319
157	430.15	2361200	0.001004	0.005991	0.000153498	0.000916	0.5571	3.3247	1.795	0.30078	0.64408	0.941207
167	440.15	2789800	0.001082	0.004644	0.000165407	0.00071	0.6003	2.5772	1.666	0.38802	0.76099	0.963096
177	450.15	3280600	0.00122	0.003374	0.000186609	0.000516	0.6772	1.8725	1.477	0.53404	0.89487	0.984984
182	455.15	3554700	0.001393	0.002597	0.000213054	0.000397	0.7732	1.4414	1.293	0.69377	0.96964	0.995929
183	456.15	3627000	0.0015	0.0022	0.000229395	0.000336	0.8325	1.2210	1.201	0.81901	0.98936	0.998118

- Tables imported from Refprop which is published by NIST, the program uses thermodynamics equations to solve for the saturation properties of a fluid. Tables were then modified by adding volume and density ratios. [8]

Appendix C - Mathcad Codes

R134a Saturation Values Calculations

Mathcad code for saturation values was developed by Dr. Beck and then was modified

Linear Interpolation Algorithm for R134a Saturation Properties

ORIGIN := 1 TOL := 0.0000001 kJ := 1000·J

Input Matrix of R134a Saturation Properties, T(C), p(MPa), ρ_f(kg/m^3), ρ_g(kg/m^3), h_f(kJ/kgK), h_g(kJ/kgK), s_f(kJ/kgK), s_g(kJ/kgK), C_{pf}(kJ/kgK), C_{pg}(kJ/kgK):

RP1 :=

	T(C)	p(MPa)	ρ_f(kg/m^3)	$\rho_g$kg/m^3)	h_f(kJ/kg)
	1	2	3	4	5
1	0	0.293	$1.295 \cdot 10^3$	14.428	200
2	1	0.304	$1.292 \cdot 10^3$	14.939	201.34
3	2	0.315	$1.288 \cdot 10^3$	15.465	202.69
4	3	0.326	$1.285 \cdot 10^3$	16.005	204.04
5	4	0.338	$1.281 \cdot 10^3$	16.56	205.4
6	5	0.35	$1.278 \cdot 10^3$	17.131	206.75
7	6	0.362	$1.275 \cdot 10^3$	17.717	208.11
8	7	0.375	$1.271 \cdot 10^3$	18.319	209.47

RP2 :=

	h_g(kJ/kg)	s_f(kJ/kgK)	s_g(kJ/kgK)	C_{pf}(kJ/kgK)	C_{pg}(kJ/kgK)
	1	2	3	4	5
1	398.6	1	1.727	1.341	0.897
2	399.19	1.005	1.726	1.344	0.902
3	399.77	1.01	1.726	1.347	0.906
4	400.34	1.015	1.726	1.349	0.911
5	400.92	1.02	1.725	1.352	0.916
6	401.49	1.024	1.724	1.355	0.921
7	402.06	1.029	1.724	1.358	0.925
8	402.63	1.034	1.724	1.361	0.93
9	403.2	1.039	1.723	1.364	0.935

Extract Individual Properties from above Input Matrices, RP1 & RP2:

$\Delta T := 1\,\Delta°C \qquad i := 1..102$

$TT_i := RP1_{i,1}\cdot\Delta°C \qquad PP_i := RP1_{i,2}\cdot MPa \qquad \rho pf_i := RP1_{i,3}\cdot\frac{kg}{m^3} \qquad \rho pg_i := RP1_{i,4}\cdot\frac{kg}{m^3} \qquad HHf_i := RP1_{i,5}\cdot\frac{kJ}{kg}$

$HHg_i := RP2_{i,1}\cdot\frac{kJ}{kg} \qquad SSf_i := RP2_{i,2}\cdot\frac{kJ}{kg\cdot K} \qquad SSg_i := RP2_{i,3}\cdot\frac{kJ}{kg\cdot K} \qquad Cpf_i := RP2_{i,4}\cdot\frac{kJ}{kg\cdot K} \qquad Cpg_i := RP2_{i,5}\cdot\frac{kJ}{kg\cdot K}$

Define Individual Continuous Interpolation Functions for Saturation Properties as a Function of Temperature, T:

(a) Saturation Pressure, p(T):

$$p(T) := \left| \begin{array}{l} T \leftarrow \frac{T}{\Delta°C} \\ j \leftarrow \text{floor}\left(\frac{T}{\frac{\Delta T}{\Delta°C}}\right) + 1 \\ Press \leftarrow PP_j + \left(\frac{PP_{j+1} - PP_j}{\frac{\Delta T}{\Delta°C}}\right)\cdot\left(T - \frac{TT_j}{\Delta°C}\right) \end{array} \right.$$

$p(0\cdot\Delta°C) = 0.293\,MPa$

$T := 0.0\cdot\Delta°C, 0.1\cdot\Delta°C .. 101\cdot\Delta°C$

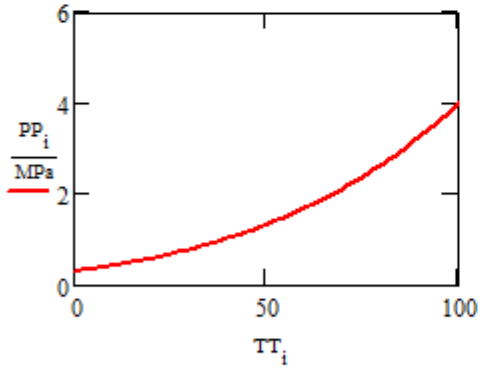

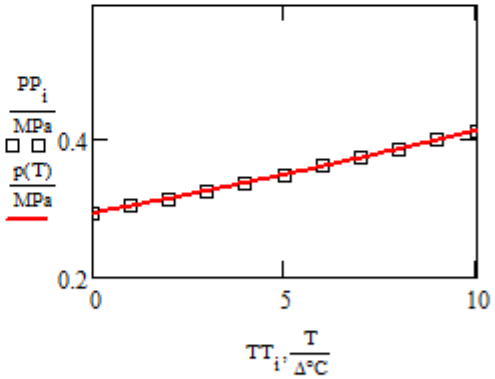

(b) Liquid Density, $\rho_f(T)$:

$$\rho_f(T) := \left| \begin{array}{l} T \leftarrow \frac{T}{\Delta°C} \\ j \leftarrow \text{floor}\left(\frac{T}{\frac{\Delta T}{\Delta°C}}\right) + 1 \\ dens_f \leftarrow \rho pf_j + \left(\frac{\rho pf_{j+1} - \rho pf_j}{\frac{\Delta T}{\Delta°C}}\right)\cdot\left(T - \frac{TT_j}{\Delta°C}\right) \end{array} \right.$$

$\rho_f(0\cdot\Delta°C) = 1294.8\,\frac{kg}{m^3}$

(c) Vapor Density, $\rho_g(T)$:

$$\rho_g(T) := \left| \begin{array}{l} T \leftarrow \frac{T}{\Delta°C} \\ j \leftarrow \text{floor}\left(\frac{T}{\frac{\Delta T}{\Delta°C}}\right) + 1 \\ dens_g \leftarrow \rho\rho g_j + \left(\frac{\rho\rho g_{j+1} - \rho\rho g_j}{\frac{\Delta T}{\Delta°C}}\right) \cdot \left(T - \frac{TT_j}{\Delta°C}\right) \end{array} \right.$$

$$\rho_g(0 \cdot \Delta°C) = 14.428 \frac{kg}{m^3}$$

(d) Liquid Enthalpy $h_f(T)$:

$$h_f(T) := \left| \begin{array}{l} T \leftarrow \frac{T}{\Delta°C} \\ j \leftarrow \text{floor}\left(\frac{T}{\frac{\Delta T}{\Delta°C}}\right) + 1 \\ hliq \leftarrow HHf_j + \left(\frac{HHf_{j+1} - HHf_j}{\frac{\Delta T}{\Delta°C}}\right) \cdot \left(T - \frac{TT_j}{\Delta°C}\right) \end{array} \right.$$

$$h_f(0 \cdot \Delta°C) = 200 \frac{kJ}{kg}$$

(e) Vapor Enthalpy $h_g(T)$:

$$h_g(T) := \left| \begin{array}{l} T \leftarrow \frac{T}{\Delta°C} \\ j \leftarrow \text{floor}\left(\frac{T}{\frac{\Delta T}{\Delta°C}}\right) + 1 \\ hvap \leftarrow HHg_j + \left(\frac{HHg_{j+1} - HHg_j}{\frac{\Delta T}{\Delta°C}}\right) \cdot \left(T - \frac{TT_j}{\Delta°C}\right) \end{array} \right.$$

$$h_g(0 \cdot \Delta°C) = 398.6 \frac{kJ}{kg}$$

(f) Liquid Entropy $s_f(T)$:

$$s_f(T) := \left| \begin{array}{l} T \leftarrow \frac{T}{\Delta°C} \\ j \leftarrow \text{floor}\left(\frac{T}{\frac{\Delta T}{\Delta°C}}\right) + 1 \\ sliq \leftarrow SSf_j + \left(\frac{SSf_{j+1} - SSf_j}{\frac{\Delta T}{\Delta°C}}\right) \cdot \left(T - \frac{TT_j}{\Delta°C}\right) \end{array} \right.$$

$$s_f(0 \cdot \Delta°C) = 1.000 \frac{kJ}{kg \cdot K}$$

(g) Vapor Entropy $s_g(T)$:

$$s_g(T) := \left| \begin{array}{l} T \leftarrow \dfrac{T}{\Delta°C} \\ j \leftarrow \text{floor}\left(\dfrac{T}{\frac{\Delta T}{\Delta°C}}\right) + 1 \\ svap \leftarrow SSg_j + \left(\dfrac{SSg_{j+1} - SSg_j}{\frac{\Delta T}{\Delta°C}}\right) \cdot \left(T - \dfrac{TT_j}{\Delta°C}\right) \end{array} \right.$$

$$s_g(0 \cdot \Delta°C) = 1.727 \frac{kJ}{kg \cdot K}$$

(h) Liquid Specific Heat, $C_{pf}(T)$:

$$C_{pf}(T) := \left| \begin{array}{l} T \leftarrow \dfrac{T}{\Delta°C} \\ j \leftarrow \text{floor}\left(\dfrac{T}{\frac{\Delta T}{\Delta°C}}\right) + 1 \\ Cpliq \leftarrow Cpf_j + \left(\dfrac{Cpf_{j+1} - Cpf_j}{\frac{\Delta T}{\Delta°C}}\right) \cdot \left(T - \dfrac{TT_j}{\Delta°C}\right) \end{array} \right.$$

$$C_{pf}(0 \cdot \Delta°C) = 1.341 \frac{kJ}{kg \cdot K}$$

(i) Vapor Specific Heat, $C_{pg}(T)$:

$$C_{pg}(T) := \left| \begin{array}{l} T \leftarrow \dfrac{T}{\Delta°C} \\ j \leftarrow \text{floor}\left(\dfrac{T}{\frac{\Delta T}{\Delta°C}}\right) + 1 \\ Cpvap \leftarrow Cpg_j + \left(\dfrac{Cpg_{j+1} - Cpg_j}{\frac{\Delta T}{\Delta°C}}\right) \cdot \left(T - \dfrac{TT_j}{\Delta°C}\right) \end{array} \right.$$

$$C_{pg}(0 \cdot \Delta°C) = 0.897 \frac{kJ}{kg \cdot K}$$

(j) Define Vaporization Properties, $h_{fg}(T)$ and $s_{fg}(T)$:

$$h_{fg}(T) := h_g(T) - h_f(T) \qquad h_{fg}(0 \cdot \Delta°C) = 198.6 \frac{kJ}{kg}$$

$$s_{fg}(T) := s_g(T) - s_f(T) \qquad s_{fg}(0 \cdot \Delta°C) = 0.727 \frac{kJ}{kg \cdot K}$$

Van der Waals Equation R134a

Finding Saturation Values

Van der Waals Equation (R134a) (bar) Calculating Saturation Values & Spinodal

$a := 9.79 \qquad b := 0.0944 \qquad R := 0.08206 \qquad T := 300$

Van der Waals Equation $P(V,T) := \left(R\frac{T}{V-b}\right) - \frac{a}{V^2}$

$V := 0.095, 0.096 .. 2 \qquad p := 15.70278901$

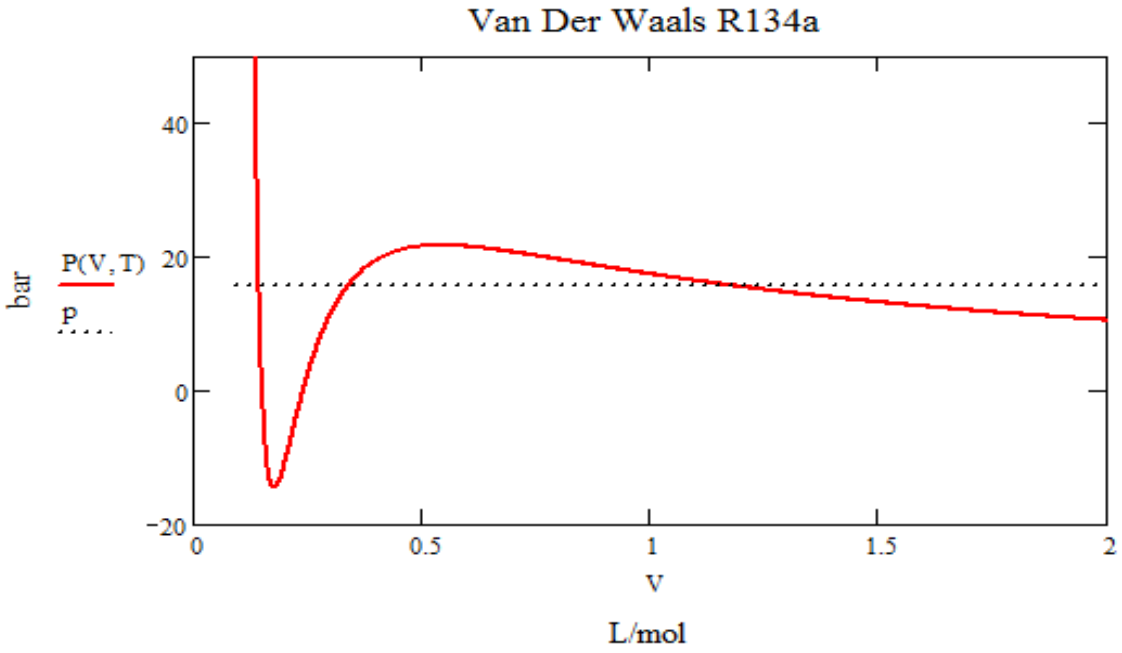

$$\left[\int_{0.1467}^{1.1737} (P(V,T) - p)\, dV\right] = -0$$

$V := 0.1 \qquad y := 1$

Given

$P(V,T) = p$

$P(y,T) = p$

$X := \text{Find}(V,y)$

$$X = \begin{pmatrix} 0.1467 \\ 1.1737 \end{pmatrix}$$

Solve block for determining saturation limits for a given temperature T:

Initial Guesses for Vf and Vg:

$V_f := 0.1 \qquad V_g := 2 \qquad p := 15$

Given

$$\left[\int_{V_f}^{V_g} (P(V,T) - p)\, dV\right] = 0$$

$$P(V_f, T) = p$$

$$P(V_g, T) = p$$

$$X := \text{Find}(V_f, V_g, p)$$

Saturation Value

$$X = \begin{pmatrix} 0.147 \\ 1.174 \\ 15.703 \end{pmatrix}$$

$V := 0.095, 0.096 .. 2$

$V_f := X_0 \qquad V_g := X_1 \qquad p := X_2$

$V_f = 0.147 \qquad V_g = 1.174 \qquad p = 15.703$

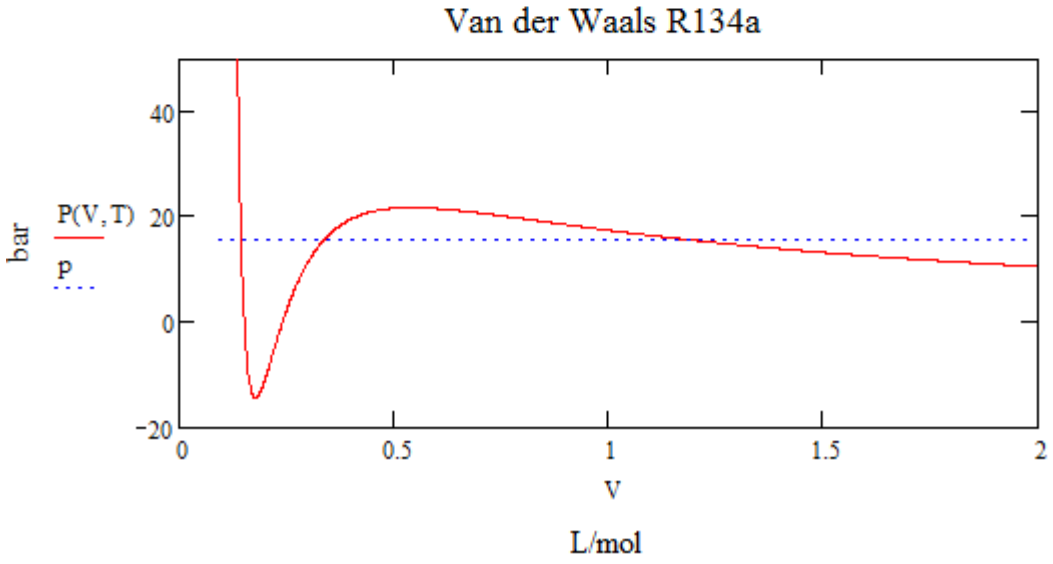

Finding Spinodal Points

Van Der Waals Equation Derivation (R134a), Calculating Spinodal Points

$a1 := 9.79 \qquad b1 := 0.0944 \qquad R1 := 0.08206 \qquad T1 := 300$

Van der Waals Derivation $\qquad P1(V1) := \left[-R1 \cdot \frac{T1}{(V1 - b1)^2} + 2 \cdot \frac{a1}{V1^3} \right]$

$V1 := 0.15, 0.151 .. 2$

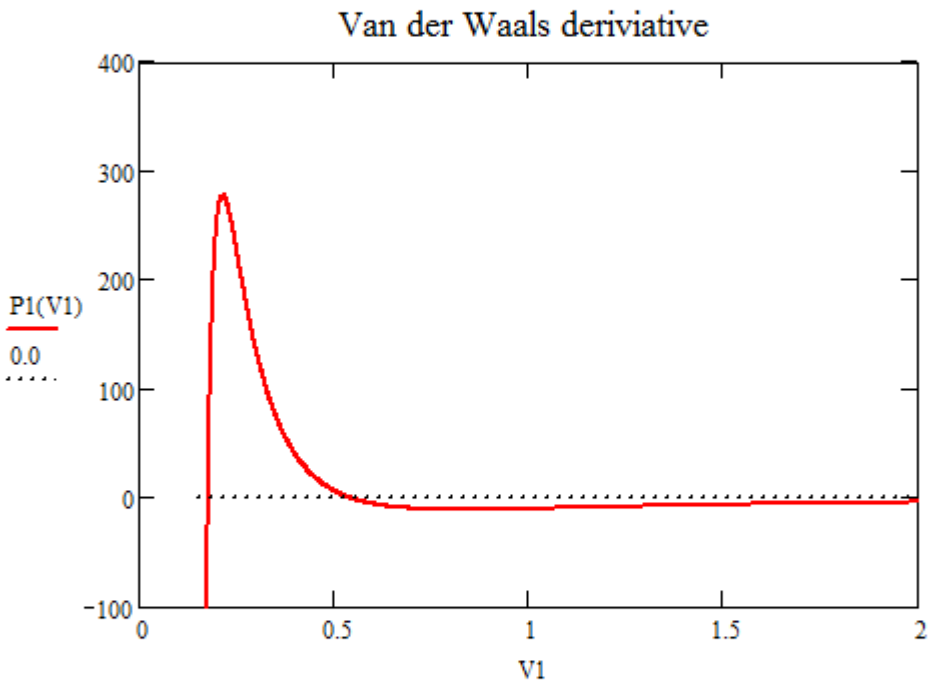

$V1 := 0.2 \qquad y1 := 0.5$

Given

$P1(V1) = 0$

$P1(y1) = 0$

Finding Spinodal Points

$X1 := \text{Find}(V1, y1) \qquad X1 = \begin{pmatrix} 0.18 \\ 0.543 \end{pmatrix}$

Peng Robinson Equation R134a

Finding Saturation Values

Evaluation of Peng Robinson Equation with Units

$kmol := 1000 \cdot mol$ $\quad MPa = 1 \times 10^{6}\,Pa$ $\quad kJ := 1000 \cdot J$ $\quad kmol = 1 \times 10^{3}\,mol$

$R_u := 8.314 \cdot \frac{J}{K \cdot mol}$ $\quad R_{uu} := 8.31434 \cdot \frac{kJ}{kmol \cdot K}$

Critical Temp and Press for R134a:

$T_c := 374.2 \cdot K$ $\quad p_c := 4.059 \cdot MPa$ $\quad \omega := 0.329$

$T_c = 374.2\,K$ $\quad T_c = 101.05\,°C$

Input Parameters for Peng-Robinson EOS:

$v_c := \frac{R_u \cdot T_c}{p_c}$ $\quad v_c = 7.665 \times 10^{-4}\,\frac{m^3}{mol}$

$a_c := 0.45724 \cdot \frac{R_u^{\,2} \cdot T_c^{\,2}}{p_c}$ $\quad a_c = 1.09041\,\frac{kg \cdot m^5}{mol^2 \cdot s^2}$ $\quad \frac{R_u \cdot T_c}{p_c} = 0.766501\,\frac{m^3}{kmol}$

$\kappa(\omega) := 0.37464 + 1.54226 \cdot \omega - 0.26992 \cdot \omega^2$

$\alpha(\omega, T) := \left[1 + \kappa(\omega) \cdot \left[1 - \left(\sqrt{\frac{T}{T_c}}\right)\right]\right]^2$

$a_{aa} := 0.45724 \cdot p_c \cdot \frac{R_u^{\,2} \cdot T_c^{\,2}}{p_c^{\,2}}$

$a(\omega, T) := a_c \cdot \alpha(\omega, T)$

$a_{aa} := 0.45724 \cdot p_c \cdot \left(\frac{R_u \cdot T_c}{p_c}\right)^2$

$b := 0.07780 \cdot \frac{R_u \cdot T_c}{p_c}$ $\quad b = 0.05963\,\frac{m^3}{kmol}$

$T_1 := 30\,°C$ $\quad T_1 = 303.15\,K$

$p(T, v) := \frac{R_u \cdot T}{v - b} - \frac{a(\omega, T)}{v^2 + 2v \cdot b - b^2}$

Check on Calculation--comparing with R134a Phase Diagram:

Sat vap at 30C = 303.15K and v = 0.026 m^3/kg should have a pressure of about 7.9 bar

$v_{test} := 0.026 \cdot \frac{m^3}{kg} \cdot 102.03 \cdot \frac{kg}{kmol}$ $\quad v_{test} = 2652.780\,\frac{cm^3}{mol}$ $\quad \frac{a_c}{v_c^{\,2}} = 1.856 \times 10^{6}\,Pa$

$p(303.15 \cdot K, v_{test}) = 7.973\,bar$ $\quad$ it checks--good!!

$T_1 := 30\,°C$

$v := 60 \cdot \frac{cm^3}{mol}, 60.2 \cdot \frac{cm^3}{mol} .. 900 \cdot \frac{cm^3}{mol}$

$b = 59.634 \frac{cm^3}{mol}$ $\quad b = 0.06 \frac{L}{mol}$

$v := 0.06 \cdot \frac{L}{mol}, 0.062 \cdot \frac{L}{mol} .. 4 \cdot \frac{L}{mol}$

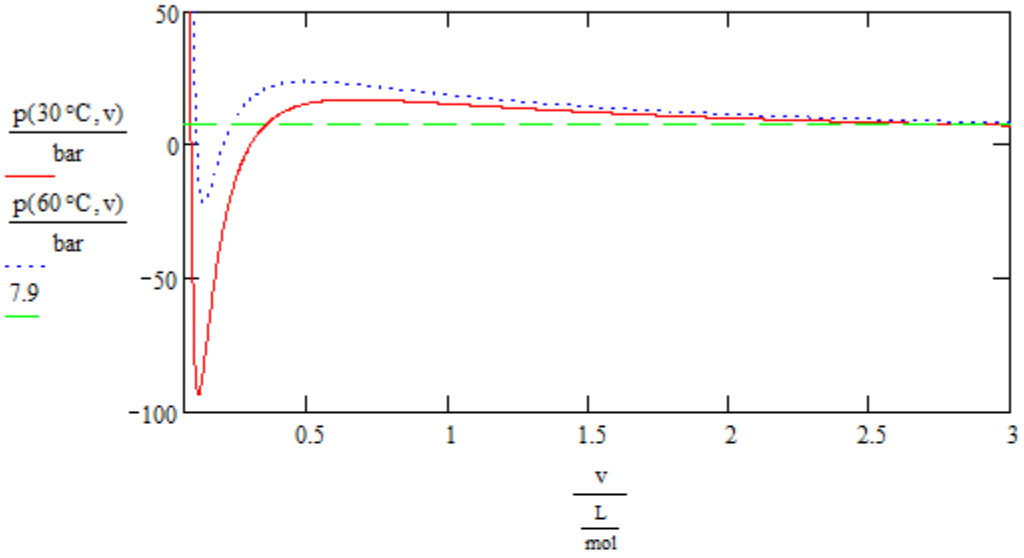

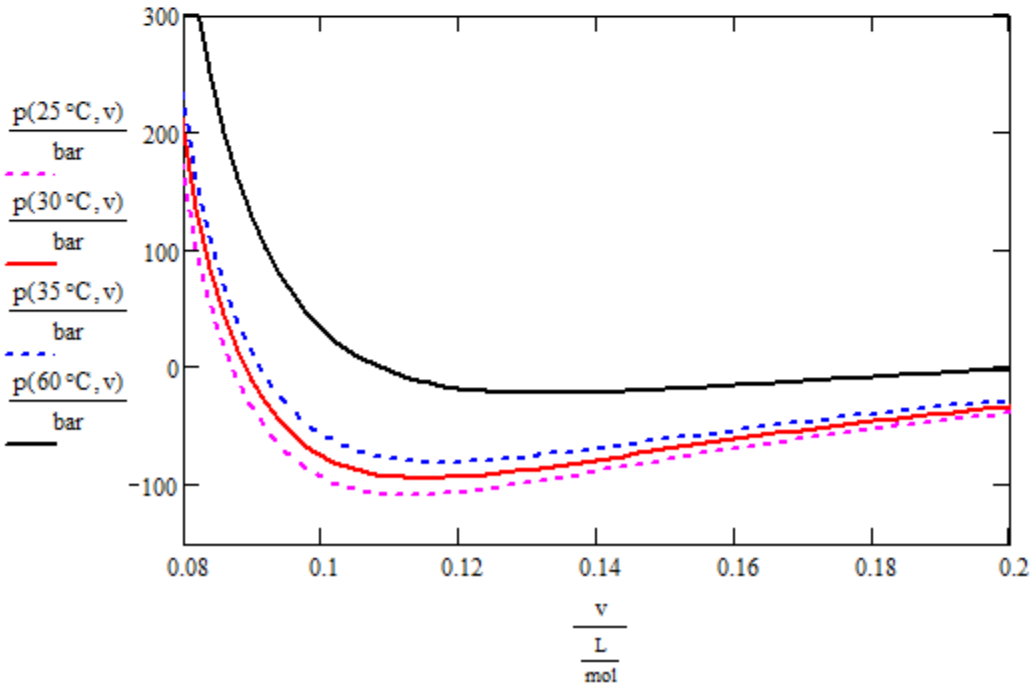

Now start with an initial subcooled state that is at To = 30C, po = 15 bar = 15 MPa

Plot the PR relation as a function of v giving:

$$v := 0.06 \cdot \frac{L}{mol}, 0.061 \cdot \frac{L}{mol} .. 4 \cdot \frac{L}{mol}$$

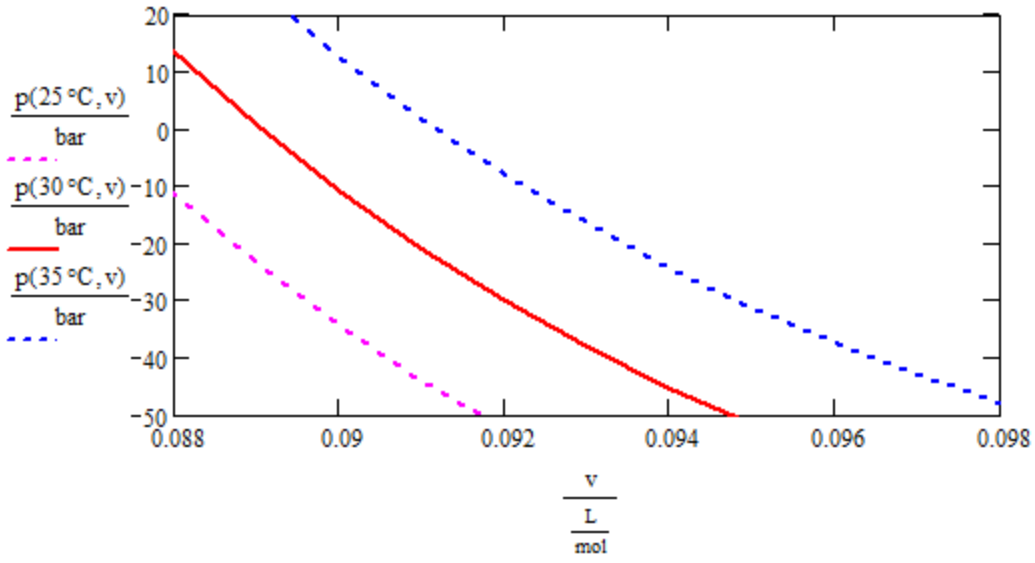

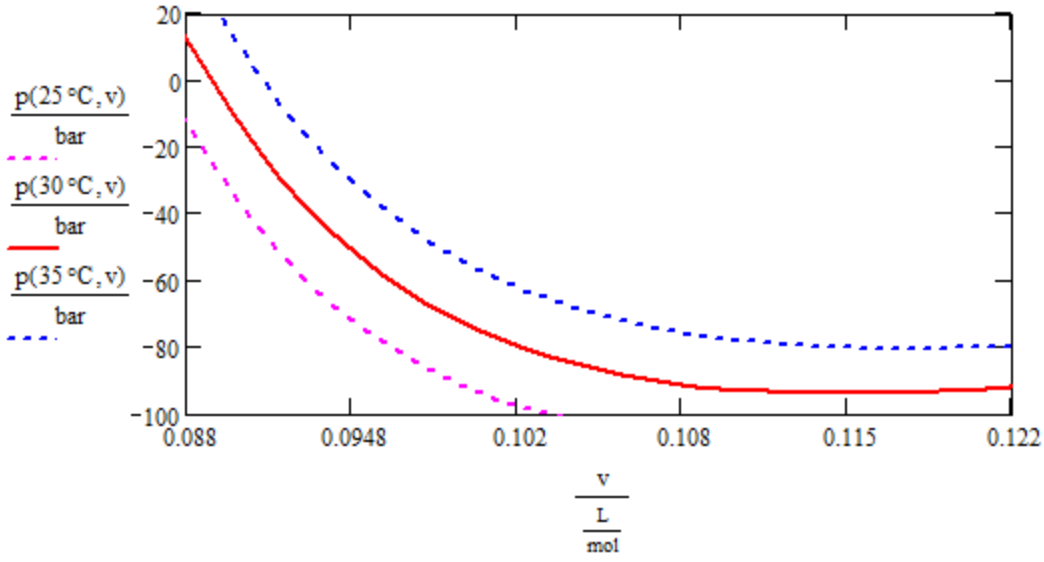

Finding Spinodal Points

Peng Robinson Equation Derivation (R134a)

$T := 261.15 \qquad V := 0.002$

$$P2(V,T) := \left[\frac{-(R \cdot T)}{(V - b)^2} + \frac{2a \cdot (V + b) \cdot \alpha(T)}{\left(V^2 + 2 \cdot b \cdot V - b^2\right)^2} \right] \cdot 10^{-8}$$

$P2(V,T) = -2.511$

$$dPdV(V,T) := 10^{-8} \cdot \frac{d}{dV} P(V,T)$$

$dPdV(V,T) = -2.511$

$V := 0.000060, 0.000061 .. 0.003$

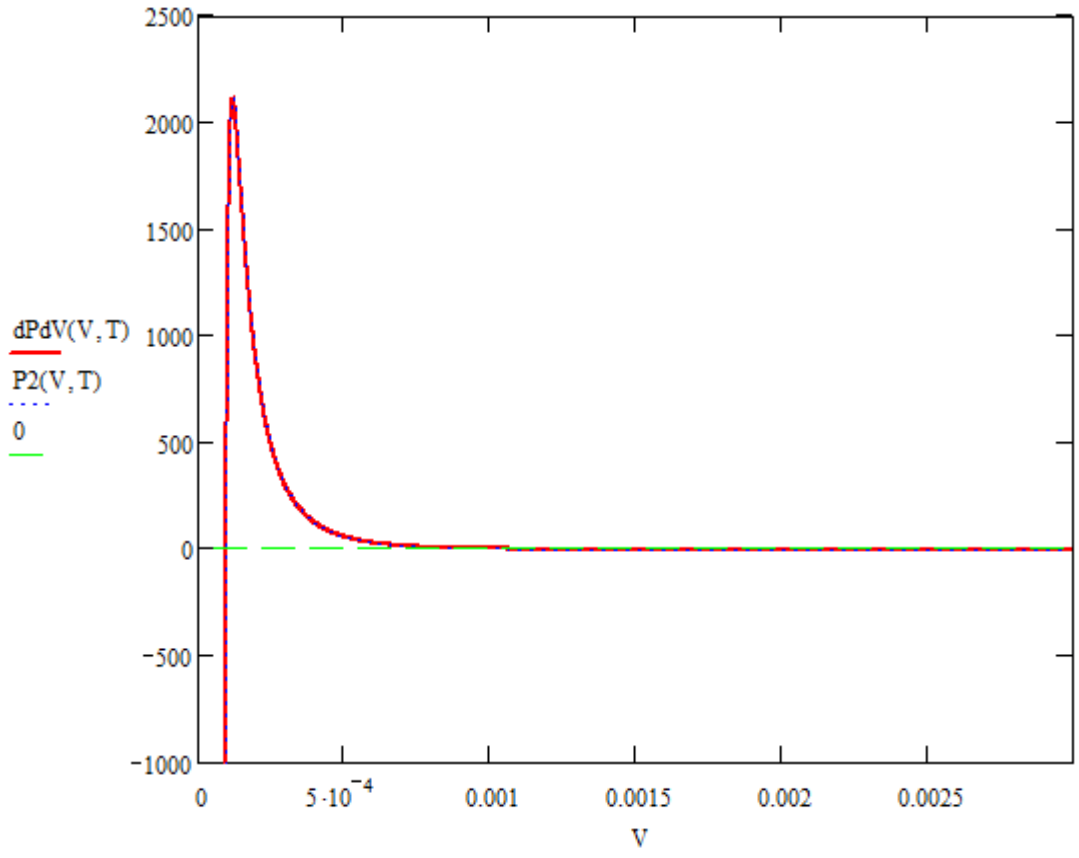

$V2 := 0.5 \times 10^{-4}$ $y2 := 0.0005$ $y2 := 0.0015$

Given

$dPdV(V2, T) = 0$

$dPdV(y2, T) = 0$

$V3 := 1 \cdot 10^{-4}$ $y3 := 20$

Given

$P2(V3, T) = 0$

Spinodal Points

$X3 := Find(V3, y3)$

$$X3 = \begin{pmatrix} 9.965 \times 10^{-5} \\ 20 \end{pmatrix}$$

Appendix D - Temperature Equation Analysis

Basic theories were proposed first by Dr. Sorensen and then used for evaluations

Static Evaluations

Assuming all the heat comes out of the flowing liquid, and not the surrounding environment, that yields the maximum temperature drop, ΔT_{max}. The heat required to form a mass of gas is

$$dq = h_{fg} dm_g$$

where h_{fg} is the latent heat of vaporization of the fluid. If we assume heat comes from gas and liquid phases we get,

$$dq = (m_g C_g + m_l C_l) dT$$

where C_g and C_l are the mass heat capacities of the gas and liquid states, then introducing the total mass which,

$$m = m_g + m_l$$

then solving for dT gives an equation

$$dT = dm_g h_{fg} / [(C_l - C_g) m_l + m C_g]$$

differentiating the equation gives

$$\Delta T = \frac{h_{fg}}{\Delta C} \ln\left[(m_l \Delta C + C_g m) / m C_l\right]$$

using $\Delta C = C_l - C_g$ and $x = m_g/m$ we get,

$$\Delta T = \left(\frac{h_{fg}}{\Delta T}\right) \ln\left[1 - \left(\frac{\Delta C}{C_l}\right) Q\right]$$

for a small quality the equation reduces to

$$\Delta T_{max} = -\left({}^{h_{fg}}\!/_{C_l}\right) x$$

Heat Flow Rate Evaluations

Assuming the heat sources comes from the fluid itself and environment. Thus, we introduce a heat flow rate equation as

$$\dot{q} = \dot{q_{fl}} + \dot{q_{en}}$$

where $\dot{q_{fl}}$ is the heat from fluid and $\dot{q_{en}}$ is heat from environment. We then introduce a fraction shows less than 1 of the heat comes from the environment and temperature decrease becomes $\Delta T = (1 - f)\Delta T_{max,}$ solving for the fraction we get,

$$f = 1 - \left({\Delta T}/{\Delta T_{max}}\right)$$

then the heat flow rate from the environment is

$$\dot{q_{en}} = f h_{fg} \rho x \varphi_v = \left(1 - \left({\Delta T}/{\Delta T_{max}}\right)\right) L_v \rho Q \varphi_v$$

using equation ΔT_{max} we get

$$\dot{q_{en}} = \rho \varphi_v \left(h_{fg} x - C_l \Delta T\right)$$

Dynamics Evaluations

We consider the kinetic energy a mass of the flowing liquid with a velocity entering the nucleation zone. We assume the gas phase accelerates and nucleate which the kinetic energy equation for gas is defined as

$$\Delta \boldsymbol{E} = \frac{\mathbf{1}}{\mathbf{2}} \boldsymbol{m_g V_g^2}$$

then using the conservation of mass we introduce

$$\dot{\boldsymbol{m}}_{\boldsymbol{g}} - \dot{\boldsymbol{m}}_{\boldsymbol{l}} = (\boldsymbol{\rho AV})_{\boldsymbol{g}} - (\boldsymbol{\rho AV})_{\boldsymbol{l}} = 0$$

With a constant area we get an equation for the velocity of the gas

$$\boldsymbol{V_g} = \boldsymbol{V_l} \left(\frac{\boldsymbol{\rho_l}}{\boldsymbol{\rho_g}} \right)$$

Introducing the mass quality as

$$\boldsymbol{x} = \frac{\boldsymbol{m_g}}{\boldsymbol{m_l}}$$

$$\boldsymbol{m_g} = x\, \boldsymbol{m_l}$$

Then we introduce the energy equation in terms of the liquid's thermal energy

$$\Delta \boldsymbol{E} = \boldsymbol{m_l C_l \Delta T}$$

Under the assumption that all the kinetic energy comes out of the thermal liquid's energy, solving for the temperature drop with the gas phase nucleating, we get an equation of

$$\Delta \boldsymbol{T} = \frac{\boldsymbol{x\, V_l^2} \left(\frac{\boldsymbol{\rho_l}}{\boldsymbol{\rho_g}} \right)^{\mathbf{2}}}{\mathbf{2} \boldsymbol{C_l}}$$